UC San Diego
UC San Diego Electronic Theses and Dissertations

Title
From Visualization of Molecular Events to Remote Control of T Cells

Permalink

Author
Wu, Yiqian

Publication Date
2020

Supplemental Material

Peer reviewed|Thesis/dissertation

UNIVERSITY OF CALIFORNIA SAN DIEGO

From Visualization of Molecular Events to Remote Control of T Cells

A dissertation submitted in partial satisfaction of the requirements for the degree

Doctor of Philosophy

in

Bioengineering

by

Yiqian Wu

Committee in charge:

      Professor Yingxiao Wang, Chair
      Professor Shu Chien, Co-Chair
      Professor Stephanie Fraley
      Professor Thomas Liu
      Professor Prashant Mali

2020

The Dissertation of Yiqian Wu is approved, and it is acceptable in quality and form for

publication on microfilm and electronically:

_____

_____

_____

_____
Co-Chair

_____
Chair

University of California San Diego

2020

EPIGRAPH

We like to be out in nature so much because it has no opinion about us.

Friedrich Nietzsche

TABLE OF CONTENTS

LIST OF ABBREVIATIONS

ALL   Acute lymphocytic leukemia

BLI   Bioluminescence imaging

CAR   Chimeric antigen receptor

CCR   Chimeric costimulatory receptor

CFMRI   Center for Functional MRI

CLL   Chronic lymphocytic leukemia

CRISPR   Clustered Regularly Interspaced Short Palindromic Repeats

CRS   Cytokine release syndrome

dCas9   Endonuclease dead Cas9

DLBCL   Diffuse large B cell lymphoma

DMEM   Dulbecco's Modified Eagle Medium

DNMT   DNA methyltransferase

Dox   Doxycycline

E:T   Effector-to-target

ECFP   Enhanced cyan fluorescent protein

EGFP   Enhanced green fluorescent protein

ER   Estrogen receptor

EYFP   Enhanced yellow fluorescent protein

FA   Focal adhesions

FACS   Fluorescence-activated cell sorting

FAK   Focal adhesion kinase

FAT   FA-targeting

FBS	Fetal bovine serum
FKBP	FK506 binding protein
Fluc	Firefly luciferase
FP	Fluorescent protein
FRB*	FKBP-rapamycin binding domain
FRET	Förster resonance energy transfer or fluorescence resonance energy transfer
FUS	Focused ultrasound
GFP	Green fluorescent protein
gRNA	guide RNA
HIFU	High-intensity focused ultrasound
HS	Heat shock
HSP	Heat shock protein
Hsp	Heat shock protein promoter
iCAR	Inhibitory chimeric antigen receptor
IFN-γ	Interferon gamma
IL-2	Interleukin-2
IVIS	In vivo Imaging System
JAX	Jackson Laboratory
MACS	Magnetic-activated cell sorting
MEF	Mouse embryonic fibroblast
MRI	Magnetic resonance imaging
PBMC	Peripheral blood mononuclear cell

PBS   Phosphate-buffered saline

PCR   Polymerase chain reaction

PSMA   Prostate-specific membrane antigen

qPCR   Quantitative PCR

Rapalog   Rapamycin analog

Rluc   Renilla luciferase

ROI   Region of interest

RPMI   Roswell Park Memorial Institute medium

SFK   Src family kinase

Tet   Tetracycline

tetO   Tetracycline operator

tetR   Tetracycline repressor

TSS   Transcription starting site

tTA   Tetracycline-controlled transactivator

YPet   Yellow fluorescent protein

LIST OF FIGURES

LIST OF TABLES

LIST OF SUPPLEMENTAL VIDEOS

ACKNOWLEDGEMENTS

I would like to thank my advisor and committee chair Dr. Yingxiao (Peter) Wang. Thank you for your advice and support throughout the years that made this dissertation possible. Thank you for the creative ideas, inspiring discussions, multiple rounds of draft revision, and all your efforts in establishing collaborations for my projects. Thank you for being so optimistic, positive, available, and supportive. Your passion and enthusiasm for science inspire us all.

I would like to thank the rest of my committee members, Dr. Shu Chien, Dr. Stephanie Fraley, Dr. Thomas Liu, and Dr. Prashant Mali for your most valuable help throughout my thesis and defense. In particular, Dr. Chien, thank you for being the co-chair of my committee, and for all your constructive, critical, insightful and helpful feedback on draft revisions and individual meetings. Dr. Liu, thank you for welcoming me into the Center for Functional MRI (CFMRI), introducing me to your most helpful staff Bob and Aaron, and providing indispensable support for the establishment of the MRI-guided focused ultrasound (FUS) system at CFMRI.

I would like to thank my mentor Dr. Shaoying (Kathy) Lu. When I was an undergraduate exchange student at UIUC in 2012, I emailed faculty members about working as a volunteer in their labs. Kathy was the only one that replied. Later when the Wang lab moved to UCSD, Kathy recruited me as a PhD student. I worked closely with Kathy on computational analysis during my first year of PhD. Kathy, thank you for your kindness and mentorship that led me here.

I would like to thank Dr. Ziliang (Adam) Huang. Adam taught me every lab techniques when I started experimental lab in my second year of PhD. He is also a great friend in life, interesting, smart, humorous, and tolerant. Thank you for everything.

I would like to thank Dr. Yahan Liu, who has been working closely with me since she joined the lab at the end of 2018 as a visiting scholar. Yahan is an experienced and hardworking

researcher, and also a very likable person. Yahan, thank you for all your contributions to my project, and more importantly, for being the sister I never had.

I would like to thank Dr. Zhen (Jane) Jin, who worked closely with me from 2016 to 2017 during her visit in our lab. Months before she arrived, we had just started working on primary human T cells for the first time in our lab and were struggling with infection efficiencies. Zhen had worked with T cells before, and made me realize the importance of MOI, which led to our titration experiments and the identification of the optimal MOI for infection. Soon after, we were able to achieve high infection efficiencies. Zhen also taught me animal techniques that laid the foundation for my later *in vivo* work. We also became close friends outside the lab. Zhen, thank you for your help, company, and friendship that helped me through one of the most difficult times during my PhD.

I would like to thank Dr. Praopim (Mint) Limsakul. Not long after I joined the Wang lab, I discovered that we lived in the same building on campus. I paid her a visit at her apartment, leading to her helping me catch a cockroach in my apartment and us walking 30 min one way for grocery shopping (all happened on the same day), marking the start of our friendship. We became close friends and shared endless conversations and food in the following years. Mint graduated recently and is now a professor in Thailand. Thank you, Mint, for all the support in both research and life, and for always being on my side.

I would like to thank Dr. Robert Bussell and Mr. Aaron D. Jacobson at the UCSD CFMRI. When Erik delivered the FUS system at the CFMRI at the end of 2017, Bob and Aaron helped figure out the technical details with Erik and integrate the FUS with the 7T MRI. This first MRI-guided FUS system on UCSD campus could not have been established without them.

They continued to help me with the troubleshooting of this system. Bob and Aaron, I greatly appreciate your expertise and help.

I would like to thank Dr. Erik Dumont and Ms. Stéphanie Hoarau-Recco at Image Guided Therapy in France for their tremendous help on the FUS system. Erik (and his team) built the FUS system and integrated it with the 7T MRI at UCSD CFMRI, which is the key tool for my research. I haven't met Stéphanie in person, but we have exchanged dozens of emails regarding the troubleshooting of the FUS system. Stéphanie wrote new scripts that enabled more precise regulation of the temperature. Thank you for making my research possible.

I would like to thank Shannon Laub, Ali Zamat, Xin Wang, Yuzhou Tong and Jiayi Li, for being the sweetest mentees I could ever ask for. In particular, Xin worked with me closely on the troubleshooting of the MRI-guided FUS system in 2018, during which we shared numerous frustrations and excitement.

I would like to thank the rest of the Wang lab members, past and present, for their help and support. To Ya Gong and Yiwen Shi for your sweet friendship and company; to Linshan Zhu and Chi-Wei Man for the funny office talks; to Drs. Qin Peng, Longwei Liu, Chi Woo (Nate) Yoon, Reed Harrison, Yijia Pan, Molly Allen, Rongxue Wan, Pengzhi Wang, Lei Lei, Mingxing Ouyang, Binbin Cheng, for the memorable moments; and to Rinoka Sato and Yujia Fu, for the management help.

I would like to thank all my other collaborators and co-authors, especially Dr. Michael Bouvet and his team, Dr. Helmi Lwim, and Dr. Ya-Ju (Bird) Chang, for providing valuable inputs and essential collaborative efforts.

I would like to thank the staff at UCSD for their help during my PhD. In particular, to Vu Nguyen, Cody Fine, and Jesus Olvera at HESCCF for your help with cell sorting. To Jan Lenington, for your help with all my paperwork.

I would like to thank my dear friends, near and far, for being there for me, supporting me and encouraging me.

Most importantly, I want to thank my parents. Thank you for supporting your only child in pursuing her dreams, even though it meant she would be thousands of miles away from home for years. Thank you for always respecting my decisions and choices. Thank you for your unconditional love.

VITA

2014   Bachelor of Engineering in Biomedical Engineering, The Chinese University of Hong Kong

2020   Doctor of Philosophy in Bioengineering, University of California San Diego

PUBLICATIONS

1. Huang Z*, **Wu Y***, Allen M, Pan Y, Kyriakakis P, Lu S, Chang YJ, Wang X, Chien S, Wang Y. Engineering Light-controllable CAR T Cells for Cancer Immunotherapy. *Science Advances*. Accepted. 2020. * indicates equal contribution.

2. Allen ME, Zhou W, Thangaraj J, Kyriakakis P, **Wu Y**, Huang Z, Ho P, Pan Y, Limsakul P, Xu X, Wang Y. An AND-gated Drug and Photoactivatable Cre-*loxP* System for Spatiotemporal Control in Cell-based Therapeutics. *ACS Synthetic Biology.* 2359-2371. 2019.

3. Wan R, Wu J, Ouyang M, Lei L, Wei J, Peng Q, Harrison R, **Wu Y**, Cheng B, Li K, Zhu C, Tang L, Lu S, Wang Y. Biophysical Basis underlying Dynamic Lck Activation Visualized by ZapLck FRET Biosensor. *Science Advances*. 5(6): eaau2001. 2019.

4. **Wu Y** and Wang Y. Synthetic Biology: Protein Circuits Reprogram Cells. *Nature Chemical Biology*. 15(2):96-97. 2019.

5. Bank RE, **Wu Y**, Shi Y, Gill PE, Wang Y, Lu S. Optimization with Partial Differential Equation Constraints for Bio-imaging Applications. *Computing and Visualization in Science*. Accepted. 2018.

6. Pan Y, Yoon S, Sun J, Huang Z, Lee C, Allen M, **Wu Y**, Chang Y-J, Sadelain M, Shung K.K, Chien S, and Wang Y. Remote Controlled Mechanogenetics for Gene Manipulation and CAR T Immunoengineering in Live Cells. _Proc Natl Acad Sci USA_. 115(5):992-997. 2018.

7. Limsakul P, Peng Q, **Wu Y**, Allen M, Liang L, Remacle AG, Lopez T, Ge X, Kay B, Zhao H, Strongin AY, Yang Y-L, Lu S, and Wang Y. Directed Evolution to Engineer Monobody for FRET Biosensor Assembly and Imaging at Live-Cell Surface. _Cell Chemical Biology_. 25(4):370-379.e4. 2018.

8. **Wu Y**, Zhang K, Seong J, Fan J, Chien S, Wang Y, Lu S. In-situ Coupling between Kinase Activities and Protein Dynamics within Single Focal Adhesions. _Scientific Reports_. 6: 29377. 2016.

9. Ma Z*, **Wu Y***, Mak AFT. Rheological Behavior of Actin Stress Fibers in Myoblasts after Nanodissection: Effects of Oxidative Stress. _Biorheolog_y. 52(3) 225-234, 2015. * indicates equal contribution.

10. Zhuo Y, Qian T, **Wu Y**, Seong J, Gong Y, Ma H, Wang Y, Lu S. Subcellular and Dynamic Coordination between Src Activity and Cell Protrusion under Microenvironment modulations. _Scientific Reports_. 11(5): 12963. 2015.

11. Xiao Z, **Wu Y**, Mak AFT. Accumulation of Loading and Unloading Reperfusion Injury – Modeling for the Propagation of Deep Tissue Ulcers. _Journal of Biomechanics_. 47(2014): 1658-1664. 2014.

12. Liao X, Lu S, **Wu Y,** Xu W, Zhuo Y, Peng Q, Li B, Zhang L, Wang Y. The Effect of Differentiation Induction on FAK and Src Activity in Live HMSCs Visualized by FRET. _PLoS ONE_. 8(8): e72233. 2013.

ABSTRACT OF THE DISSERTATION

From Visualization of Molecular Events to Remote Control of T Cells

by

Yiqian Wu

Doctor of Philosophy in Bioengineering

University of California San Diego, 2020

Professor Yingxiao Wang, Chair

Professor Shu Chien, Co-Chair

Cancer remains a major threat to human health. Utilizing imaging tools including fluorescent proteins and Förster resonance energy transfer-based biosensors, we visualized the molecular events involved in cancer metastasis such as kinases activities at single focal adhesions (FAs) in living cells. Combined with single FA tracking and cross-correlation analysis,

we quantified the temporal coordination between the observed kinases activities and FA structural change at single FA resolution, providing new insights into the dynamic coupling between these molecular events that are crucial for cancer cell adhesion. In addition to observational tools, we asked if we could use perturbative tools to reprogram cells to achieve desired therapeutic functions against cancer. Recently, T cells genetically engineered with chimeric antigen receptors (CARs) have shown unprecedented efficacy in treating blood cancers. The CAR T cells possess redirected specificity against tumor cells expressing the target antigens, and are thus effective in recognizing and eliminating target tumor cells. However, the extensive overlap of the antigens between tumor (especially solid tumor) and normal tissues makes it difficult to identify a truly tumor-specific antigen. As a result, the CAR T cells might attack normal tissues expressing low levels of the target antigen and cause severe side effects. To alleviate this "on-target, off-tumor" toxicity, we sought to utilize ultrasound to remotely control the activation of the infused CAR T cells at a confined region and desired time. Focused ultrasound (FUS) can induce temperature increase in biological samples due to internal friction, and has been applied to regulate heat-inducible transgene expression *in vivo*. While other regulation systems utilizing small molecules or light exist, FUS-based induction method has better spatiotemporal resolution and deeper penetration. We engineered heat-inducible CAR T cells responsive to FUS heating and demonstrated their efficacy in inhibiting tumor growth *in vivo* after FUS stimulation. We envision that the FUS controllable CAR T therapy will emerge as a powerful treatment for solid tumors, and FUS-based acoustogenetics will become a platform for the remote manipulation of genetics, epigenetics, and cellular functions in living organisms.

CHAPTER 1. INTRODUCTION

1.1. Visualization of molecular events in live cells

The invention of microscopes opened the door to a previously invisible world of cells, molecules, and smaller structures, and opened up new fields in life science. Over time, imaging methods have been developed to probe into the inner life of cells. One example of such imaging tools is a class of genetically encoded biosensors based on Förster resonance energy transfer (FERT).

Förster resonance energy transfer, fluorescence resonance energy transfer, or FRET, describes the process where the energy from an excited chromophore (donor) is nonradiatively transferred to a nearby chromophore (acceptor). The first experimental observation of FRET and theories attempting to explain this phenomenon date back to the early 1900s. In the mid-1900s, Theodor Förster developed the correct quantitative theory of FRET accompanied by experimental verifications, which laid the foundation for subsequent applications of FRET in physics, chemistry, and biology (*1*).

But it was not until the discovery of fluorescent proteins (FPs) was FRET widely applied to biological and biomedical studies. Green fluorescent protein (GFP) was first purified by Osamu Shimomura from the jellyfish *Aequorea victoria* in the early 1960s, and its DNA sequence was first cloned by Douglas Prasher in 1992 (*2*). In the mid-1990s, with the GFP gene from Douglas Prasher, Martin Chalfie expressed GFP in *E. coli* and *C. elegans*, and Roger Tsien mutated and improved the wild-type GFP to obtain enhanced GFP (EGFP) and its color variants for biological and medical applications, among which Tsien also proposed the usage of FPs for FRET (*3*).

For FRET to occur, the two chromophores (or FPs, in the case of FP-FRET) must be in close proximity (~1 - 10 nm) and favorable mutual orientation (*4*). More importantly, the emission spectrum of the donor FP must overlap significantly (>30%, (*5*)) with the excitation spectrum of the acceptor FP. The development of an array of GFP color variants made it possible to obtain FP pairs suitable for FRET. This led to the invention of a class of genetically-encoded FRET biosensors for the study of cellular signaling in live cells. Besides the two FPs (the FRET pair), these FRET biosensors also contain domains (e.g., proteins, cleavage or substrate peptides, binding sites, etc.) capable of inducing conformational change of the biosensor with the presence of certain signaling cues. The conformational change further leads to a change in the distance/orientation between the two FPs and the resultant FRET (*6*). This class of FRET biosensors have been applied to study signaling molecules inside cells such as kinases (*7*).

Traditionally, kinase activities inside cells are studied using methods such as western blot and immunostaining (*8*). Western blot requires lysing of cells followed by protein denaturation, gel electrophoresis, and antibody staining, producing an averaged readout from a large quantity of cells. Immunostaining has improved spatial resolution as it enables the visualization of single cells, but still requires cell fixation and fails to capture the dynamic changes in live cells.

FRET biosensors, on the other hand, allow the dynamic visualization of kinase activities in live cells with high spatiotemporal resolutions, and have thus stood out from traditional methods and gained increased popularity in the field. One example of this class of FRET biosensors, on which Chapter 2 is based, is a Src FRET biosensor developed by Wang et al. in 2005 (*9*). Src is a non-receptor tyrosine kinase that plays important roles in cellular signaling in cell proliferation and cancer invasion. The biosensor is composed of the classic FRET FP pair, i.e., enhanced cyan FP (ECFP) and enhanced yellow FP (EYFP), with the SH2 domain, a flexible

linker, and a Src substrate peptide in between. When Src is activated, it phosphorylates the

substrate peptide, causing the binding of the SH2 domain to the phosphorylated tyrosines in the

substrate peptide. As a result of this conformational change, the originally adjacent ECFP and

EYFP are separated, and a decrease in FRET is observed. Using this FRET biosensor, Wang et

al. witnessed the propagation of a Src activation wave across a live cell upon mechanical

stimulation (*9*).

1.2. Remote control of cells via genetic reprogramming

1.2.1. Inducible gene expression systems

Through the visualization of molecular events and the understanding of their coordination

in determining cellular functions, we ask ourselves if we can reprogram cells to control their

functions for desired outcomes.

To date, plenty of methods have been developed to control cellular functions, including

the genetic engineering of cells to express functional transgenes. However, many of these

transgene expressions are constitutive and unregulated, resulting in unnecessarily high

expression levels that are potentially harmful (*10*). It is therefore desirable to have enhanced

controllability over transgene expressions in terms of magnitude, location, and time.

To this end, researchers have engineered inducible gene regulation systems utilizing

external cues such as chemicals, light, or mechanical stimuli to control transgene expression.

Tetracycline inducible systems represent a class of drug-inducible gene expression systems. In

1992, Gossen and Bujard developed a Tetracycline-Off (Tet-Off) system in which the transgene

could be virtually silenced with the presence of tetracycline (*11*). To do so, they fused the

tetracycline repressor (*tet*R) from *E. coli* and the transcriptional activator VP16 to generate a

hybrid tetracycline-controlled transactivator tTA. They also constructed an inducible promoter composed of tetracycline operator (*tet*O) sequences and a minimal promoter to drive the reporter luciferase gene. Without tetracycline, tTA binds to *tet*O in the inducible promoter and allows transgene transcription. When tetracycline is present, it binds to the *tet*R in the tTA, thus preventing the binding of tTA to the inducible promoter. As a result, the transgene expression is inhibited. In 1995, Gossen et al. developed another system (later named Tet-On) where the presence of tetracycline (or its derivative doxycycline, dox) led to gene activation instead of repression (*12*). Other examples of drug-inducible gene regulation systems include rapamycin-regulated systems based on rapamycin-inducible protein dimerization, and tamoxifen-regulated systems based on tamoxifen-induced nuclear translocation of the estrogen receptor (ER) and its fused recombinase such as Cre (*13*).

Although chemicals provide enhanced controllability compared to traditional systems, they often act slow and lack tissue specificity, and therefore have limited spatiotemporal resolutions in regulating transgene expressions. Light, on the other hand, can trigger responses in milliseconds at specified regions in cells and living organisms. In 2005, Boyden et al. utilized light to control the activation of mammalian neurons expressing an exogenous light-sensitive ion channel named Channelrhodopsin-2, a technology termed optogenetics (*14*). Since then, optogenetics has become a booming field even beyond neuroscience (*15*). In 2010, Kennedy et al. utilized another pair of light-sensitive proteins CRY2 and CIB1 that undergo heterodimerization upon light stimulation to bring two inactivate fragments of a split protein (e.g., Cre recombinase) together, rendering it functional again (*16*). Other systems based on light-inducible protein dimerization or conformational change for the controllable regulation of transgene expression were also developed (*17*).

Despite the advantages of light over chemicals such as precise spatial control and fast dynamics, the penetration depth of light is limited at millimeters, making it suboptimal for *in vivo* or therapeutic applications unless using invasive optical fibers for illumination. It is therefore desirable to utilize a tool that is clinically compatible and has long penetration depth to achieve remote and noninvasive control of gene expression. One candidate that matches these criteria is ultrasound.

Focused ultrasound (FUS) has a typical penetration depth of centimeters in living organisms. It can exert oscillating pressure on and result in cyclic loading and unloading of biological tissues. This process generates thermal energy through internal friction and leads to temperature elevation in the local tissue (*18*). The ability of FUS to induce hyperthermia and its integration with magnetic resonance imaging (MRI) thermometry has made it a useful research and clinical tool. MRI-guided high-intensity FUS (HIFU) causing local temperature increase to above 65°C is used clinically to ablate malignant and nonmalignant tissues (*19*). Mild hyperthermia induced by MRI-guided FUS can facilitate drug delivery, vasodilation, and neuromodulation (*20*).

Moreover, MRI-guided FUS has been used by researchers to drive the expression of heat-sensitive transgenes. Heat shock proteins (HSPs) are a class of proteins that are synthesized in response to heat stimulation in living organisms. Utilizing the promoter of the HSP (heat shock promoter, Hsp), Guilhon et al. demonstrated MRI-guided FUS-induced expression of a heat-sensitive GFP transgene (Hsp-GFP) (*21*). Other studies utilizing this technology to activate Hsp-driven reporter transgenes have also been published (*22*). As such, FUS-based acoustogenetics represents one of the optimal technologies for controlling inducible gene expression with precise spatiotemporal resolutions.

1.2.2. CAR T therapy

The reprogramming of cells via genetic engineering not only provides mechanistic understanding of biological processes, but also offers opportunities to improve the welfare of human beings.

One example is the reprogramming of T cells to gain redirected specificity to fight cancer, the so-called "CAR T therapy", which is also the basis of Chapter 4. "CAR" stands for chimeric antigen receptor. In CAR T therapy, T cells from the patients are genetically modified in the laboratory to express CAR molecules on cell surface. A CAR molecule is composed of (1) an extracellular single-chain variable fragment (scFv) that can recognize a specific target antigen on the tumor cell surface, (2) transmembrane domain and (3) intracellular co-stimulatory and activation domains that facilitate signal transduction and T cell activation upon engagement with target tumor cells. The engineered CAR T cells are infused back to the patients to treat cancers.

While initial research on CAR T cells dates back to 1989 (*23, 24*), successful clinical reports on CAR T therapy did not come out until around 20 years later, when one case report in 2010 described a partial response in a B cell lymphoma patient treated with anti-CD19-CAR-transduced T cells (*25, 26*). In 2011, it was reported for the first time that complete remission was achieved in a chronic lymphocytic leukemia (CLL) patient treated with anti-CD19-CAR T cells (*27*). Since then, CAR T therapy has received unprecedented attention, especially with the approvals of CAR T therapies for acute lymphocytic leukemia (ALL) and diffuse large B cell lymphoma (DLBCL) by FDA in 2017 (*25*).

1.2.3. On-target off-tumor toxicity and its countermeasures

Despite its success in treating blood cancers, side effects and limitations of CAR T therapy need to be addressed before it can be applied to treat solid tumors. As normal tissues may share the same target antigens with tumors, they can be attacked by the infused CAR T cells as well. This "on-target, off-tumor" toxicity has caused manageable to lethal side effects in patients (*28*). In the most severe case, an infusion of a high dose of 10^{10} anti-ERBB2 CAR T cells in an attempt to treat a patient with ERBB2 overexpressing tumors resulted in respiratory and multiorgan failure and subsequent death (*29*). It was believed that the large amount of the infused anti-ERBB2 CAR T cells recognized the low-level ERBB2 antigens on normal lung cells and secreted inflammatory cytokines leading to a cascading cytokine storm, resulting in unforeseen consequences (*29*). Several strategies have been developed to tackle this "on-target, off-tumor" toxicity, including inhibitory CARs, combinatorial CARs, synNotch CARs, and small molecular-gated CARs (*30-33*).

Inhibitory CARs (iCARs) are designed based on the assumption that although normal tissues and tumor cells have shared expression of antigen 1, normal tissues also express an antigen 2 that is not expressed on tumors. An iCAR T cell expresses a canonical CAR against antigen 1, and an iCAR composed of a scFv recognizing antigen 2 and the signaling domains of immunoinhibitory receptors (e.g. PD-1). Fedorov et al. demonstrated that the iCAR was able to inhibit the activating CAR, rendering the T cells cytotoxic to cells expressing only antigen 1 but not those expressing both antigens 1 and 2 (*30*). However, the strength of the positive activating CAR and the negative iCAR need to be characterized and tuned to ensure iCAR T cells can function properly.

Combinatorial CAR T cells are designed to attack only when both target antigens are present. A combinatorial CAR T cell expresses a first generation CAR composed of a scFv recognizing target antigen 1 and an activation domain (CD3ζ), and a chimeric costimulatory receptor (CCR) composed of another scFv recognizing target antigen 2 and costimulatory domains (CD28, 4-1BB). Kloss et al. showed that the engineered T cells demonstrated optimal efficacy against tumor cells expressing both target antigens 1 and 2 both not those expressing only one antigen (*31*). It is of note that in this logic AND gate strategy, careful characterization is needed to ensure that the CAR reaches only suboptimal activation upon antigen 1 binding for its function to be rescuable by the CCR after engaging with antigen 2.

SynNotch CAR T cells represent another type of AND gate-based design. A synNotch CAR T cell expresses an antigen 1-recognizing synNotch receptor fused with a transcriptional activator. The engagement of the T cell with target cells expressing antigen 1 triggers the cleavage of the synNotch receptor and leads to the release of the transcriptional activator. The transcriptional activator then induces the expression of a CAR against antigen 2. Roybal et al. showed that the synNotch CAR T cells were able to selectively attack tumor cells with both antigens while sparing those with only one antigen (*32*).

Small molecule-gated CAR T cells utilize a drug-inducible heterodimerization system briefly discussed in Section 1.2.1. In this design, the extracellular antigen-recognizing scFv and the intracellular activation domain of a conventional CAR are split in two proteins, with one fused to FK506 binding protein (FKBP) domain and another to T2089L mutant of FKBP-rapamycin binding domain (FRB*). Wu et al. showed that the presence of a rapamycin analog (rapalog) induced the heterodimerization between FKBP and FRB*, bringing the split halves together to form a functional CAR (*33*). The inducible CAR T cells treated with rapalog became

active after engaging with the target tumor antigen. However, as discussed before, the spatial resolution of small molecule-mediated control may be limited.

We approached this problem from a different angle by employing external stimuli to switch CAR T cells from a resting state to an active state *in vivo* with desired spatial and temporal precision. To this end, we were motivated to utilize ultrasound to remotely and noninvasively activate infused CAR T cells through acoustogenetics, which we will discuss in detail in Chapter 4.

1.3. References

1. Clegg, R. M. (2006). The History of Fret. In C. D. Geddes & J. R. Lakowicz (Eds.), *Reviews in Fluorescence 2006* (pp. 1-45). Boston, MA: Springer US.

2. Tsuji, F. I. (2010). Early history, discovery, and expression of Aequorea green fluorescent protein, with a note on an unfinished experiment. *Microsc Res Tech, 73*(8), 785-796. doi:10.1002/jemt.20821

3. Zimmer, M. (2009). GFP: from jellyfish to the Nobel prize and beyond. *Chem Soc Rev, 38*(10), 2823-2832. doi:10.1039/b904023d

4. Periasamy, A. (2001). Fluorescence resonance energy transfer microscopy: a mini review. *J Biomed Opt, 6*(3), 287-291. doi:10.1117/1.1383063

5. Sekar, R. B., & Periasamy, A. (2003). Fluorescence resonance energy transfer (FRET) microscopy imaging of live cell protein localizations. *J Cell Biol, 160*(5), 629-633. doi:10.1083/jcb.200210140

6. Zadran, S., Standley, S., Wong, K., Otiniano, E., Amighi, A., & Baudry, M. (2012). Fluorescence resonance energy transfer (FRET)-based biosensors: visualizing cellular dynamics and bioenergetics. *Appl Microbiol Biotechnol, 96*(4), 895-902. doi:10.1007/s00253-012-4449-6

7. Ni, Q., & Zhang, J. (2010). Dynamic visualization of cellular signaling. *Adv Biochem Eng Biotechnol, 119*, 79-97. doi:10.1007/10_2008_48

8. Prigent, C. (2017). *Protein Phosphorylation*: IntechOpen.

9. Wang, Y., Botvinick, E. L., Zhao, Y., Berns, M. W., Usami, S., Tsien, R. Y., & Chien, S. (2005). Visualizing the mechanical activation of Src. *Nature, 434*(7036), 1040-1045. doi:10.1038/nature03469

10. Wang, J., Voutetakis, A., Papa, M., Rivera, V. M., Clackson, T., Lodde, B. M., . . . Baum, B. J. (2006). Rapamycin control of transgene expression from a single AAV vector in mouse salivary glands. *Gene Ther, 13*(2), 187-190. doi:10.1038/sj.gt.3302647

11. Gossen, M., & Bujard, H. (1992). Tight control of gene expression in mammalian cells by tetracycline-responsive promoters. *Proc Natl Acad Sci U S A, 89*(12), 5547-5551. doi:10.1073/pnas.89.12.5547

12. Gossen, M., Freundlieb, S., Bender, G., Muller, G., Hillen, W., & Bujard, H. (1995). Transcriptional activation by tetracyclines in mammalian cells. *Science, 268*(5218), 1766-1769. doi:10.1126/science.7792603

13. Kallunki, T., Barisic, M., Jaattela, M., & Liu, B. (2019). How to Choose the Right Inducible Gene Expression System for Mammalian Studies? *Cells, 8*(8). doi:ARTN 79610.3390/cells8080796

14. Boyden, E. S., Zhang, F., Bamberg, E., Nagel, G., & Deisseroth, K. (2005). Millisecond-timescale, genetically targeted optical control of neural activity. *Nat Neurosci, 8*(9), 1263-1268. doi:10.1038/nn1525

15. Baker, M. (2011). Light tools. *Nature Methods, 8*(1), 19-22. doi:10.1038/Nmeth.F.322

16. Kennedy, M. J., Hughes, R. M., Peteya, L. A., Schwartz, J. W., Ehlers, M. D., & Tucker, C. L. (2010). Rapid blue-light-mediated induction of protein interactions in living cells. *Nature Methods, 7*(12), 973-U948. doi:10.1038/Nmeth.1524

17. Toettcher, J. E., Voigt, C. A., Weiner, O. D., & Lim, W. A. (2011). The promise of optogenetics in cell biology: interrogating molecular circuits in space and time. *Nature Methods, 8*(1), 35-38. doi:10.1038/Nmeth.F.326

18. Saboktakin, A., Ibarra-Castanedo, C., Bendada, A., & Maldague, X. P. V. (2010). *FINITE ELEMENT ANALYSIS OF HEAT GENERATION IN ULTRASONIC THERMOGRAPHY*.

19. Rohani, M., & Fasano, A. (2017). Focused Ultrasound for Essential Tremor: Review of the Evidence and Discussion of Current Hurdles. *Tremor Other Hyperkinet Mov (N Y), 7*, 462. doi:10.7916/D8Z89JN1

20. Thanou, M., & Gedroyc, W. (2013). MRI-Guided Focused Ultrasound as a New Method of Drug Delivery. *J Drug Deliv, 2013*, 616197. doi:10.1155/2013/616197

21. Guilhon, E., Voisin, P., de Zwart, J. A., Quesson, B., Salomir, R., Maurange, C., . . . Moonen, C. T. W. (2003). Spatial and temporal control of transgene expression in vivo using a heat-sensitive promoter and MRI-guided focused ultrasound. *Journal of Gene Medicine, 5*(4), 333-342. doi:10.1002/Jgm.345

22. Deckers, R., Quesson, B., Arsaut, J., Eimer, S., Couillaud, F., & Moonen, C. T. (2009). Image-guided, noninvasive, spatiotemporal control of gene expression. *Proc Natl Acad Sci U S A, 106*(4), 1175-1180. doi:10.1073/pnas.0806936106

23. Gross, G., Waks, T., & Eshhar, Z. (1989). Expression of Immunoglobulin-T-Cell Receptor Chimeric Molecules as Functional Receptors with Antibody-Type Specificity. *Proc Natl Acad Sci U S A, 86*(24), 10024-10028. doi:DOI 10.1073/pnas.86.24.10024

24. Rodriguez-Cartagena, L. G., Bowles, B. S., Kurani, S. S., Windebank, A. J., Kenderian, S. S., & Greenberg-Worisek, A. J. (2018). Chimeric Antigen Receptor T-Cells: Successful Translation of the First Cell and Gene Therapy From Bench to Bedside. *Cts-Clinical and Translational Science, 11*(6), 537-539. doi:10.1111/cts.12586

25. Boyiadzis, M. M., Dhodapkar, M. V., Brentjens, R. J., Kochenderfer, J. N., Neelapu, S. S., Maus, M. V., . . . Bishop, M. R. (2018). Chimeric antigen receptor (CAR) T therapies for the treatment of hematologic malignancies: clinical perspective and significance. *Journal for Immunotherapy of Cancer, 6*. doi:ARTN 13710.1186/s40425-018-0460-5

26. Kochenderfer, J. N., Wilson, W. H., Janik, J. E., Dudley, M. E., Stetler-Stevenson, M., Feldman, S. A., . . . Rosenberg, S. A. (2010). Eradication of B-lineage cells and regression of lymphoma in a patient treated with autologous T cells genetically engineered to recognize CD19. *Blood, 116*(20), 4099-4102. doi:10.1182/blood-2010-04-281931

27. Porter, D. L., Levine, B. L., Kalos, M., Bagg, A., & June, C. H. (2011). Chimeric Antigen Receptor-Modified T Cells in Chronic Lymphoid Leukemia. *New England Journal of Medicine, 365*(8), 725-733. doi:10.1056/NEJMoa1103849

28. Bonifant, C. L., Jackson, H. J., Brentjens, R. J., & Curran, K. J. (2016). Toxicity and management in CAR T-cell therapy. *Molecular Therapy-Oncolytics, 3*. doi:UNSP 1601110.1038/mto.2016.11

29. Morgan, R. A., Yang, J. C., Kitano, M., Dudley, M. E., Laurencot, C. M., & Rosenberg, S. A. (2010). Case report of a serious adverse event following the administration of T cells transduced with a chimeric antigen receptor recognizing ERBB2. *Mol Ther, 18*(4), 843-851. doi:10.1038/mt.2010.24

30. Fedorov, V. D., Themeli, M., & Sadelain, M. (2013). PD-1- and CTLA-4-based inhibitory chimeric antigen receptors (iCARs) divert off-target immunotherapy responses. *Sci Transl Med, 5*(215), 215ra172. doi:10.1126/scitranslmed.3006597

31. Kloss, C. C., Condomines, M., Cartellieri, M., Bachmann, M., & Sadelain, M. (2013). Combinatorial antigen recognition with balanced signaling promotes selective tumor eradication by engineered T cells. *Nat Biotechnol, 31*(1), 71-+. doi:10.1038/nbt.2459

32. Roybal, K. T., Rupp, L. J., Morsut, L., Walker, W. J., McNally, K. A., Park, J. S., & Lim, W. A. (2016). Precision Tumor Recognition by T Cells With Combinatorial Antigen-Sensing Circuits. *Cell, 164*(4), 770-779. doi:10.1016/j.cell.2016.01.011

33. Wu, C. Y., Roybal, K. T., Puchner, E. M., Onuffer, J., & Lim, W. A. (2015). Remote control of therapeutic T cells through a small molecule-gated chimeric receptor. *Science, 350*(6258), aab4077. doi:10.1126/science.aab4077

CHAPTER 2. IN-SITU COUPLING BETWEEN KINASE ACTIVITIES AND PROTEIN DYNAMICS WITHIN SINGLE FOCAL ADHESIONS

2.1. Introduction

Focal adhesions (FAs) are prominent intracellular molecular complexes containing hundreds of residential proteins, including integrin receptors, tyrosine kinases, and scaffolding proteins (*1-3*). Located at the interface of intracellular actin cytoskeleton and extracellular matrix, FAs undergo dynamic modifications involving their assembly, maturation, turnover, and disassembly (*1, 4*). FA proteins have been shown to form 3D nano-structures and move as slippery clutches in cells (*5, 6*). Increasing evidence indicates that FA dynamics is critically involved in important cellular processes, such as cancer metastasis, stem cell differentiation, and immune response, as well as biochemical and mechano-sensing of the surrounding microenvironment (*7-11*). While the dynamic regulation of FA proteins and their structural segregation have been under intense investigation, it remains unclear how molecular activities are coupled to the protein localization in guiding the FA assembly and disassembly dynamics at individual single FA sites.

The process of cellular adhesion, involves the dynamic regulation of FAs, with rapid assembly and turnover of FA complexes (*12, 13*). At the start of cell adhesion, integrin receptors at the cellular surface bind to matrix proteins, causing integrin activation and clustering to recruit adapter proteins and tyrosine kinases, such as paxillin, talin, Src family kinase (SFK) and focal adhesion kinase (FAK), to the initial FAs (*14*). These kinases can phosphorylate local substrate molecules and create docking sites for the recruitment and assembly of FA complexes (*15, 16*). The activation of tyrosine kinases coordinates with the transient increase of membrane tension to regulate FA traction force and FA turnover, as well as promote sustained cell spreading (*17-21*).

The complex roles of tyrosine kinases reflect a sophisticated and dynamic regulation mechanism in single FAs. To elucidate the dynamic roles of kinases in regulating FA kinetics, there is a great need for new imaging tools that allow the monitoring and analysis of multiple molecular events in single FAs.

Genetically encoded fluorescence resonance energy transfer (FRET) biosensors have been widely used to visualize subcellular molecular activities at single-cell level (*22, 23*). We have previously developed FAK and Src FRET biosensors and demonstrated their capabilities of monitoring the corresponding kinase activities with high sensitivity and specificity (*24, 25*). Utilizing these biosensors, we demonstrated that at the plasma membrane, most of the Src activation occurs outside the lipid-rafts microdomain (*26*), whereas FAK is mainly activated within the lipid-rafts microdomain (*25*). Here we have engineered novel FA-targeting (FAT) biosensors with the C-terminal FAT region of FAK, to monitor and track kinase activities at individual FA sites (*27-30*). Therefore, these FAT-Src and FAT-FAK biosensors should allow the visualization and quantification of the local Src and FAK activities, respectively, with single-FA precision.

While subcellularly targeted FRET biosensors enable the visualization of molecular signals with high resolution, computational analysis is indispensable for integrating multiple signals and deciphering regulatory parameters from live-cell images (*23, 31*) (*18, 32*). To elucidate the dynamic coupling between the biochemical kinase activities and structural FA dynamics we integrated the new FA-targeting biosensors, single-FA tracking, and cross-correlation analysis methods to quantitatively evaluate the temporal coordination of these molecular events at the single-FA level. Our analysis focused on elucidating the governing mechanism and temporal orders among the biochemical kinase activities and biophysical FA

dynamics in individual FAs during the adhesion of cancer cells. Such fundamental insights cannot be gained via traditional methods, because biochemical assays that average signals from a large number of cells and FAs cannot reveal the precise temporal coordination of molecular activations within single FA sites, especially if different FAs undergo non-synchronized regulations.

2.2. Results

2.2.1. FAT-FRET biosensors for monitoring Src and FAK kinase activities at single FA sites

To monitor local kinase activities with high spatiotemporal resolution, we engineered FRET-based Src and FAK biosensors to target to FAs, namely the FAT-Src and FAT-FAK biosensors (Figs. 2.1 and 2.2). The FAT-Src biosensor contains sequentially a Src SH2 domain, a flexible linker, and a Src specific substrate sequence, which are concatenated in between the enhanced cyan fluorescent protein (ECFP) and yellow fluorescent protein (YPet) FRET pair, with YPet connected to the FAT domain for FA localization (Fig. 2.1a). Active Src kinase can cause the tyrosine phosphorylation of the substrate and the subsequent increase of ECFP/FRET emission ratio (*24, 26, 33*). Therefore, the ECFP/FRET ratio can be used to represent subcellular Src kinase activity. Herein, we applied the FA-localized FAT-Src biosensor for reporting the Src activities within each individual FA site during cell adhesion.

MDA-MB-231 breast cancer cells expressing FAT-Src biosensors were seeded onto fibronectin-coated cover glass to allow cell adhesion and spreading (Fig. 2.1b and Supplementary Video 2.S1). As shown in a representative cancer cell (Figs. 2.1b and 2.1d), the intracellular ECFP/FRET ratio increased ~10% and ~40% of basal level at 30 min and 60 min after initial adhesion, respectively. Quantified results showed an average increase of ~40% in

ECFP/FRET ratio across multiple cells, clearly representing a significant Src activation during cell adhesion (Fig. 2.1e). The intensity profile of the FAT-Src biosensor showed a clear FA localization in clusters at the cell periphery, although diffusive fluorescence signals were seen at perinuclear structures, possibly reflecting that some biosensor cargoes were trapped during the transportation process after protein synthesis (Fig. 2.1b). These results indicate that FAT-Src biosensors correctly localize to FAs and can be used to visualize Src activation within these individual structures with high sensitivity during cell adhesion.

To confirm the localization of the FAT-Src biosensor, the YPet intensity pattern of the biosensor was compared with that of the FA protein, mCherry-paxillin. As shown in Fig. 2.1f and Figs. 2.S1a and 2.S1b, the YPet signals overlapped with mCherry-paxillin throughout the adhesion process at cell periphery. Slightly more paxillin was observed at perinuclear regions than biosensor signals, probably representing diffusive background of unprocessed fusion proteins trapped in organelles such as Golgi complex and ER (Fig. 2.1f). Correlation analysis showed a high time-average Pearson coefficient of 0.986±7e-4 between the two images (Fig. 2.S1). This co-localization was observed in all four cells studied with FAT-Src biosensors and mCherry-paxillin. Therefore, our results indicate that the FAT-Src biosensors are recruited to peripheral FAs and undergo turnover with similar spatiotemporal dynamics as the FA protein paxillin.

Both the original FAK and Src biosensors have been thoroughly examined and characterized to demonstrate a high specificity toward their desired target kinases (*34, 35*). The addition of fusion tag FAT is expected to enhance the subcellular efficiency without altering the specificity of these biosensors. Nevertheless, to further characterize the specificity of our FAT-Src biosensor, cells expressing the biosensors were treated with the SFK inhibitor PP1 and

monitored during the adhesion process. PP1 pretreatment (10 µM for 1 hr) significantly blocked

the adhesion process, as ~50% of the cells did not attach, indicating the importance of SFK

kinase activity in adhesion. In the group of PP1-treated cells that did adhere, the quantified Src

ECFP/FRET ratio showed significantly reduced values (Figs. 2.1c-2.1e and Supplementary

Video 2.S2). The cells treated with PP1 also had less expansion with a reduced number of FAs

than those without PP1 (Figs. 2.1c-2.1d and Supplementary Video 2.S2). Taken together, these

results indicate that our FAT-Src biosensors can specifically detect dynamic Src kinase

activation in single FAs, which is important for cancer cell adhesion and expansion.

Using a similar strategy, we engineered a FAT-FAK biosensor (*34*) (Fig. 2.2a). The FAT-

FAK biosensor allowed the visualization of FAK activation with high sensitivity during the

adhesion process of MDA-MB-231 cells (Fig. 2.2b and Supplementary Video 2.S3). Again, the

majority of FAT-FAK biosensors localized correctly to FAs, with some appeared at perinuclear

regions. A representative cell showed ~22% increase of ECFP/FRET ratio during adhesion (Fig.

2.2c). Pretreatment of the cells with PF228 (FAK inhibitor, 1 µM for 1 hr) blocked cell adhesion,

while the addition of PF228 (1 µM) during imaging caused a significant decrease in the

ECFP/FRET ratio of the biosensors, confirming the specificity of the FRET signals (Figs. 2.2c-

2.2d). These results demonstrate that our FAT-FAK biosensors can be used to monitor FAK

activation at single FAs during the adhesion of cancer cells with high sensitivity and specificity.

In a cell expressing both the FAT-FAK biosensor and mCherry-paxillin, YPet signals

overlapped precisely with mCherry patterns with a time-averaged Pearson coefficient of

0.994±9e-5 during adhesion (Fig. 2.S1c), indicating that the FAT-FAK biosensor and paxillin

were highly co-localized. Quantitative plots confirmed similar dynamics between FAT-FAK-

YPet and mCherry-paxillin (Fig. 2.S1d). This co-localization was observed in all five cells co-

expressing FAT-FAK biosensors and mCherry-paxillin. Therefore, the YPet signal of the FAT-FAK biosensor can be used to assess and quantify the dynamic recruitment and turnover of the FA structure highlighted by paxillin (*36, 37*). In addition, YPet images were collected with YPet excitation and YPet emission, which is different and independent of FRET images collected by ECFP excitation and YPet emission. As a result, a single transfection of a FAT-biosensor can allow the simultaneous tracking and quantification of the biochemical kinase activity (via ECFP/FRET ratio) and the biophysical FA dynamics (via YPet intensity).

To examine the general applicability of our FA-tagged FRET biosensors, we transfected the biosensors into a different cell line, mouse embryonic fibroblasts (MEFs), and monitored the adhesion process. Similar to that in the MDB-MD-231 cells, the FAT-Src biosensors in MEF cells localized to FAs, with the ECFP/FRET ratio increased ~50% in 30-60 minute after adhesion (Fig. 2.S2). Meanwhile, MEF cells expressing the FAT-FAK biosensors also showed correct FA-localization and ~30% increase in the ECFP/FRET ratio after adhesion (Fig. 2.S2). Altogether, these results indicate that our FA-targeted FRET biosensors provide new tools to visualize and quantitatively analyze kinase activities in single FAs and that the FA-target strategy has general utility in engineering FRET biosensors for monitoring molecular activities with subcellular resolution.

2.2.2. Quantification of kinase activities and FA dynamics in single FAs by feature detection and single-FA tracking during adhesion of cancer cells

During the adhesion process, cells undergo dramatic expansion and FAs are highly dynamic. The fluorescence intensity images of the MDA-MB-231 breast cancer cells were significantly smaller and brighter at the beginning of adhesion than those after adhesion, with

~10-fold increase of the cell area (Figs. 2.1-2.2). In general, there were no visible FAs initially. When the FAs became detectable in the YPet intensity images, the number of FAs quickly increased to 20 or more per cell within 30 min (Figs. 2.1 and 2.2). Meanwhile, cells expanded before they started migration. Such drastic changes in cell shape and FA dynamics require accurate detection and tracking methods to precisely quantify the local kinase activities and FA dynamics at single FA sites.

The cell body was detected using the biosensor YPet images. Because of the marked change of YPet intensity profile during adhesion, Otsu's method with an adaptive detection threshold was used to calculate the mask of the cell body (*24*). The threshold was adapted continuously according to the decreasing YPet intensity resulted from cell spreading. In some cases, the YPet images of the cell did not have a uniform intensity profile around the cell boundary (Fig. 2.3a). As a result, segmentation based on a global threshold could not precisely detect parts of the cell boundaries (Fig. 2.3a). To address this problem, a two-step adaptive thresholding method was used to improve detection accuracy. First, we generated a basic cell boundary using a global threshold. Second, we detected the local thresholds and masks within a moving rectangle along the basic boundary by Otsu's method (Fig. 2.3a). The local masks were then merged and smoothed to calculate the refined whole-cell boundary and mask (Fig. 2.3a). This two-step adaptive thresholding method improved the accuracy of cell boundary detection (Fig. 2.3b), and is robust for changing cell shapes and intensity profiles during adhesion.

After cell boundary detection, the FAs were subsequently detected using the modified water algorithm via high pass filter and thresholding (*18*). The size of the high-pass filter was adjusted according to the cell size, allowing the accurate detection of dynamic FAs during adhesion (Fig. 2.3c). The cells were divided into layers based on the distance from each image

pixel to the background region outside of the cell, allowing the determination of ECFP/FRET ratio and YPet intensity of FAs in the outermost layer composed mainly of lamellipodia regions (Fig. 2.3c).

Single-FA tracking is essential for the quantitative investigation of biosensor signals, FA dynamics, and their coordination at individual FA sites, since the average signals from a large number of cells or FA sites cannot reveal the precise coordination of molecular activations as different FAs generally undergo non-synchronized regulations. The single particle tracking algorithm developed by Jaqaman et al. was hence adopted here to track the detected FAs via optimization (*38*) (Fig. 2.3d). We developed an interface program to overlay track numbers on the FA images, allowing a visual evaluation of the tracking accuracy. For the purpose of studying the molecular regulation of the assembly and disassembly of FAs, we focused on the FA population that grew or shrank in size, but did not split or merge. Hence, we used the these tracks of FAs for the quantification of the time courses of ECFP/FRET ratio and YPet intensity, as well as the subsequent analysis deciphering the coupling between the biochemical kinase activities and structural FA dynamics at individual FA sites.

2.2.3. Src activation leads FAK activation following the initiation of FA assembly

Throughout the dynamic adhesion process of the MDA-MB-231 cells, some FAs continued to assemble and eventually matured, while others turned over or disassembled as depicted in the schematic plot (Fig. 2.4a). In contrast to the relatively smooth curves for FA intensity, the kinase activity shows more time-variance, with an overall rising phase accompanied by oscillatory patterns in time (Fig. 2.4a).

We first investigate the FA assembly phase. It has been reported that kinases are recruited to FA sites and activated to cause a positive feedback loop of phosphorylation, recruitment, and activation during FA assembly (*4, 39, 40*). To investigate the sequential regulation between kinase activation and FA assembly, we first focused on the rising phase of ECFP/FRET ratio signals, which represents kinase activation, and that of YPet intensity, which represents FA assembly (Figs. 2.4b-2.4d and Supplementary Videos 2.S4-2.S5). No significant photobleaching was observed with our imaging setting (Fig. 2.S3a) and evidenced in our previous publications (*34, 35*). Cross-correlation analysis (*18, 32*) was performed to evaluate the temporal phase difference between FA structural changes and kinase activation (Fig. 2.4e). In representative FAs, the cross-correlation function showed a positive time delay between the dynamics of YPet intensity and FAT-FAK ECFP/FRET ratio (Fig. 2.4b), indicating that FA assembly led FAK activation at this FA, while Src activation and FA assembly occurred nearly concurrently (Figs. 2.4b-2.4e).

Cross-correlation analysis on multiple individual FAs showed a significant difference between the distributions of the time delays in FA-FAK and FA-Src correlations (Fig. 2.4f). These time delays were independent of the average YPet intensity of the corresponding FAs (Figs. 2.S3b and 2.S3c), suggesting that targeting our biosensors with Src or FAK substrates at FAs did not significantly perturb the endogenous molecular dynamics. Taken together, our results indicate that FA assembly occurred significantly earlier than FAK activation by 42.6±12.6 sec, but not Src activation, with an FA-Src time lag of 10.8±10.2 sec (Fig. 2.4g). The high peak values of the FA-FAK and FA-Src cross-correlations indicate a strong coupling between FA assembly and kinase activation (Fig. 2.4h). Although the FAT-Src and FAT-FAK activities were monitored in different cells, cross-correlation analysis allowed the quantitative

evaluation of the Src and FAK activation sequence using FA signal as a common reference. Therefore, these results suggest that during FA assembly and growth, Src kinase is activated almost concurrently with FA assembly, which is on average 42.6 sec earlier than FAK activation at individual FA sites.

2.2.4. The fate of individual FAs reflected by the kinase-FA coupling and regulated by the successive activations of FAK and Src

To study the role of the kinases in determining the fates of FAs during disassembly, we separated the FA populations into matured (FA intensity increased or remained stable for 6 min or more) and disassembled (FA intensity peaked and then decreased) subgroups. Interestingly, the matured FAs in cells with the FAK biosensor had a sharp distribution of the time delay between FA assembly and kinase activation, with a mean value of 16.4±9.4 sec (not significantly different from 0 sec, Fig. 2.5a), indicating nearly concurrent rises of FA intensity and kinase activity. In contrast, the disassembled FAs in cells with the FAK biosensor had a relatively dispersed distribution of the time delay between FA assembly and kinase activation with a significantly larger mean value of 69.6±20.6 sec (Fig. 2.5a), suggesting that FA assembly led kinase activation by ~1.2 min in this group. Similar difference between the two groups of FAs also exists in cells with the Src biosensor, with the matured FAs having a sharp distribution of the time delay centered at -25.9±16.4 sec (not significantly different from 0 sec), while the disassembled FAs having a significantly wider distribution centered at 69.5±25.8 sec (Fig. 2.5a, insert). Statistical analysis shows a significant difference in the standard deviations of the time delays between the matured and disassembled FAs, which indicates distinct couplings between FA assembly and kinase activation in these two FA groups. It is of note that a wider distribution

of FA-kinase time delay in the disassembled FAs can represent a less coordinated FA dynamics with its associated kinase activation and perhaps reflecting the dynamic instability of these FAs. This result suggests that, at the time of assembly, the fate of a FA to disassemble or to mature can be reflected by its FA-kinase coordination. FAs with tight coupling of FA-kinase have a high chance to mature and stabilize, while those with loose FA-kinase coupling mostly disassemble (Fig. 2.5a).

To probe further into the dynamic coupling between kinase activities and FA disassembly, we focused on the group of disassembled FAs. It has been documented that the activation of FAK/Src kinases at the FA site can lead to the disassembly of that FA (*17*). To verify this notion in our system, we treated cells with the FAK inhibitor PF228 (1 μM) after the cells had stopped spreading. The inhibition of FAK activity reduced the FAK ECFP/FRET ratio and caused a more persistent FA growth than that in untreated cells (Fig. 2.5b and Supplementary Video 2.S6). The persistency of FA growth was quantified from the ratio between the duration of the rising phase of YPet intensity and the total time course studied in individual FAs before or after inhibitor treatment. As shown in Figs. 2.5b-2.5c, the persistency of FA growth significantly increased after PF228 treatment from 34±9% to 70±13%. In fact, the intensities of the majority of FAs kept increasing till the end of imaging, which was about 36 min after the addition of PF228. These results suggest that the inhibition of FAK leads to stabilization of FAs and that FAK activity plays an indispensable regulatory role in FA disassembly and turnover. This is also consistent with previous observations of a hindered FA disassembly in cells lacking FAK (*17*) or SFKs (*18*).

With the causal relationship between kinase activity and FA disassembly established, we proceeded to examine the temporal coordination between these two molecular events by

investigating the time delay, Δt, defined as the temporal difference between the starting point of the FA disassembly phase and its associated kinase activation phase (Fig. 2.5d). This approach avoids the difficulty of performing direct cross-correlation between kinase activation and FA disassembly engendered from multi-phasic oscillations of kinase activities during the lifetime of these disassembled FAs. FAK and Src ECFP/FRET ratio images and quantified time courses from representative FAs both showed an increase of kinase activities before the start of FA disassembly (Figs. 2.5e-2.5g and Supplementary Videos 2.S7-2.S8). The average Δt in cells with the FAK biosensor was 4.5±0.54 min, significantly larger than that of 2.5±0.3 min in cells with the Src biosensor (Fig. 2.5h). By using the event of FA disassembly as a time reference, these results indicate that, at the single-FA level, the rising of biochemical FAK activity initiates ~2.0 min earlier than that of Src, which then lead to the structural FA disassembly in another ~2.5 min.

Since the histogram of Δt from individual FAs is similar to Poisson distribution, we fitted the histogram to the Poisson probability density function with least-squares approximation to obtain the parameter λ, the average time passed between the proceeding kinase activation wave and the start of FA disassembly. The fitted values of the time parameter l confirmed that FAK activity rose ~2.0 min before Src activation in regulating FA disassembly (Fig. 2.5i). Since the distribution of Δt fits the Poisson probability density function, this result suggests that the sequential activation of kinases may trigger FA disassembly via stochastic regulations, which occur in a time scale of minutes.

2.3. Discussion

FAs are actively involved in mechanosensing, force transducing, and outside-in signaling during cell adhesion and expansion (*9, 20*). FAK and Src play key roles in the precise and fine regulation of the FA dynamics (*15, 17*). Our understanding on the regulatory functions of FAK and Src about FAs is mainly based on averaged signals from a large number of different cells/FAs at the global level, which can cause inaccuracies as individual FAs are generally not synchronized. Currently, there is a lack of imaging and analysis tools to quantitatively evaluate the temporal coordination among these different molecular events at individual FA sites. In this work, we engineered and characterized the FAT-Src and FAT-FAK FRET biosensors to precisely localize at individual FA sites and monitor the kinetic changes of Src and FAK activities, as well as the local FA structural change. With the aid of automated feature-detection and single particle tracking methods, we quantified the time sequences of FAK and Src kinase activation and FA intensity in a single FA throughout its dynamic lifespan during cell adhesion. By cross-correlation-based analysis (*18*), we unraveled the kinetic coupling between the biochemical kinase activity and the biophysical structural dynamics at the single-FA level. Our results suggest that the FA complex assembly and its concurrent Src activation lead to a full-scale activation of FAK in ~40 sec. In guiding FA disassembly, however, the activation of FAK leads a wave of Src activation in minutes prior to the FA structural disassembly. Our analysis should thus provide a quantitative and precise understanding of the kinetic coupling among the molecular events within single FA complex during cell adhesion.

During the adhesion process, cells go through three major phases: the initial attachment (P0), rapid spreading (P1), and slow spreading (P2) (*12, 20*). Toward the end of P1 phase, the early FA proteins associated with integrin clusters, e.g., paxillin, talin, and FAK, recruit and

activate Src kinase and formin to induce actin polymerization (*15, 41*). Subsequently, the force generated by actin flow and myosin contraction recruits vinculin and triggers FA maturation and cell spreading (*16, 42, 43*). It is conceivable that the initial recruitment of kinases and the subsequent phosphorylation of substrate molecules within an FA complex facilitate the further recruitment of proteins for FA assembly. As the kinase activities accumulate, the FA proteins are hyper-phosphorylated to cause competing protein interactions within the complex, which may, together with the developed tension at the local site, lead to FA turnover or disassembly. As such, the fate of FA stabilization and turnover can be determined by the coordinated interplay of local biochemical kinase activities, biophysical force, and the molecular status of an FA. Our work highlights the roles played by FAK and Src kinases during this process, and provides a timeline of these sequential signaling events in the lifetime of an FA.

Our results revealed that FA assembly and the concurrent Src activation led FAK activation by ~43 sec in individual FAs. Although Src activation has been reported to precede FAK activation in cancer cell adhesion (*44*), it is generally understood that FAK autophosphorylation at Y397 site was required for the recruitment of Src at the FA sites to fully activate FAK (*45-47*). It is possible that the initial FAK autophosphorylation is relatively weak before the recruitment and activation of Src to turn on the full-scale activation of FAK, which then becomes detectable by the FAT-FAK biosensor (*29, 39*). A more sensitive FAK FRET biosensor may be needed to monitor this biphasic FAK activation, with the initial autophosphorylation and activation of FAK followed by a full-scale activation mediated by the Src recruitment and activation.

It is of note that there is a narrow distribution of cross-correlation time delays between the FA assembly and kinase activation in the matured FAs, suggesting a relatively coordinated

coupling between FA structure and kinase regulations. In contrast, the time delays in disassembled FAs are significantly longer and dispersed across a wide range, suggesting a relatively stochastic decision-making process in the disassembled FAs. In fact, it appears that the fate of FA may have been determined during the assembly phase, with individual FAs having tight coupling between kinase activation and FA assembly inclining toward growth and maturation. It is possible that disassembled FAs are at locations where the subcellular microenvironment is less stable initially and hence require varied time periods to reach a deterministic process. In fact, oscillatory kinase activation waves can be observed in these disassembled FAs, possibly reflecting multiple rounds of adaptations and alterations of local biochemical processes.

Different from the assembly phase, FA disassembly was demonstrated to be closely regulated by FAK and Src in our present and previous studies (*17, 18*). Our results suggest that FA disassembly follows the successive risings of FAK and Src activities within 4.5 minutes. As such, we propose a regulatory network within individual FA sites where Src activation leads a full-scale FAK activation after both Src and FAK are recruited during FA assembly. After reaching equilibrium, some FAs mature and become stabilized. Among the others that are destined to turnover, the full activation of FAK leads another wave of Src activation in triggering FA disassembly (Fig. 2.6). FAK may hence serve as a decision maker to switch FA from assembly toward disassembly phase in these turnover FAs, possibly via the accumulated FAK activity and its resulted hyper-phosphorylation of FA proteins aided by the lagging Src activation.

In summary, via the utilization of the newly designed FAT-FRET biosensors targeted at the subcellular individual FA sites, we have successfully monitored the active molecular events

during cancer cell expansion upon adhesion. Single particle tracking and cross-correlation analysis provide powerful tools for the precise quantification of the temporal coordination among the biochemical activities of FAK and Src and the structural dynamics of the FA at the single-FA level. Unraveling the time sequence of FAK and Src activation dynamics at local FA sites should advance our in-depth understanding on how these crucial molecular events are coordinated to govern the cell adhesion that serves as a pivotal step for cancer cell metastasis to secondary sites. This understanding should also allow the design of new therapeutic approaches optimizing the inhibitor combinations and applications.

2.4. Acknowledgements

2.5. Methods

2.5.1. Focal adhesion (FA) targeting FRET biosensors

To engineer the FAT-FAK biosensor, a PCR product of the FAK-FAT domain with KpnI and EcoRI sites are first fused to the C-terminal of the cytosolic FAK biosensor (ECFP, SH2 domain, FAK substrate, and YPet) in pRSETB and the vector was replaced to pcDNA3.1 with BamHI/EcoRI sites for the mammalian expression (*25, 34*). To create the FAT-Src biosensor in pRSETB, the FAK biosensor part of pRSETB-FAT-FAK biosensor was replaced with a PCR product of the cytosolic Src biosensor (ECFP, SH2 domain, Src substrate, and YPet) containing BamHI/KpnI sites. For the mammalian expression, the pRSETBvector was further replaced by pcDNA3.1 with BamHI/EcoRI sites, generating FAT-Src biosensor in pcDNA3.1.

2.5.2. Cell culture and reagents

Human breast cancer cells (MDA-MB-231) were cultured in DMEM supplemented with 10% fetal bovine serum (FBS), 2 mM L-glutamine, 100 unit/ml penicillin, 100 μg/ml streptomycin, and 1 mM sodium pyruvate (GIBCO BRL). Cells were maintained in a humidified 95% air, 5% CO_2 incubator at 37°C. Lipofectamine 2000 (Invitrogen) was used in the transfection of different DNA plasmids. The typical amounts of plasmids were 1.5 – 2.0 μg for single transfection of FAT-FAK or FAT-Src, and 1.0 – 1.5 μg each for co-transfection with mCherry-paxillin.

Cells expressing various exogenous proteins were starved in cell culture medium with 0.5% FBS for 36 hr before passing onto fibronectin-coated glass bottom dishes (Cell E&G) overnight prior to imaging. This step also served the purpose of synchronizing the status of cell cycle and reducing its effect on the variation of intracellular protein expression and molecular

wiring. The dishes were incubated with FN solutions (20 mg/ml) at 37°C for 4 hr before usage.

For inhibitor experiments, cells with FAT-Src biosensors were pre-treated with the Src inhibitor

PP1 (10 μM, BioMol) for 1 hour. A specific FAK inhibitor PF573228 (PF228, 1 μM, Pfizer) was

added to cells with FAT-FAK biosensors during imaging (25). PP1 and PF228 were dissolved in

DMSO in stock solution (100 mM) and then further diluted in DMEM imaging medium before

experiments.

2.5.3. Image acquisition and analysis

Prior to microscopy imaging, the cells were transferred to Agarose gel dishes and

suspended for 1 hr. The cells were then collected and transferred to glass bottom dishes for

imaging of the adhesion process. Images were collected by a Zeiss Axiovert inverted microscope

equipped with 1003 objective (1.4 NA) and a cooled charge-coupled device camera (Cascade

512 B; Photometrics) using the MetaFluor 6.2 software (Universal Imaging). The parameters of

dichroic mirrors, excitation and emission filters for different fluorescence proteins were

described previously (33). In brief, the FAT-Src/FAK biosensors were excited at 420±20 nm,

and the emissions collected at 475±40 nm or 535±25 nm for ECFP or FRET images,

respectively. The YPet images were obtained by excitation at 495±10 nm and emission at

535±25 nm. The mCherry-paxillin probe was excited at 560±40 nm and the emission collected at

653±95 nm for mCherry images. These excitation and emission settings were selected to allow

optimal FRET efficiency and minimal bleed-through among FRET, YPet, and mCherry

channels. Meanwhile, we minimized photobleach by reducing laser excitation duration and

introducing neutral density filters to reduce excitation intensity, yet collect sufficient signals via

a highly sensitive camera (Cascade II). As such, we will be able to obtain time-lapse images of single live cells without significant photobleach.

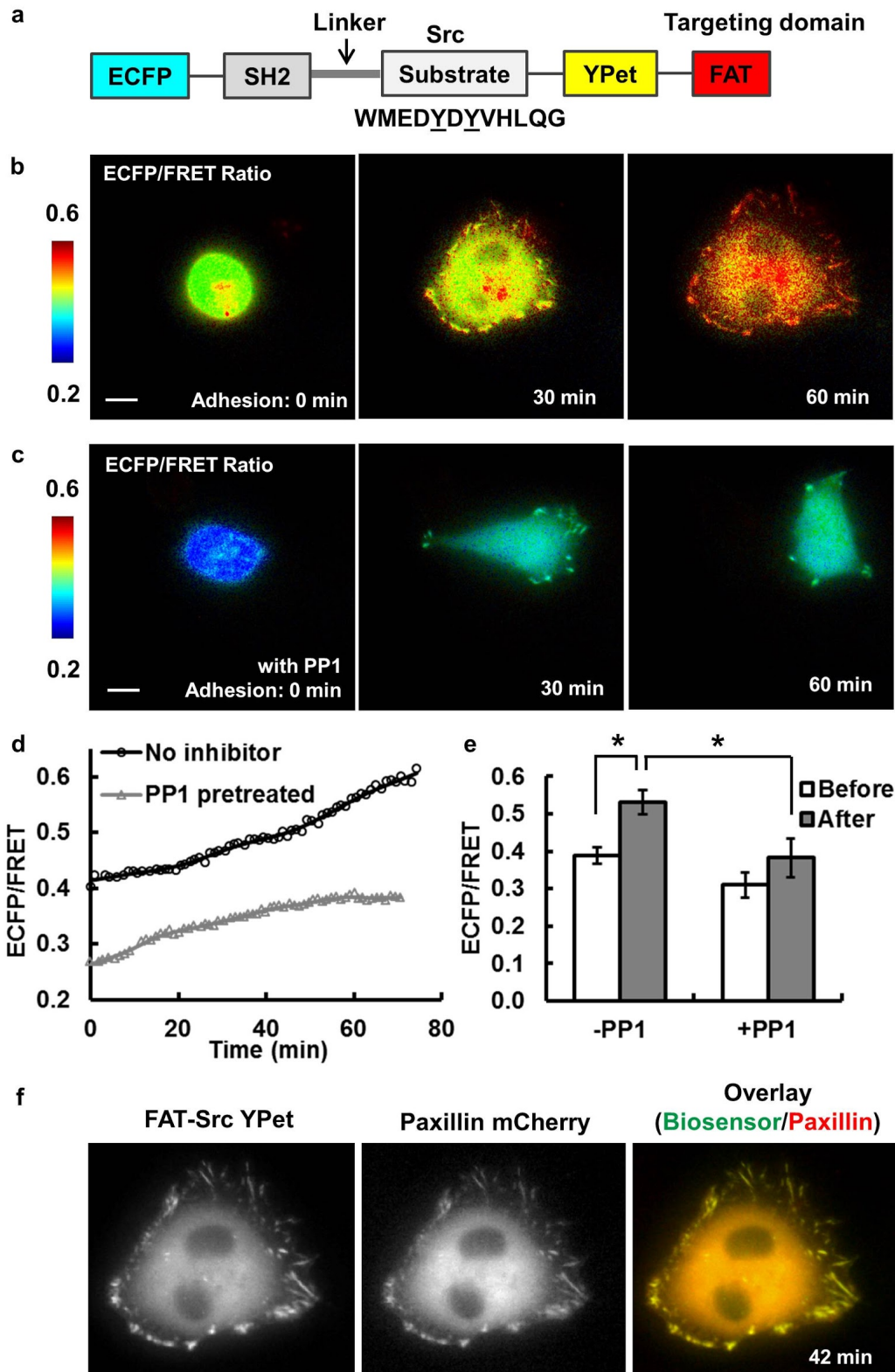### 2.5.4. Quantification and cross-correlation analysis

In signal processing, cross-correlation measures the similarity and time delay/difference between two signals. Cross-correlation analysis was applied in this study to reveal the dynamic coordination among FA dynamics (represented by the YPet intensity of the biosensors) and FAK, Src activities (represented by the ECFP/FRET ratio of the corresponding biosensors in cancer cell adhesion. We used the cross-correlation algorithm developed by Lu et al. to determine the time delay between FA assembly and kinase activations (*18*). Instead of padding with zeros, the program extended the signals to a longer length using their end values and thus provided accurate results for slow and non-oscillatory signals, such as those observed during FA assembly and turnover. Both signals were normalized such that the maximum of the cross-correlation was one. The time-axis of the maximum of the cross-correlation function gives the time delay between the two signals analyzed. Since FAK and Src activities were not simultaneously monitored in the same cell, the FA dynamics served as a common reference in the temporal comparison between the two kinase activities.

2.5.5. Statistical analysis

The Bonferroni multiple comparison test of means at 95% confidence interval was applied for the statistical analysis in Fig. 2.1e using a customized program based on the *multcompare* function in Matlab (The MathWorks, Natick, MA) (*48*). Similarly, a paired multiple comparison test was performed for the statistical analysis in Fig. 2.2d using the same

program. Two-tailed paired Student's t-test (Type 1 TTEST, Excel) was used to compare the proportions of YPet intensity rising phase in the same FA before and after PF228 treatment in cells with the FAT-FAK biosensor in Fig. 2.5c. For the analysis in the assembly phase in Fig. 2.4f, the Kolmogorov-Smirnov test (kstest2, MATLAB) was utilized to compare the distributions of the time delays between FA assembly and kinase activation in cells with FAT-FAK and FAT-Src biosensors. To analyze the shapes of the cross-correlation time delay distributions in the matured and disassembled FAs, the randomized test (bootstrp, MATLAB) was used to compare the standard deviations of the distributions. For the rest of results, two-tailed two-sample Student's t-test assuming different variances (Type 3 TTEST, Excel) was employed for the statistical analyses if not otherwise specified.

Figure 2.1. Engineer and characterize the focal-adhesion-targeting FAT-Src FRET biosensor. (a) The schematics of the FA-targeting Src FRET biosensor. **(b)** The ECFP/FRET ratio images of a representative cell during the adhesion process. **(c)** The ECFP/FRET ratio images of a control cell pretreated with Src inhibitor PP1. **(d)** The time courses of the ECFP/FRET ratio in the cell shown in (b) (black line with circles) and that in (c) (gray line with triangles). **(e)** The average ECFP/FRET ratio values before (0-3 min, white) and after (33-36 min, gray) the appearance of FAs in cells with ($N1 = 8$) or without PP1 treatment ($N2 = 5$). * indicates significant difference by Bonferroni multiple comparison test *(p < 0.05)*. **(f)** The YPet intensity (left) and mCherry image (middle) of a cell co-transfected with the FAT-Src biosensor and mCherry paxillin, with the overlaid image shown on the right. Scale bar: 10 μm.

a

ECFP — SH2 — Linker↓ — Src Substrate — YPet — Targeting domain FAT

WMED<u>Y</u>D<u>Y</u>VHLQG

b

ECFP/FRET Ratio

0.6

0.2

Adhesion: 0 min | 30 min | 60 min

c

ECFP/FRET Ratio

0.6

0.2

with PP1 Adhesion: 0 min | 30 min | 60 min

d

- ○ No inhibitor
- △ PP1 pretreated

ECFP/FRET

Time (min)

e

ECFP/FRET

□ Before
■ After

-PP1   +PP1

f

FAT-Src YPet | Paxillin mCherry | Overlay (Biosensor/Paxillin)

42 min

34
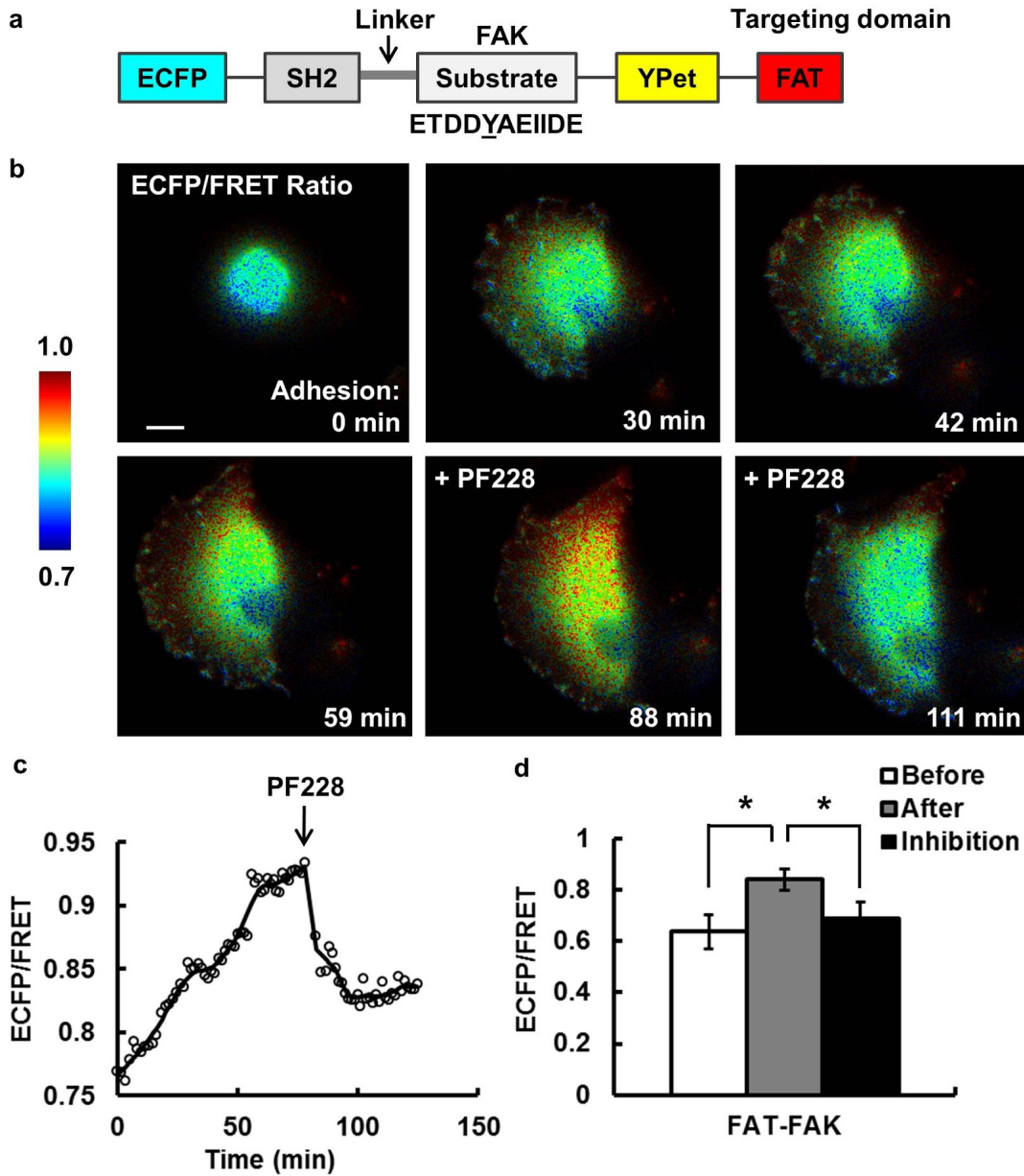
Figure 2.2. The FAT-FAK FRET biosensor is sensitive and specific in detecting FAK activity in live cells. (a) The schematics of the FAT-FAK FRET biosensor. **(b)** The ECFP/FRET ratio images of a representative cell before and after adhesion, and that after FAK inhibition. **(c)** The time course of the average ECFP/FRET ratio in the cell shown in (b). **(d)** The average ECFP/FRET ratio values before (0-4 min, white) and after (75-78 min, gray) the appearance of FAs, and that after inhibitor treatment (~105-108 min, 0.69±0.067, black). * indicates significant difference from the other groups by a paired Bonferroni multiple comparison test (*p <0.05, N = 3*). Scale bar: 10 μm.

Figure 2.3. Cell and FA detection and tracking. (a) Detection of the cell boundary and subsequent refinement using local threshold values. **(b)** Comparison of the detected cell boundaries before (green) and after (red) refinement on a DIC image. **(c)** The detection schematics of FAs at the cell periphery. **(d)** The trajectories (white) of the well-tracked individual FAs that did not merge or split in a representative cell. The rainbow colors represent FAs at different time points in chronological order, with violet representing the FAs from the earliest frame and red the latest. Arrows indicate the direction of the FA translocation during the adhesion process.
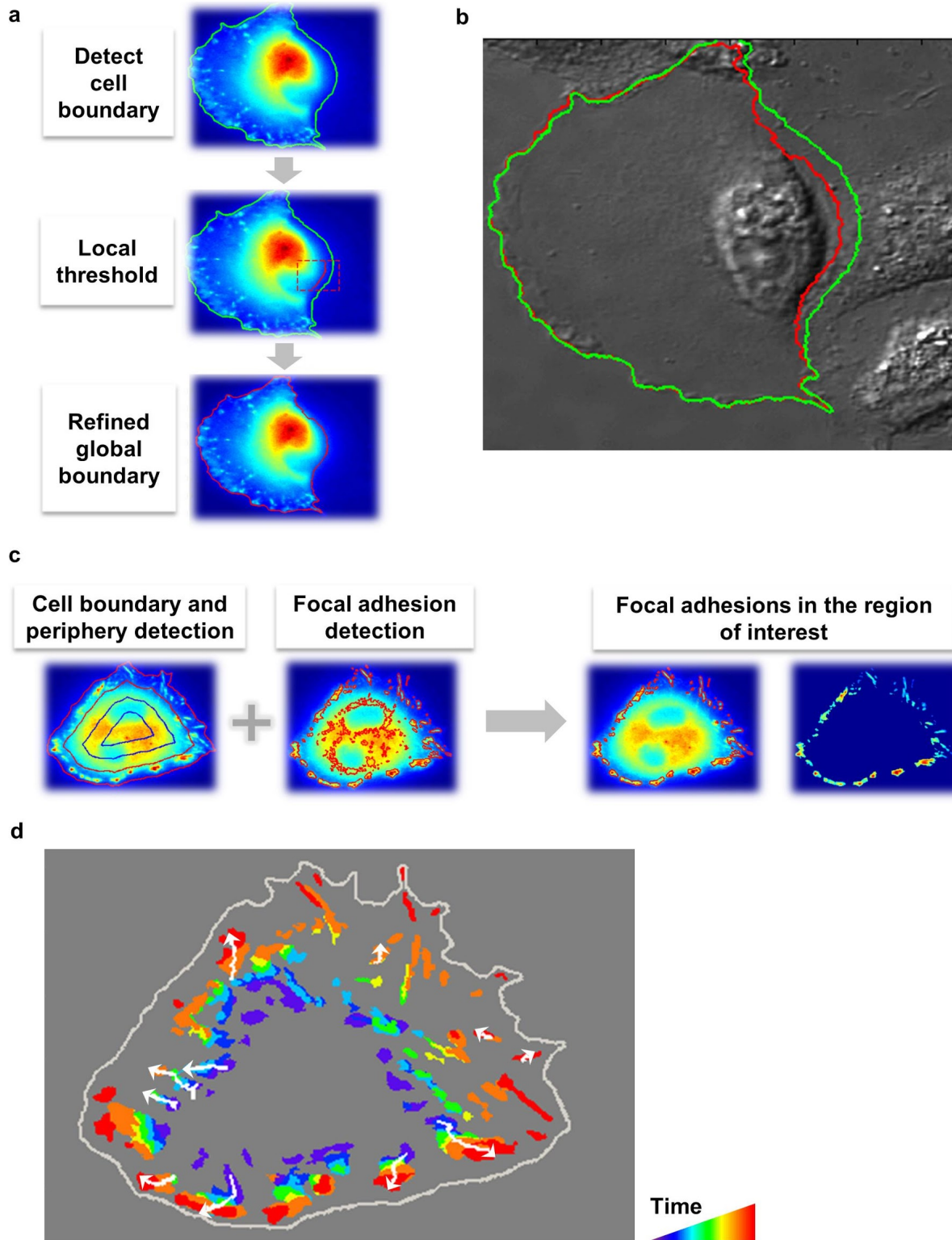
Figure 2.4. FA assembly leads the sequential activation of Src and FAK kinases. (a) The schematic of the typical kinase activity and total FA intensity kinetics at a single FA, with the rising phases shown in dark solid lines. The lines in light colors illustrate the variations in YPet intensity ECFP/FRET ratio trend among different individual FAs. In (**b-c**), the YPet intensity images of a representative FA color-coded by its ECFP/FRET ratio (top row) or by total FA YPet intensity (bottom row) in cells with either **(b)** FAT-FAK or **(c)** FAT-Src biosensors. **(d)** The time courses of the rising phases of ECFP/FRET ratio (red) and YPet intensity (blue) in representative FAs from different individual cells with either FAT-FAK (solid; images shown in panel b) or FAT-Src (dashed; images shown in panel c) biosensors. **(e)** The intensity-ratio cross-correlation functions calculated from the time courses in (b-c). **(f)** The histograms of the time delay, **(g)** the average time delays and **(h)** the cross-correlation peak values between the rising of YPet intensity and that of ECFP/FRET ratio in single FAs are compared between cells with the FAT-FAK biosensor (number of FAs: $n = 35$; number of cells: $N = 6$) and those with the FAT-Src biosensor (number of FAs: $n = 53$; number of cells: $N = 10$). * indicates statistically significant difference ($p < 0.05$). Error bar: SEM. Scale bar: 5 μm.
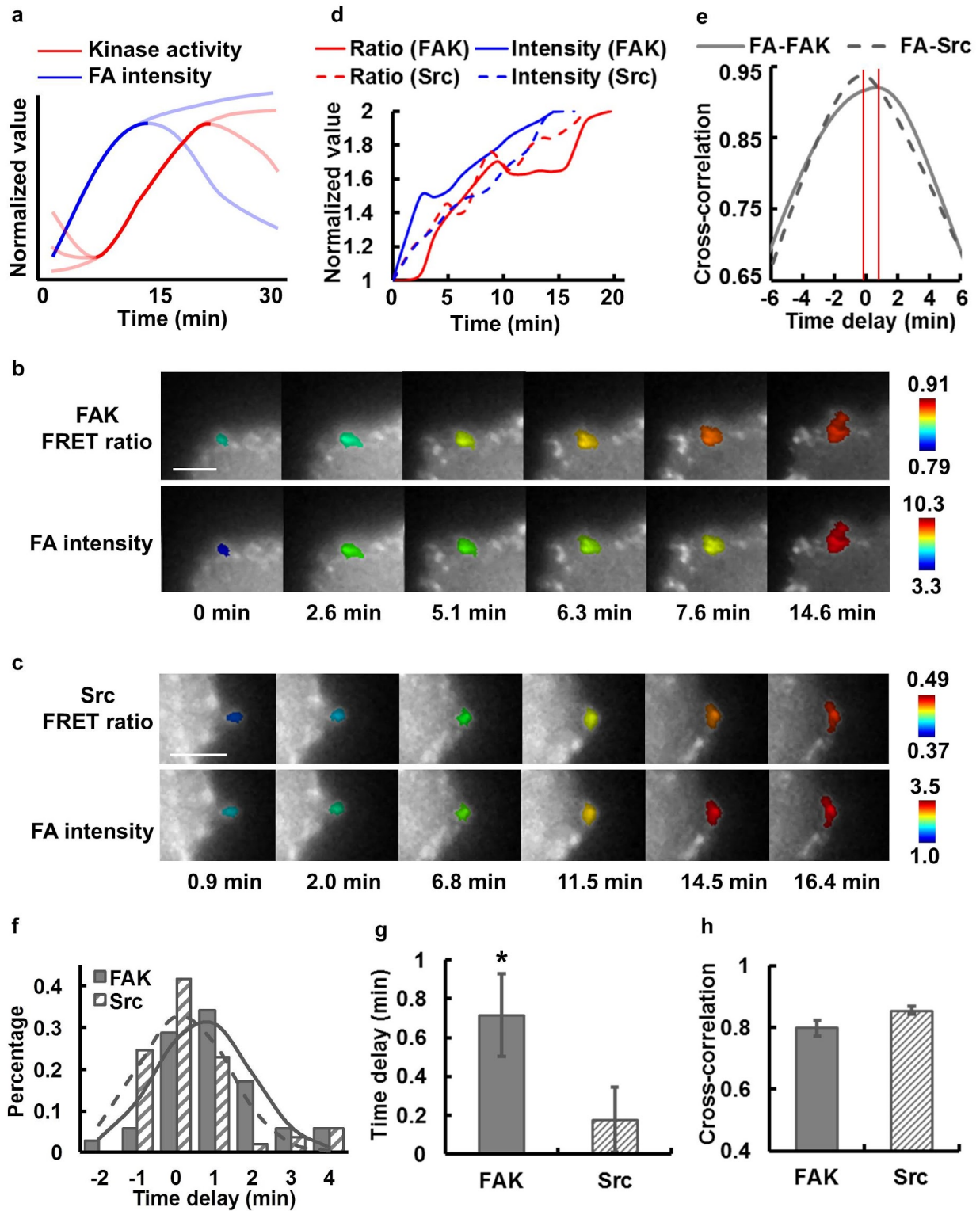
**Figure 2.5. FAK activation leads Src activation and FA turnover sequentially. (a)** The histograms of the single-FA time delays between the rising YPet intensity and ECFP/FRET ratio in different FA groups with the FAT-FAK biosensor or FAT-Src biosensor (insert). * indicates significant difference of the mean time delays between the matured and disassembled groups ($p < 0.05$). **(b)** YPet intensity images of a cell before and after FAK inhibitor PF228 treatment, with a representative FA color-coded by its FAT-FAK ECFP/FRET ratio (top) or the total FA YPet intensity (bottom). **(c)** The portions of the YPet intensity rising phase in the periods before ($34\pm9\%$) and after ($70\pm13\%$) PF228 treatment in FAs (* indicates significant difference, $p < 0.05$; number of FAs: $n = 10$; number of cells: $N = 1$). **(d)** The schematic of the typical kinase activity and total FA intensity kinetics at an individual FA highlighting the FA disassembly phase (solid blue) and its associated kinase activation phase (solid red). The time delay, Δt, is defined as the difference between the starting points of FA disassembly (solid blue curve) and its associated kinase activation phase (the immediate preceding local minimum in ECFP/FRET ratio). The lines in light colors illustrate the variations in ECFP/FRET ratio and YPet intensity trends among individual FAs. **(e)** The time courses of the ECFP/FRET ratio and YPet intensity in two representative FAs, each in cells with FAT-FAK (solid) or FAT-Src (dashed) biosensors. YPet intensity images of cells with the representative FAs in panel (e) color-coded by the ECFP/FRET ratio (top) or the total FA YPet intensity (bottom) in cells with either **(f)** FAT-FAK or **(g)** FAT-Src biosensors. **(h)** Compare the time delay, Δt (4.5 ± 0.5 min and 2.5 ± 0.3 min, respectively), calculated at individual FAs as described in (d) *: statistically significant difference by Kolmogorov-Smirnov test ($p < 0.05$, $n1=30$ in 6 cells, $n2 = 20$ in 10 cells). **(i)** The fitted Poisson distribution of FAT-FAK Δt (mean: $\lambda = 3.66$ min) and that of FAT-Src Δt (mean: $\lambda = 1.33$ min). Error bar: SEM. Scale bar: 5 μm.

41
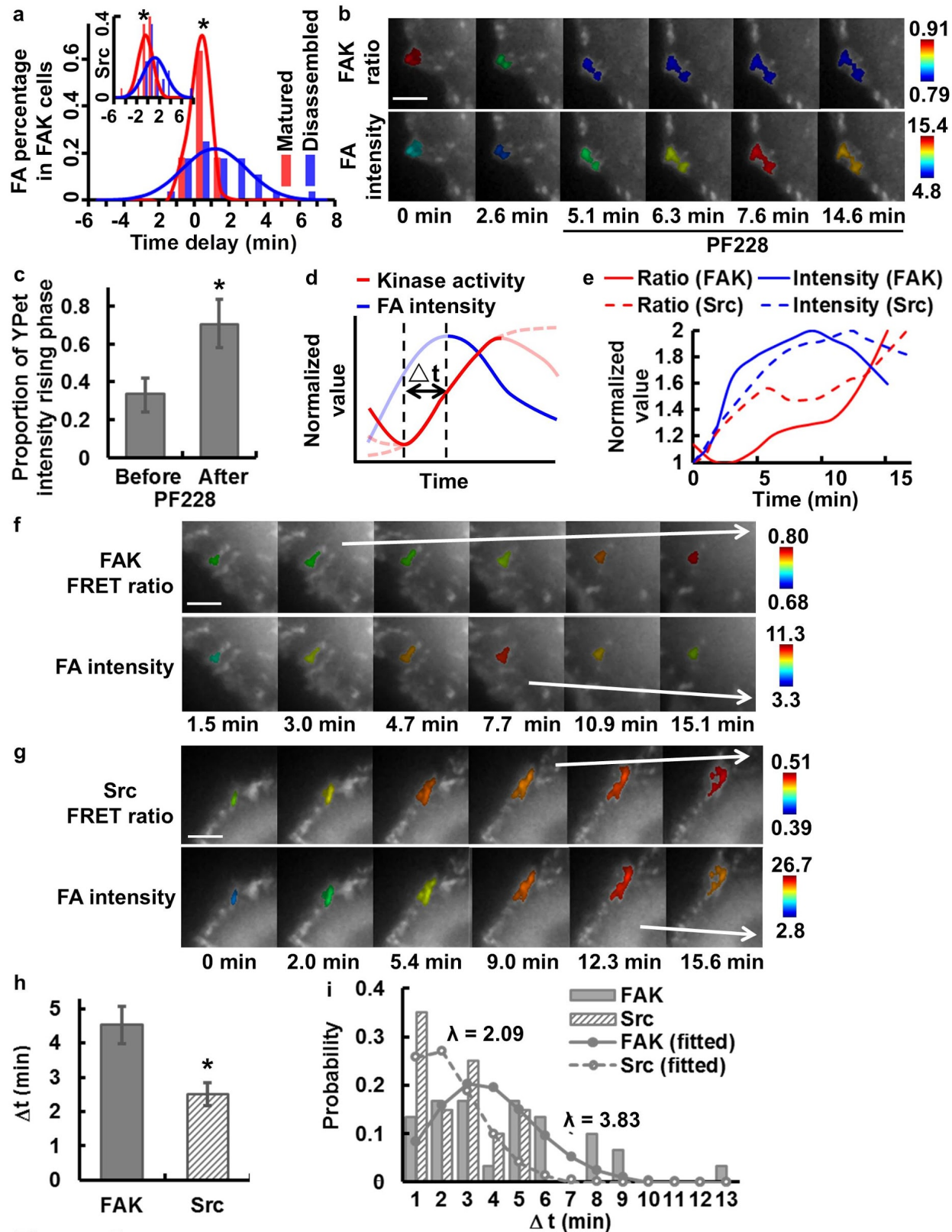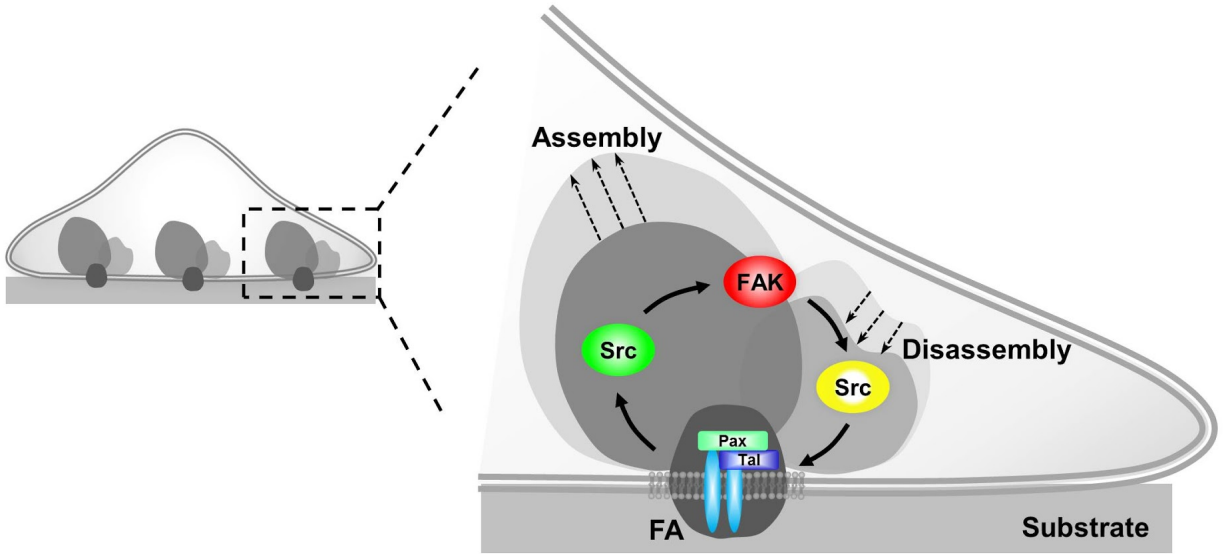
Figure 2.6. The proposed sequential signaling network of FAK and Src activations relative to the assembly and turnover of FAs at the single-FA level. During FA assembly, Src is activated earlier than FAK, while FAK activation in turn leads Src activation to trigger FA disassembly.
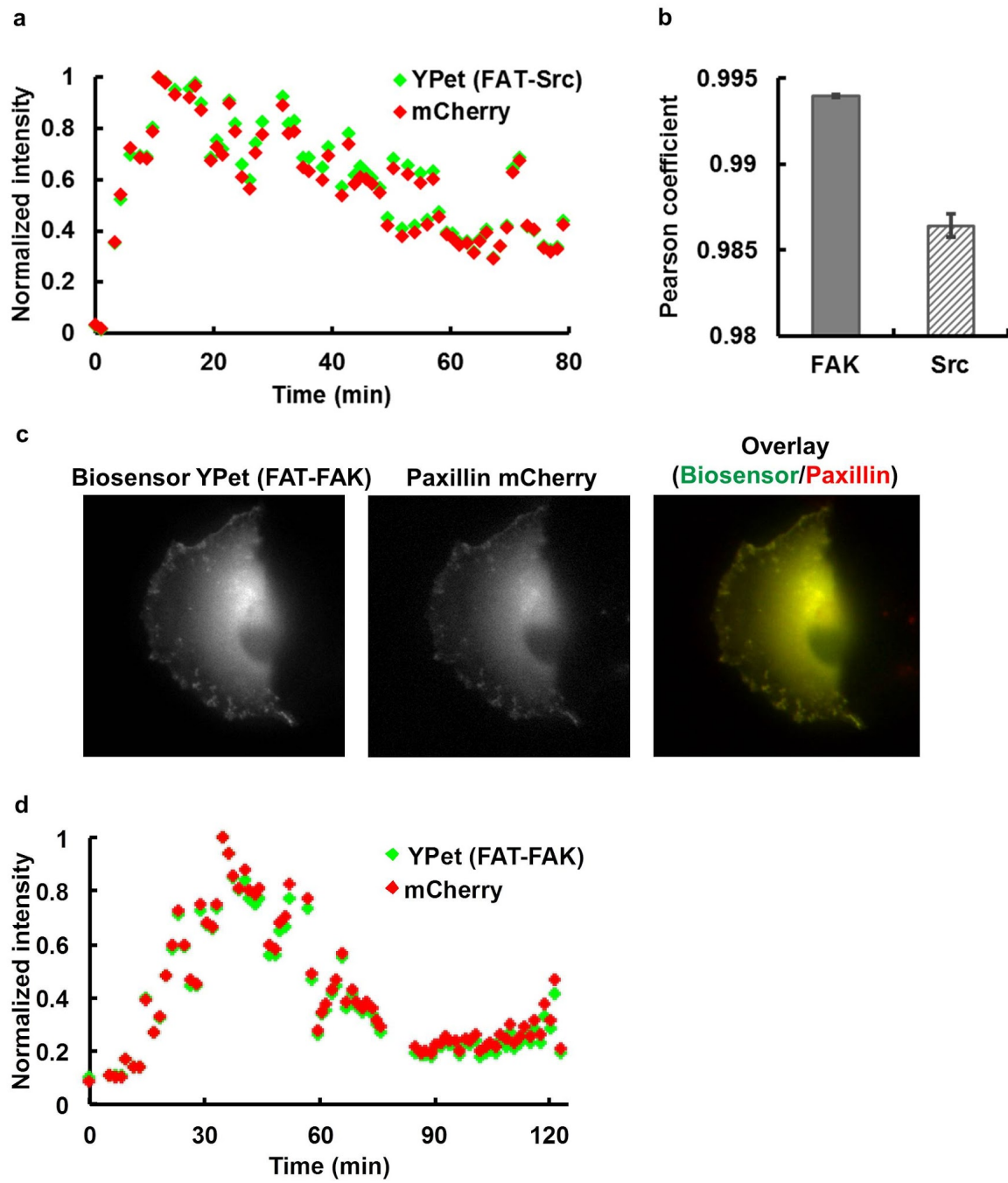
Figure 2.S1. The co-localization between FAT biosensors and paxillin. (a) The intensity time courses of the YPet channel of the FAT-Src biosensor and mCherry-paxillin at the FA sties of the cell shown in Fig.1b. **(b)** The Pearson coefficients evaluating the co-localization between FAT biosensors and paxillin images of the cells in Figs. 1b (Src) and 2b (FAK). **(c)** The YPet intensity image of the FAT-FAK biosensor (left) is compared with the intensity image of paxillin-mCherry (middle) to generate the overlaid image (right) in one cell. **(d)** The intensity time course of the YPet channel of the FAT-FAK biosensor and mCherry-paxillin at the FA sites of the cell shown in (c).

Figure 2.S2. The characterization of the FAT biosensors in MEFs. (a) The ECFP/FRET ratio images of a representative MEF transfected with the FAT-Src biosensor during adhesion. **(b)** The ECFP/FRET ratio images of a representative MEF transfected with the FAT-FAK biosensor during adhesion. **(c)** The time courses of the ECFP/FRET ratio in the cell shown in (a) (black line with circles) and that in (b) (gray line with triangles). **(d)** The average ECFP/FRET ratio values before (0-3 min, 0.61 ± 0.048, white) and after (57-60 min, 0.81 ± 0.047, gray) the appearance of FAs in cells with the FAT-FAK biosensor (*p = 0.04, n = 3*), and those before (0-3 min, 0.40 ± 0.023, white) and after (57-60 min, 0.54 ± 0.039, gray) the appearance of FAs in cells with the FAT-Src biosensor (*p = 0.03, n = 4*). * indicates statistically significant difference. Scale bar: 10 μm.
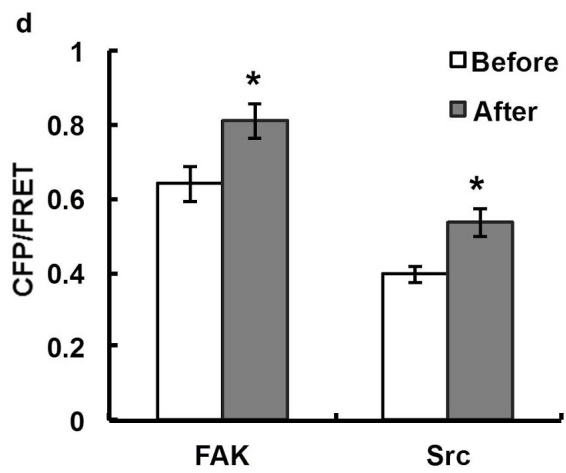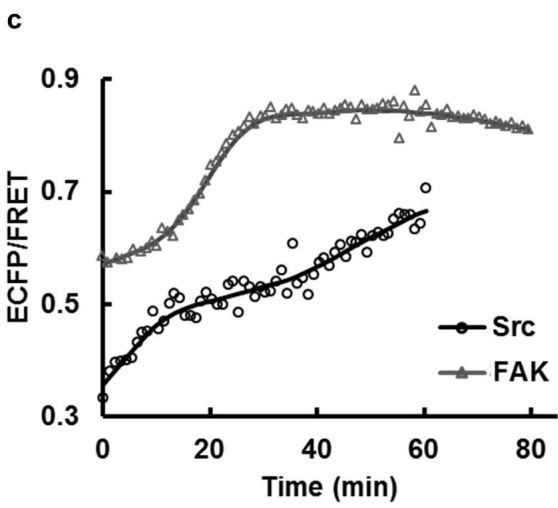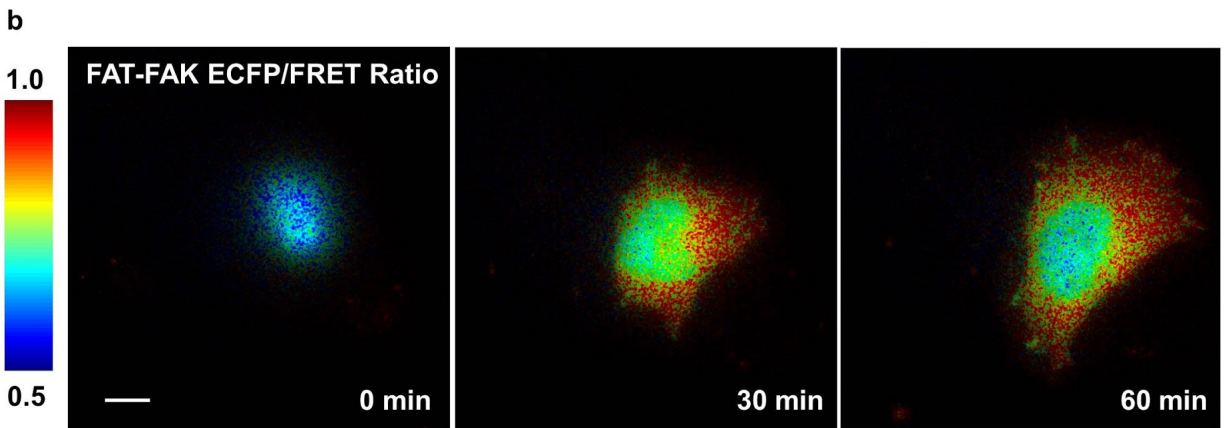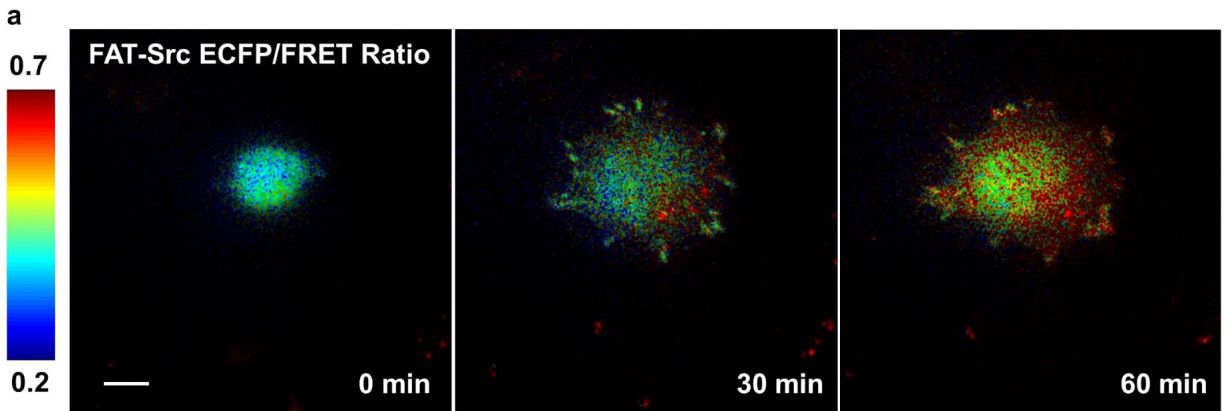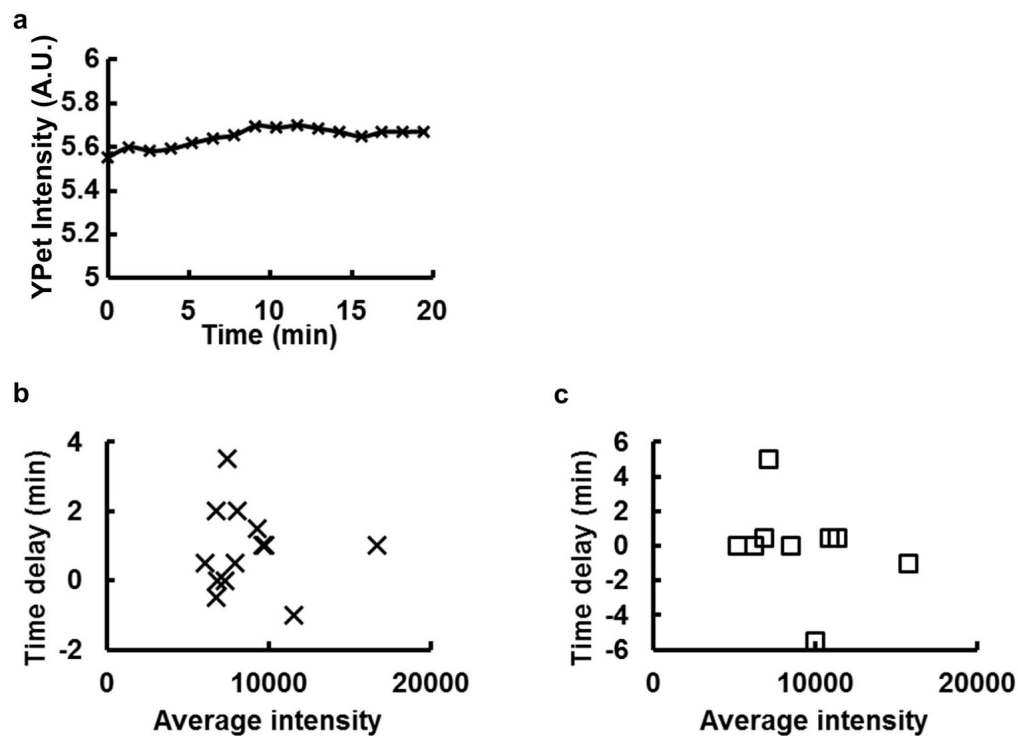
Figure 2.S3. The effects of photobleaching and biosensor targeting. (a) The time course of average whole-cell YPet intensity in a stable adhering cell with the FAT-FAK biosensor. **(b)** The relationship between the temporal average biosensor YPet intensity and the cross-correlation time delay in the assembly phase of single FAs in a representative cell with FAT-FAK biosensor ($R^2 = -0.006$; number of FAs: $n = 13$) and **(c)** that in a representative cell with FAT-Src biosensor ($R^2 = -0.09$; number of FAs: $n = 9$).

2.6. Supplemental video captions

Video 2.S1. The activation of Src kinase during cell adhesion and spreading.
The kinase activity of Src is visualized by the ECFP/FRET ratio of the transfected FAT-Src biosensor during the adhesion and spreading of the representative cell shown in Fig. 2.1b. The ECFP/FRET ratio turns from green to red, indicating an increase in Src activity.

Video 2.S2. The dynamic activity of Src kinase during the adhesion and spreading processes of a PP1-pretreated cell. The cell transfected with the FAT-Src biosensor and pretreated with PP1, corresponding to the one in Fig. 2.1c, develops fewer FAs with limited spreading and a lower ECFP/FRET ratio after touchdown as compared to the cell in Supplementary Video 2.S1.

Video 2.S3. The dynamic activity of FAK kinase during cell adhesion and spreading. The kinase activity of FAK is visualized by the ECFP/FRET ratio of the transfected FAT-FAK biosensor during the adhesion and spreading of the representative cell in Fig. 2.2b. The ECFP/FRET ratio turns from cool colors to warm colors as the cell spreads, and cools down after the addition of the FAK inhibitor PF228.

Video 2.S4. FAK activity and FA dynamics at a single FA during its assembly. Left: the YPet intensity images of the FAT-FAK biosensor were color-coded by the average FAK ECFP/FRET ratio within a representative FA at a corner of a cell. Right: the YPet intensity images were color-coded by the total YPet intensity within the same FA at the corner of the cell. A cold color indicates a low value while a hot color indicates a high one. This video corresponds to Fig. 2.4c.

Video 2.S5. Src activity and FA dynamics at a single FA during its assembly. Left: the YPet intensity images of the FAT-Src biosensor were color-coded by the average FAK ECFP/FRET ratio within a representative FA at a corner of a cell. Right: the YPet intensity images were color-coded by the total YPet intensity within the same FA at the corner of the cell. A cold color indicates a low value while a hot color indicates a high one. This video corresponds to Fig. 2.4d.

Video 2.S6. FAK activity and FA dynamics at a single FA before and after PF228 treatment. Left: the average ECFP/FRET ratio of the FAT-FAK biosensor (color-coded) superimposed on the YPet intensity images of the biosensors within a representative FA in part of a cell. Right: the total YPet intensity (color-coded) superimposed on the YPet intensity images of a representative FA in part of a cell. A cold color indicates a low value while a hot color indicates a high one. This video corresponds to Fig. 2.5a.

Video 2.S7. FAK activity and FA dynamics at a single FA over its lifespan. Left: the average ECFP/FRET ratio of the FAT-FAK biosensor (color-coded) superimposed on the YPet intensity images of the biosensors within a representative FA in part of a cell. Right: the total YPet intensity (color-coded) superimposed on the YPet intensity images of a representative FA in part

of a cell. A cold color indicates a low value while a hot color indicates a high one. This video corresponds to Fig. 2.5e.

Video 2.S8. Src activity and FA dynamics at a single FA over its lifespan. Left: the average ECFP/FRET ratio of the FAT-Src biosensor (color-coded) superimposed on the YPet intensity images of the biosensors within a representative FA in part of a cell. Right: the total YPet intensity (color-coded) superimposed on the YPet intensity images of a representative FA in part of a cell. A cold color indicates a low value while a hot color indicates a high one. This video corresponds to Fig. 2.5f.

2.7. References

1. Parsons, J. T., Horwitz, A. R., & Schwartz, M. A. (2010). Cell adhesion: integrating cytoskeletal dynamics and cellular tension. *Nat Rev Mol Cell Biol, 11*(9), 633-643. doi:10.1038/nrm2957

2. Zamir, E., Katz, B. Z., Aota, S., Yamada, K. M., Geiger, B., & Kam, Z. (1999). Molecular diversity of cell-matrix adhesions. *J Cell Sci, 112 (Pt 11)*, 1655-1669.

3. Oakes, P. W., & Gardel, M. L. (2014). Stressing the limits of focal adhesion mechanosensitivity. *Curr Opin Cell Biol, 30*, 68-73. doi:10.1016/j.ceb.2014.06.003

4. Webb, D. J., Parsons, J. T., & Horwitz, A. F. (2002). Adhesion assembly, disassembly and turnover in migrating cells -- over and over and over again. *Nat Cell Biol, 4*(4), E97-100. doi:10.1038/ncb0402-e97

5. Kanchanawong, P., Shtengel, G., Pasapera, A. M., Ramko, E. B., Davidson, M. W., Hess, H. F., & Waterman, C. M. (2010). Nanoscale architecture of integrin-based cell adhesions. *Nature, 468*(7323), 580-584. doi:10.1038/nature09621

6. Hu, K., Ji, L., Applegate, K. T., Danuser, G., & Waterman-Storer, C. M. (2007). Differential transmission of actin motion within focal adhesions. *Science, 315*(5808), 111-115. doi:10.1126/science.1135085

7. Vicente-Manzanares, M., Ma, X., Adelstein, R. S., & Horwitz, A. R. (2009). Non-muscle myosin II takes centre stage in cell adhesion and migration. *Nat Rev Mol Cell Biol, 10*(11), 778-790. doi:10.1038/nrm2786

8. Gardel, M. L., Schneider, I. C., Aratyn-Schaus, Y., & Waterman, C. M. (2010). Mechanical integration of actin and adhesion dynamics in cell migration. *Annu Rev Cell Dev Biol, 26*, 315-333. doi:10.1146/annurev.cellbio.011209.122036

9. Hynes, R. O. (2009). The extracellular matrix: not just pretty fibrils. *Science, 326*(5957), 1216-1219. doi:10.1126/science.1176009

10. Stehbens, S., & Wittmann, T. (2012). Targeting and transport: how microtubules control focal adhesion dynamics. *J Cell Biol, 198*(4), 481-489. doi:10.1083/jcb.201206050

11. Poh, Y. C., Shevtsov, S. P., Chowdhury, F., Wu, D. C., Na, S., Dundr, M., & Wang, N. (2012). Dynamic force-induced direct dissociation of protein complexes in a nuclear body in living cells. *Nat Commun, 3*, 866. doi:10.1038/ncomms1873

12. Wolfenson, H., Iskratsch, T., & Sheetz, M. P. (2014). Early events in cell spreading as a model for quantitative analysis of biomechanical events. *Biophys J, 107*(11), 2508-2514. doi:10.1016/j.bpj.2014.10.041

13. Giannone, G., Dubin-Thaler, B. J., Dobereiner, H. G., Kieffer, N., Bresnick, A. R., & Sheetz, M. P. (2004). Periodic lamellipodial contractions correlate with rearward actin waves. *Cell, 116*(3), 431-443. doi:10.1016/s0092-8674(04)00058-3

14. Shen, B., Delaney, M. K., & Du, X. (2012). Inside-out, outside-in, and inside-outside-in: G protein signaling in integrin-mediated cell adhesion, spreading, and retraction. *Curr Opin Cell Biol, 24*(5), 600-606. doi:10.1016/j.ceb.2012.08.011

15. Yu, C. H., Law, J. B., Suryana, M., Low, H. Y., & Sheetz, M. P. (2011). Early integrin binding to Arg-Gly-Asp peptide activates actin polymerization and contractile movement that stimulates outward translocation. *Proc Natl Acad Sci U S A, 108*(51), 20585-20590. doi:10.1073/pnas.1109485108

16. Oakes, P. W., Beckham, Y., Stricker, J., & Gardel, M. L. (2012). Tension is required but not sufficient for focal adhesion maturation without a stress fiber template. *J Cell Biol, 196*(3), 363-374. doi:10.1083/jcb.201107042

17. Webb, D. J., Donais, K., Whitmore, L. A., Thomas, S. M., Turner, C. E., Parsons, J. T., & Horwitz, A. F. (2004). FAK-Src signalling through paxillin, ERK and MLCK regulates adhesion disassembly. *Nat Cell Biol, 6*(2), 154-161. doi:10.1038/ncb1094

18. Lu, S., Seong, J., Wang, Y., Chang, S. C., Eichorst, J. P., Ouyang, M., . . . Wang, Y. (2014). Decipher the dynamic coordination between enzymatic activity and structural modulation at focal adhesions in living cells. *Sci Rep, 4*, 5756. doi:10.1038/srep05756

19. Plotnikov, S. V., Pasapera, A. M., Sabass, B., & Waterman, C. M. (2012). Force fluctuations within focal adhesions mediate ECM-rigidity sensing to guide directed cell migration. *Cell, 151*(7), 1513-1527. doi:10.1016/j.cell.2012.11.034

20. Iskratsch, T., Wolfenson, H., & Sheetz, M. P. (2014). Appreciating force and shape-the rise of mechanotransduction in cell biology. *Nat Rev Mol Cell Biol, 15*(12), 825-833. doi:10.1038/nrm3903

21. Zhang, X., Jiang, G., Cai, Y., Monkley, S. J., Critchley, D. R., & Sheetz, M. P. (2008). Talin depletion reveals independence of initial cell spreading from integrin activation and traction. *Nat Cell Biol, 10*(9), 1062-1068. doi:10.1038/ncb1765

22. Zhang, J., Campbell, R. E., Ting, A. Y., & Tsien, R. Y. (2002). Creating new fluorescent probes for cell biology. *Nat Rev Mol Cell Biol, 3*(12), 906-918.

23. Wang, Y., Shyy, J. Y., & Chien, S. (2008). Fluorescence proteins, live-cell imaging, and mechanobiology: seeing is believing. *Annu Rev Biomed Eng, 10*, 1-38.

24. Wang, Y., Botvinick, E. L., Zhao, Y., Berns, M. W., Usami, S., Tsien, R. Y., & Chien, S. (2005). Visualizing the mechanical activation of Src. *Nature, 434*(7036), 1040-1045. doi:10.1038/nature03469

25. Seong, J., Ouyang, M., Kim, T., Sun, J., Wen, P. C., Lu, S., . . . Wang, Y. (2011). Detection of focal adhesion kinase activation at membrane microdomains by fluorescence resonance energy transfer. *Nat Commun, 2*, 406. doi:10.1038/ncomms1414

26. Seong, J., Lu, S., Ouyang, M., Huang, H., Zhang, J., Frame, M. C., & Wang, Y. (2009). Visualization of Src activity at different compartments of the plasma membrane by FRET imaging. *Chem Biol, 16*(1), 48-57.

27. Tachibana, K., Sato, T., D'Avirro, N., & Morimoto, C. (1995). Direct association of pp125FAK with paxillin, the focal adhesion-targeting mechanism of pp125FAK. *J Exp Med, 182*(4), 1089-1099. doi:10.1084/jem.182.4.1089

28. Zheng, C., Xing, Z., Bian, Z. C., Guo, C., Akbay, A., Warner, L., & Guan, J. L. (1998). Differential regulation of Pyk2 and focal adhesion kinase (FAK). The C-terminal domain of FAK confers response to cell adhesion. *J Biol Chem, 273*(4), 2384-2389. doi:10.1074/jbc.273.4.2384

29. Schlaepfer, D. D., & Mitra, S. K. (2004). Multiple connections link FAK to cell motility and invasion. *Curr Opin Genet Dev, 14*(1), 92-101. doi:10.1016/j.gde.2003.12.002

30. Hayashi, I., Vuori, K., & Liddington, R. C. (2002). The focal adhesion targeting (FAT) region of focal adhesion kinase is a four-helix bundle that binds paxillin. *Nat Struct Biol, 9*(2), 101-106. doi:10.1038/nsb755

31. Eliceiri, K. W., Berthold, M. R., Goldberg, I. G., Ibanez, L., Manjunath, B. S., Martone, M. E., . . . Carpenter, A. E. (2012). Biological imaging software tools. *Nat Methods, 9*(7), 697-710. doi:10.1038/nmeth.2084

32. Zhuo, Y., Qian, T., Wu, Y., Seong, J., Gong, Y., Ma, H., . . . Lu, S. (2015). Subcellular and Dynamic Coordination between Src Activity and Cell Protrusion in Microenvironment. *Sci Rep, 5*, 12963. doi:10.1038/srep12963

33. Ouyang, M., Sun, J., Chien, S., & Wang, Y. (2008). Determination of hierarchical relationship of Src and Rac at subcellular locations with FRET biosensors. *Proc Natl Acad Sci U S A, 105*(38), 14353-14358.

34. Seong, J., Tajik, A., Sun, J., Guan, J. L., Humphries, M. J., Craig, S. E., . . . Wang, Y. (2013). Distinct biophysical mechanisms of focal adhesion kinase mechanoactivation by different extracellular matrix proteins. *Proc Natl Acad Sci U S A, 110*(48), 19372-19377. doi:10.1073/pnas.1307405110

35. Ouyang, M., Lu, S., Li, X. Y., Xu, J., Seong, J., Giepmans, B. N., . . . Wang, Y. (2008). Visualization of polarized membrane type 1 matrix metalloproteinase activity in live cells by fluorescence resonance energy transfer imaging. *J Biol Chem, 283*(25), 17740-17748. doi:10.1074/jbc.M709872200

36. Turner, C. E. (1998). Paxillin. *Int J Biochem Cell Biol, 30*(9), 955-959. doi:10.1016/s1357-2725(98)00062-4

37. Turner, C. E. (2000). Paxillin and focal adhesion signalling. *Nat Cell Biol, 2*(12), E231-236. doi:10.1038/35046659

38. Jaqaman, K., Loerke, D., Mettlen, M., Kuwata, H., Grinstein, S., Schmid, S. L., & Danuser, G. (2008). Robust single-particle tracking in live-cell time-lapse sequences. *Nat Methods, 5*(8), 695-702. doi:10.1038/nmeth.1237

39. Ruest, P. J., Roy, S., Shi, E., Mernaugh, R. L., & Hanks, S. K. (2000). Phospospecific antibodies reveal focal adhesion kinase activation loop phosphorylation in nascent and mature focal adhesions and requirement for the autophosphorylation site. *Cell Growth Differ, 11*(1), 41-48.

40. Guan, J. L. (1997a). Role of focal adhesion kinase in integrin signaling. *Int J Biochem Cell Biol, 29*(8-9), 1085-1096. doi:10.1016/s1357-2725(97)00051-4

41. Iskratsch, T., Yu, C. H., Mathur, A., Liu, S., Stevenin, V., Dwyer, J., . . . Sheetz, M. (2013). FHOD1 is needed for directed forces and adhesion maturation during cell spreading and migration. *Dev Cell, 27*(5), 545-559. doi:10.1016/j.devcel.2013.11.003

42. Ghassemi, S., Meacci, G., Liu, S., Gondarenko, A. A., Mathur, A., Roca-Cusachs, P., . . . Hone, J. (2012). Cells test substrate rigidity by local contractions on submicrometer pillars. *Proc Natl Acad Sci U S A, 109*(14), 5328-5333. doi:10.1073/pnas.1119886109

43. Ezzell, R. M., Goldmann, W. H., Wang, N., Parashurama, N., & Ingber, D. E. (1997). Vinculin promotes cell spreading by mechanically coupling integrins to the cytoskeleton. *Exp Cell Res, 231*(1), 14-26. doi:10.1006/excr.1996.3451

44. Basson, M. D. (2008). An intracellular signal pathway that regulates cancer cell adhesion in response to extracellular forces. *Cancer Res, 68*(1), 2-4. doi:10.1158/0008-5472.CAN-07-2992

45. Guan, J. L. (1997b). Focal adhesion kinase in integrin signaling. *Matrix Biol, 16*(4), 195-200. doi:10.1016/s0945-053x(97)90008-1

46. Mitra, S. K., & Schlaepfer, D. D. (2006). Integrin-regulated FAK-Src signaling in normal and cancer cells. *Curr Opin Cell Biol, 18*(5), 516-523. doi:10.1016/j.ceb.2006.08.011

47. Brunton, V. G., & Frame, M. C. (2008). Src and focal adhesion kinase as therapeutic targets in cancer. *Curr Opin Pharmacol, 8*(4), 427-432. doi:10.1016/j.coph.2008.06.012

48. Lu, S., Ouyang, M., Seong, J., Zhang, J., Chien, S., & Wang, Y. (2008). The spatiotemporal pattern of Src activation at lipid rafts revealed by diffusion-corrected FRET imaging. *PLoS Comput Biol, 4*(7), e1000127. doi:10.1371/journal.pcbi.1000127

CHAPTER 3. MRI-guided FUS system

3.1. Introduction

As discussed in Chapter 1, ultrasonic waves generated by FUS can heat tissues through mechanisms involving internal friction. While FUS-induced high temperature (>65°C) leads to the destruction of tissues, a clinical treatment for certain diseases, mild hyperthermia induced by FUS at or below 43°C has been used to regulate gene expression through heat-sensitive genetic circuits. Meanwhile, FUS is integrated with MRI as the latter can provide accurate and real-time monitoring of the temperature in animals and humans. MRI-guided FUS systems are therefore widely used in clinics. As MRI-guided FUS heating is non-ionizing, noninvasive, and can reach deep tissues in living organisms, it is an excellent tool for the remote perturbation and control of genetic and cellular functions. Despite earlier work utilizing this technology for the induction of reporter gene expression, few groups have applied it for functional studies with therapeutic purposes.

We believe that there is more to the potential of the FUS-based acoustogenetics technology - its clinical compatibility and deep penetration should make it a great tool for translational research. We therefore sought to apply this technology to achieve remote controllable immunotherapy, which will be covered in detail in Chapter 4. This chapter focuses on the methods and protocols for the MRI-guided FUS system.

3.2. Methods and protocols

We acquired an MRI-guided FUS system from Image Guided Therapy (Pessac, France). The system is composed of an 8-element annular array transducer (bandwidth = 1.4 - 1.5 MHz, diameter = 2.5 cm, radius of curvature = 2.0 cm), a 16-channel broadband RF generator (4 W per

channel), a piezo motor based X-Y positioning stage, degassing system, FUS workstation (ThermoGuide software), a customized Tx/Rx MRI coil for small animal imaging, and anesthesia cone and other accessories. The FUS system was integrated with the 7T MRI scanner (Bruker) at the Center for Functional MRI (CFMRI).

The operation of the MRI-guided FUS system follows three steps in general: I. Experimental setup; II. Transducer focus localization; III. FUS stimulation.

3.2.1. Experimental setup

1. Hardware setup. The inlet and outlet tubes on the transducer case are connected to the degassing system to allow water circulation and degassing. Once connected, the transducer case is filled with water and the membrane is inflated. Air is completely removed from the transducer case by water flow and the degassing system to ensure ultrasound propagation.

2. Software setup. The Paravision 5.1 software is used to acquire and transfer MRI images. The ThermoGuide software is used to control the FUS system. The vital signs of the animal during FUS stimulation are monitored using a physiological monitoring software.

3. Animal setup. Laboratory mice are shaved prior to arrival at the CFMRI. Anesthesia induction is typically conducted with 2% isoflurane-oxygen mixture. Once anesthetized, the mouse is placed on the FUS insert, with anesthesia maintained with 1.5% isoflurane-oxygen through a nose cone. Pressure pad and rectal probe are then set up to monitor its respiration rate and body temperature. A heater supplies warm air into the MRI bore to maintain the body temperature at 37°C through a feedback system. The transducer is placed above the target region, with the membrane touching the skin through thin layers of ultrasound gel.

3.2.2. Transducer focus localization

1. Transducer localization. TriPilot, coronal, and axial MRI scans are performed, and the images are transferred to ThermoGuide. The location of the transducer is determined through interactive computing, and a 3D representation of the transducer is generated in ThermoGuide.

2. Focus localization. Test shots are performed to localize the true focus, which could differ slightly from the geometric focus calculated based on the 3D representation of the transducer generated in the previous step. The test shots increase the temperature of the focal area, and the pixel (voxel) with the highest temperature increase is manually selected to set as focus.

3.2.3. FUS stimulation

1. Targeted heating. ThermoGuide allows automatic regulation of the ROI (region of interest) temperature through PID controller. In the automatic regulation script, a point ROI is chosen to be the regulation target. Empirically determined absorption and diffusion coefficients of the tissue, and the desired temperature and duration are manually input. During regulation, ThermoGuide calculates the phase images from the acquired and transferred MR images to generate real-time temperature maps of the scanning object. The temperature of the 9-pixel square centered at the point ROI feeds back to the PID controller to regulate the output power of the generator. As a result, the ROI temperature is increased to and maintained at the desired value.

2. Z-steering (optional). The 8-element annular array transducer allows adjustment of the focal depth in the Z direction (Z-steering). In the current subcutaneous tumor mouse model, the natural focus of the transducer usually falls on the skin/tumor, which allows FUS stimulation

without the need of Z-steering. However, in cases where the FUS stimulation target is deep in the tissue/phantom, Z-steering can be applied to focus the ultrasound beam to the intended position.

3.2.4. Operation protocol

A detailed protocol is summarized below.

I. Experimental setup

1. Hardware setup.

1) Connect the laptop and the generator, the laptop and the MRI computer using established wires.

2) Turn on the generator.

3) Connect the transducer case to the water circulation system through the inlet and outlet tubes.

4) Press the water circulation button and open the valves to start circulation.

5) Hold the transducer case and adjust its position while water fills up to avoid overinflation of the membrane.

6) Remove large air bubbles inside the transducer case by holding it with the inlet tube on the bottom and outlet tube on the top. Gently tap the case to let the air bubbles exit through the outlet.

7) Press the degassing button and leave it on for 10 min to dissolve small bubbles.

8) Prepare agarose gel as cushion for ultrasound exit.

9) Connect the transducer to the generator through the wire.

10) Set the FUS insert on the MR patient table.

11) Attach heater tubes and anesthesia tubes to the FUS insert.

2. Software setup.

   1) Open the ThermoGuide software.

   2) Trajectory Planner → Connect and Initialize.

   3) Open Paravision 5.1.

   4) Turn on the vital sign monitoring software. Set the heater feedback temperature to 37°C.

3. Animal setup.

   1) Induce anesthesia in the shaved mouse with 2% isoflurane-oxygen mixture and maintain at 1.5% or adjust according to its vital signs.

   2) Place the anesthetized mouse above the agarose gel cushion on the FUS insert and supply isoflurane-oxygen mixture through the nose cone.

   3) Set up the pressure pad and rectal probe to monitor the mouse's respiration rate and body temperature.

   4) Turn on the heater.

   5) Apply thin layers of ultrasound gel on the target region of the mouse and the transducer membrane.

   6) Place the transducer on the target region (usually the tumor region identified by IVIS), with the membrane touching the skin. Adjust the curvature of the membrane via the syringe. Adjust transducer position in ThermoGuide if needed.

   7) Place the FUS insert (with the mouse) into the MR bore.

II. Transducer focus localization

1. Transducer localization.

1) Paravision → Run the TriPilot scan to localize the transducer

2) Paravision → Run coronal and axial scans

3) Transfer scan data from Paravision to ThermoGuide, and load the coronal and axial images of the transducer: ThermoGuide → View → Targeting → Load Dicom sequences

4) Trajectory Planner → Locate. Draw three points based on the coronal images to generate a 3D representation of the transducer. Adjust its 3D location on coronal and axial images to fit the acquired images.

2. Focus localization.

1) ThermoGuide → View → ThermoGuide → Open Script → SNR_relTemp_TDose.

2) In ThermoGuide → Trajectory Planner → Electronic trajectory, set Time per shot = 1000 ms, Amplitude = 25%. In Execution, set Execution(s) = 10, click Send. Connect with MRI console.

3) In Paravision, open scan "igt_temp". Set the Z position of the middle slice the same as that of the geometric focus. Set repetition number = 15. ACQP → add users filter to pipeline: yes; users filter program name: igt.

4) Start acquisition: Paravision → GOP.

5) In ThermoGuide, click "Execute" after five dynamics to start FUS stimulation.

6) After the scan is completed, return to the dynamic with the largest temperature increase, and mark the pixel (voxel) with the highest temperature using the Point ROI tool in ThermoGuide. Set this point as the new focus: Trajectory Planner → Adjust… → select the drawn point ROI.

7) If the focus is not where FUS stimulation should be targeted, adjust the physical position of the transducer in X-Y plane so that the transducer is focused at the intended region: Trajectory Planner → Relative displacement. Refer to section III - 2 Z-steering if the position of the focus needs adjusting in the Z direction.

III. FUS stimulation.

1. Targeted heating.

1) ThermoGuide → View → ThermoGuide → Open Script → SNR_Temp_RetroControlOnROI.

2) Draw a point ROI (usually at the focus) and set as the ROI for temperature regulation. Draw polygonal ROIs and set as seed (reference) and unwrap (temperature calculation and display) regions.

3) Set the following parameters: deltaT (tolerance) = 5 - 10, absorptionCoeff = 0.4, diffusionCoeff = 0.01, convKernel = 1 or 2. Connect with MRI console.

4) In the wantedTemp CSV file, set the desired temperature and duration. For example (assuming each dynamic/repetition takes ~2.8 sec):

1;0 // initial condition

10;8 // increase temperature by 8°C in 9 repetitions

120;8 // maintain the temperature at 8°C above the initial reference for 110 repetitions (~3 min)

5) In Paravision, open scan "igt_temp". Set the Z position of the middle slice the same as that of the point ROI. Set repetition number to match the desired duration. ACQP → add users filter to pipeline: yes; users filter program name: igt.

6) In ThermoGuide → Trajectory Planner → Electronic trajectory, set Time per shot 300 ms shorter than the duration of one dynamic (one repetition) shown in Paravision.

7) Start acquisition: Paravision → GOP.

2. Z-steering (optional).

1) ThermoGuide → Trajectory Planner → Electronic trajectory → Zt[mm] = Z_{target}.

2) In Paravision, open scan "igt_temp". Set Z_{target} as the Z position of the middle slice. Perform targeted heating as described above.

CHAPTER 4. ACOUSTOGENETIC CONTROL OF CAR T CELLS VIA FOCUSED ULTRASOUND

4.1. Introduction

Chimeric antigen receptor (CAR) T cell therapy, where T cells are genetically programmed with redirected specificity against malignant cells, is becoming a paradigm-shifting approach for cancer treatment, especially for blood cancers (*1*). However, major challenges remain for solid tumors before CAR-based immunotherapy can be widely adopted. For instance, the non-specific targeting of the CAR T cells against normal tissues (on-target off-tumor toxicities) can be life-threatening: off-tumor toxicities against the lung, the brain, and the heart have caused multiple cases of deaths (*1-4*). Immunosuppressive corticosteroid therapy and suicide gene engineering are relatively effective in suppressing off-tumor toxicities and related cytokine release syndrome (CRS), but they fail to discriminate between beneficial T cell functions and toxic side effects (*5-7*). Synthetic biology and genetic circuits have been used to enhance specificity and reduce off-tumor toxicity by creating chemically inducible dimerization of split CARs, inhibitory CARs (iCARs), and SynNotch to control CAR activation (*2, 8-12*). However, given the extensive overlaps of antigens between solid tumors and normal tissues, especially those under conditions of tissue injury/inflammation (*13*), it remains very difficult to identify ideal antigens and their combinations to differentiate tumors from normal tissues. There is hence an urgent need for a high-precision control of CAR-T cells to confine the activation at local sites of solid tumors.

Optogenetics enables the control of specific molecular events and cellular functions in living systems with high spatiotemporal resolutions. However, optogenetics cannot reach deep tissues, with its penetration depth typically limited at micrometer scales (*14*). Ultrasound can be

focused to deliver mechanical energy safely and noninvasively into small volumes of tissue deep inside the body up to tens of centimeters (*14*). The rapidly oscillating pressure of focused ultrasound (FUS) waves and the resultant cycles of mechanical loading/unloading can lead to local heat generation in biological tissues. Aided by Magnetic Resonance Imaging (MRI) thermometry, FUS has been widely applied to clinically ablate tumors, and control drug delivery, vasodilation, neuromodulation (*15*), and transgene expression *in vitro* and *in vivo* using the heat-shock-protein promoter (Hsp) (*16-18*). Transcription factors and genetic circuits have also been engineered to convert the FUS-generated heat into genetic regulation to control microbial systems *in vivo* (*19*). However, there is a lack of general methods using FUS to control mammalian cell functions *in vivo* for therapeutic applications. Recently, we demonstrated that ultrasound signals can be amplified by microbubbles coupled to cells engineered with the mechanosensor Piezo1 to genetically control CAR T cell functions (*20*). However, the presence of microbubbles as cofactors limits the application of this system *in vivo*. Here, we have engineered a new class of inducible CAR T cells that can be remotely controlled by FUS without any co-factor. We show that short-pulsed FUS stimulation can activate the engineered T cells at the desired time and location to suppress tumor growth *in vivo*.

4.2. Results

4.2.1. Heat-induced reporter gene activation

We have engineered T cells with inducible CAR cassettes that can be activated by heat at 43°C. MRI-guided FUS is targeted at the tumor site to elevate the local temperature to 43°C through automated control for a desired period of time, activating the engineered T cells at local

sites to express CAR for recognizing, engaging, and eradicating the target tumor cells (Fig. 4.1A).

We first tested the inducible activation of a reporter eGFP under the control of the Hsp. We assembled a dual-promoter reporter construct containing the Hsp-driven eGFP and a constitutive PGK-driven mCherry (Fig. 4.1B). HEK 293T cells infected with the reporter lentivirus (fig. 4.S1A) were heated at 43°C for 15 min. Real-time fluorescence imaging revealed that the heat-induced eGFP expression started as early as 2 hr after heat shock (HS) and persisted throughout the course of observation (Fig. 4.1C and Video 4.S1). Quantitative tracking of the dynamics of heat-induced eGFP expression by flow cytometry showed that 97% of the cells expressed eGFP at 6 hr post HS, and the percentage increased to 99% at 12 hr and remained stable for 2 days, while the mean fluorescence intensity peaked at 12 hr followed by a steady decrease (Fig. 4.1D). We then investigated the inducible effect of HS in primary human T cells hosting the dual-promoter eGFP reporter (fig. 4.S1B). A 15-min HS induced a strong eGFP expression in 92.9% of the engineered T cells, in contrast to a background of 3.9% in control cells without HS (Fig. 4.1, E and F). The mean fluorescence intensity of the eGFP+ cells in the HS group was 10-fold of that in the control group without HS (Fig. 4.1G).

4.2.2. Heat-induced CAR expression and its functionality in Jurkat and primary human T cells

In order to convert the transient heat stimulation to a sustained gene activation and cellular functions for therapeutic actions, we integrated the Cre-lox gene switch into the inducible system. The design is composed of two constructs, one containing the Hsp-driven Cre recombinase and the PGK-driven membrane c-Myc tag for cell sorting ("inducible Cre", Fig. 4.2A), and the other containing a lox-flanked "ZsGreen-STOP" sequence between a PGK promoter and an anti-CD19 CAR ("lox-stop CAR reporter", Fig. 4.2A). As such, the excision of

the "STOP" cassette mediated by the transient heat-induced Cre can cause a switch from ZsGreen to sustained CD19CAR production.

We first tested this heat-inducible gene switch system in Jurkat T cell lines (fig. 4.S2A). A 15-min HS induced CAR expression in 76.6% of the cells when measured 24 hr after HS (Day 1), in contrast to a basal value of 14.0% in control cells without HS and a minimal leakage of 0.6% in cells infected with the lox-stop CAR reporter alone (Fig. 4.2B). The heat-induced CAR expression remained stable when measured 6 days after HS (Day 6, Fig. 4.2B). We further examined the functionality of the induced CD19CAR in engineered cells (Fig. 4.2C). Engineered Jurkat cells with (HS) or without (CT, control) a 15-min HS were co-cultured with CD19-expressing Nalm-6 tumor cells for 24 hr. Quantification of the expression level of CD69 (an early T cell activation marker) revealed a 73.4% CD69+ cell population in the engineered Jurkat cells in the HS group, in contrast to a 11.9% in the control group (Fig. 4.3, D and E). These results indicate that the HS-induced CD19CAR is efficient for functional changes in engineered Jurkat T cells.

We then examined our system in primary human T cells (Fig. 4.2, A and C; fig. 4.S2B). CAR antibody staining showed that a 15-min HS induced CAR expression in 29% of the T cells, in contrast to 1.9% in control cells without HS (Fig. 4.2F). The heat-inducible CAR T cells were then co-cultured with firefly luciferase (Fluc)-expressing Nalm-6 cells at different effector-to-target (E:T) ratios for cytotoxicity assays. The luminescence of the remaining Nalm-6 cells was quantified after 24-hr co-culture. The heat-stimulated T cells (HS) demonstrated increased cytotoxicity with increased E:T ratio, with the largest difference in cytotoxicity between the HS and control (CT) T cells observed at E:T = 1:5, eliminating 82.9% and 29.3% of the target tumor cells, respectively (Fig. 4.2G). The heat-stimulated CAR T cells also released significantly

higher concentrations of cytokines (IFN-γ and IL-2) than the control cells when co-cultured with Nalm-6 cells (Fig. 4.2, H and I), verifying the functional capability gained with the HS-induced CAR T cells.

While the continuous 15 min HS could lead to strong gene inductions (Figs. 4.1 and 4.2), it may cause toxicity to cells (*21*). We hence investigated the effect of different HS patterns in primary human T cells (fig. 4.S3). Our results showed that longer HS resulted in more cell death; however, pulsed HS was able to alleviate this toxicity while achieving induction levels comparable to that induced by continuous HS with the same total heating time (fig. 4.S3). In particular, a pulsed HS with 50% duty cycle and a total heating time of 15 min (fig. 4.S3A, Pattern 2) caused a strong induction of eGFP expression in 91.4% of the T cells engineered with the dual-promoter eGFP reporter, with a minimal toxicity as evidenced by the 92.2% cell viability measured 24 hr after HS (fig. 4.S3, B to E). Therefore, we applied this HS pattern (fig. 4.S3A, Pattern 2) for *in vivo* therapeutic studies.

4.2.3. MRI-guided FUS-induced gene activation in phantom and in vivo

MRI-guided FUS enables the delivery of thermal energy *in vivo* at confined local regions with high spatiotemporal resolutions (*16, 17*). We integrated an MRI-guided FUS system (Image Guided Therapy) with a 7T MRI as described in Methods. An annular array transducer is placed above the target region of the object to be heated (phantoms or small animals) in the MRI bore. MR images are acquired and transferred to Thermoguide software to calculate the temperature of the target region in real-time, which is fed back to the PID controller to automatically regulate the output power of the FUS generator, maintaining the temperature of the target region at the desired level (Fig. 4.3A).

We lentivirally introduced the dual-luciferase reporter with inducible Fluc and constitutive Rluc (Hsp-Fluc-PGK-Rluc-mCherry; Rluc, *Renilla* luciferase; Fig. 4.3B) into Nalm-6 cells and embedded them in a tofu phantom approximately 7 mm deep from the top surface (Fig. 4.3C and Methods). We then focused the ultrasound on the embedded cells by changing the focal distance in the z direction. Three pulses of 5-min FUS stimulations caused a significant induction of gene expression as quantified by the Fluc/Rluc ratio of the cells assayed 8 hr later (Fig. 4.3D, Methods). The induction level is comparable to that of the positive control using thermal cycler with the same heating pattern (Fig. 4.3D).

We then used MRI-guided FUS to control local temperature *in vivo* in mouse (Fig. 4.3, E and F) and tested the FUS-induced gene activation using Nalm-6 cells with the dual-luciferase reporter *in vivo*. Significant gene induction was observed in the implanted cells with only two pulses of 5-min FUS stimulation (FUS+, after), in comparison to the basal level (FUS+, before) and the control groups (FUS-, before and after) (Fig. 4.3, G and H).

4.2.4. FUS-inducible tumor cytotoxicity of the engineered CAR T cells in vivo

We next tested the tumor cytotoxicity of the FUS-inducible CAR T cells *in vivo*. We subcutaneously injected Nalm-6 cells (Fluc+) on both hindlimbs of NSG mice to generate matched bilateral tumors (Fig. 4.4A). Four days later, engineered CD19CAR T cells were subcutaneously injected at both tumor sites locally, followed by three pulses of 5-min FUS stimulation at 43°C on the left but not on the right tumor (Fig. 4.4A). Bioluminescence imaging revealed that FUS significantly suppressed tumor growth (Fig. 4.4, B and C). The results on the two tumors (FUS+ and FUS-) on the same mouse indicate that the FUS-activated CAR T cells at the local site had negligible off-site effects in attacking the distal tissues on the contralateral

hindlimb expressing the same antigens. We further performed a control experiment subjecting

mice carrying bilateral tumors to FUS stimulation on one side; with neither site subjected to the

injection of engineered CAR T cells (fig. 4.S4A). The tumors with or without FUS stimulation

exhibited similar growth profiles, indicating that FUS itself (with the chosen pattern) had no

impact on tumor growth (fig. 4.S4, B and C). Therefore, our results demonstrated that FUS can

be used to control the cytotoxicity of the engineered CD19CAR T cells *in vivo* against target

tumor cells.

We further tested this acoustogenetic technology in controlling inducible CAR T cells

against other types of tumors, particularly solid tumors. We engineered solid tumor human

prostate cancer PC3 cells to express the prostate-specific membrane antigen (PSMA) and Fluc,

and engineered primary human T cells with the Cre-lox mediated heat-inducible anti-PSMA

CAR (PSMACAR; fig. 4.S5A). We verified the functionality of the heat-inducible PSMACAR T

cells through *in vitro* co-culture cytotoxicity assays and the associated cytokine assays (fig. 4.S5,

B to D). We then generated matched bilateral subcutaneous PC3 tumors (PSMA+, Fluc+) in

NSG mice; five days later we subcutaneously injected heat-inducible PSMACAR T cells

immediately next to the tumor sites on both sides. The tumor regions on the left side were treated

with three pulses of 5-min FUS, while those on the right remained untreated. Consistently, the

tumors with FUS stimulation showed significantly inhibited growth as compared to the ones

without (Fig. 4.4, D and E). We further harvested the tumor tissues and quantified the related

mRNA amount. The CD3 mRNA in the FUS-treated tumors averaged 3-fold of that in the

untreated ones, indicating more T cell infiltration in the FUS-treated solid prostate tumors (fig.

4.S6A). Moreover, the amount of Cre-mediated recombined CAR mRNA in the FUS-treated

tumors was 9-fold of that in the untreated controls, verifying the FUS-induced DNA

recombination and subsequent CAR expression in the engineered T cells at the tumor sites (fig. 4.S6 and Methods). These results demonstrated the efficacy of FUS-based acoustogenetics in remote control of CAR T cells for treating different types of tumors *in vivo*, including solid tumors of prostate cancer.

4.3. Discussion

We developed an FUS-based acoustogenetic approach to remotely control the genetically engineered T cells capable of directly perceiving ultrasound signals and transducing them into genetic and cellular activations for therapeutic applications *in vivo*. This acoustogenetics technology enables the activation of CAR T cells at confined tissue regions, thus allowing the flexibility to target less ideal antigens without causing non-specific off-site cytotoxicity. This is of critical importance given the extensive overlap of antigens between tumors and normal cells under conditions of tissue injury and inflammation. The short-pulsed patterns of FUS stimulation should also minimize potential detrimental effects of hyperthermia.

We employ the Cre-mediated gene switch to convert transient FUS inputs into sustained outputs of genetic and cellular activities for sufficient therapeutic efficiency. The nature of local activation should limit the number of activated cells off the tumor site and the potential non-specific cytotoxicity against normal tissues (Fig. 4.4, B to E); if the Cre-mediated permanent activation of CAR becomes an issue in the future, degradation domains such as dihydrofolate reductase (DHFR) can be fused to CAR to control the protein lifetime with an FDA-approved drug methotrexate (*22*). This "AND" gate with FUS and methotrexate should enhance the precision of controllable CAR T immunotherapy.

We anticipate that comparable therapeutic outcomes can be achieved in a reversible heat-inducible system without the Cre-lox gene switch, but this will require multiple rounds of FUS

stimulation. In such a system, Hsp directly drives the production of CAR (Hsp-CAR) under FUS stimulation. Upon the withdrawal of FUS stimulation, HSFs gradually dissociate from Hsp, returning Hsp and its downstream transcriptional activities to the resting state. This recovery process has been reported to occur within 45 min after HS for *Drosophila* Hsp70 and approximately 60 min after HS for human Hsp70 (*23, 24*). The dynamics of the heat-induced CAR expression depends largely on its protein lifetime. Therefore, repeated FUS stimulation can be applied to maintain the CAR expression in the T cells (and hence their cytotoxicity) for a sustained period of time. We tested this concept by applying a 10-min HS every 48 hr in T cells with Hsp-eGFP, and indeed observed oscillatory patterns of the induced eGFP expression (fig. 4.S7). We anticipate that T cells with Hsp-CAR can also be repeatedly activated by FUS to achieve sustained CAR expression and cytotoxicity for a desired period of time or until tumor elimination. Such a reversible FUS-inducible system can further prevent "on-target off-tumor" toxicity of canonical CAR T therapy, as the T cells leaving the tumor site will no longer receive FUS stimulation and gradually lose CAR molecules. The half-life of GFP-tagged CAR has been reported to be ~8 hr (*10*).

We chose local injection at the tumor site to deliver T cells *in vivo*. Local administration of CAR T cells has been tested in animals and patients to overcome the obstacle of T cell homing associated with intravenous delivery, and has achieved promising therapeutic effects (*10, 25, 26*). In fact, the majority of patients diagnosed with prostate cancer in the United States harbor locally progressed prostate cancer (*27*), who are at increased risk of disease progression if without radical surgery or radiation therapy (*28*). Since the prostate is positioned near critical organ structures including urethra and neurovascular bundles, surgery or radiation therapy targeting the whole prostate gland may cause adverse effects that would significantly impact quality of life

(*29*). Local delivery and activation of inducible CAR T cells using clinically available MRI-guided FUS systems should allow, without nanoparticles or cofactors, a high degree of precision and safety in eradicating tumor cells in these patients harboring locally progressed prostate cancer (*29*). In cases where intravenous delivery is required, it is also possible to equip the FUS-inducible CAR T cells with additional antigen binders and/or chemokine receptors to promote trafficking and infiltration to the tumor site (*30, 31*), followed by FUS activation.

Each component of this FUS-based acoustogenetics, i.e. ultrasound devices, molecular thermo-sensors, and genetic/epigenetic transducing modules, is highly modular and will continue to evolve for greater precision and reduced immunogenicity. In fact, stretchable electronic circuits are being developed to fabricate wearable patches of ultrasound transducers (*32*). The leverage of technological advancements of different fields into FUS-based acoustogenetics should be able to drive the development of these fields to open up new frontiers. We envision that the current state of acoustogenetics is analogous to optogenetics at its infancy. Before the functional demonstration of channelrhodopsin in neuronal cells (*33*), it was challenging to manipulate molecular activities in live cells at high spatiotemporal resolutions. With the technological integration and convergence of optics, genetic circuits, and light-sensitive proteins, optogenetics is rapidly reaching its full potential. Based on this analogy, acoustogenetics may undergo a similar trajectory to provide a broadly applicable method and usher in an era of applying ultrasound for the direct, remote, and noninvasive control of genetically engineered cells for therapeutics.

4.4. Acknowledgments

4.5. Methods

Cloning

Plasmids used in this paper are listed in Table 4.S1. Cloning strategies include Gibson Assembly (NEB, E2611L) and T4 ligation (NEB, M0202L). PCR was performed using synthesized primers (Integrated DNA Technologies) and Q5 DNA polymerase (NEB, M0491). The sequences of the constructed plasmids were verified by Sanger sequencing (Genewiz).

General cell culture

HEK 293T cells were cultured in DEME (Gibco, 11995115) with 10% FBS (Gibco, 10438026) and 1% Penicillin-Streptomycin (Gibco, 15140122). Jurkat, Nalm-6, and PC3 cells were cultured in RPMI 1640 (Gibco, 22400105) with 10% FBS and 1% P/S. Primary human T cells were cultured in complete RPMI 1640 supplemented with 100 U/mL recombinant human IL-2 (PeproTech, 200-02). Cells were cultured at 37°C in a humidified 5% CO_2 incubator.

Staining and flow cytometry

Staining of cell surface markers (e.g., c-Myc, CD69, etc) for flow cytometry was performed using fluorophore-conjugated antibodies according to manufacturers' protocols. In general, cells were washed twice and resuspended in 100 μL wash buffer (PBS + 0.5% BSA) containing the suggested amounts of antibodies, incubated in dark at room temperature for suggested durations, and washed three times before being analyzed using a BD flow cytometer. Gating was based on non-engineered cells with the same staining. Flow cytometry data were analyzed using FlowJo software (Tree Star).

***In vitro* heat shock**

For Fig. 4.1C and Video 4.S1, cells seeded in a glass bottom dish were heated at 43°C for 15 min using a heating stage (Instec) integrated with a Nikon Eclipse Ti inverted microscope. Images were acquired in real-time to obtain the kinetics of the induced fluorescent protein. For the remainder of the *in vitro* heat shock (HS) experiment, unless otherwise specified, cells were washed and resuspended in cell culture medium at a concentration of 2×10^6 cells/mL, aliquoted into 8-strip PCR tubes with 50 μL/tube, and heat shocked at 43°C using a thermal cycler (Bio-Rad, 1851148) with various patterns as indicated (Table 4.S2). Cells were returned to standard

culture condition after HS. The gene induction levels were quantified by flow cytometry 12 hr

after HS in Fig. 4.1, F and G, and fig. 4.S3, D and E.

Engineered cells

The engineered cells (excluding primary human T cells) used in this work are listed in

Table 4.S3. Lentiviruses were used to deliver engineered genes into the cells. Fluorescence-

activated cell sorting (FACS), when needed, was performed at UCSD Human Embryonic Stem

Cell Core Facility by professional technicians following standard protocols.

Quantification of CAR expression in Jurkat cells

Jurkat cells were either transduced with a lentiviral cocktail (inducible Cre and lox-stop

CAR reporter, Fig. 4.2A) followed by indicated HS (fig. 4.2B), or transduced with the lox-stop

CAR reporter lentivirus alone without HS. CAR expression was quantified by CAR antibody

staining (an anti-mouse IgG, F(ab')$_2$ fragment specific antibody; Jackson ImmunoResearch, 115-

606-072) and flow cytometry 24 hr after HS. Live single cells were gated for CAR expression

analysis. Non-engineered Jurkat cells were stained with the same antibody to generate the CAR+

gate.

Quantification of CD69 expression in Jurkat cells

Jurkat cells transduced with a lentiviral cocktail (inducible Cre and lox-stop CAR

reporter, Fig. 4.2A) were treated with or without HS at 43°C for 15 min, and co-cultured with

target tumor cells for 24 hr. The cells were then stained by an APC anti-human CD69 antibody

(BioLegend, 310910) and analyzed by flow cytometry. ZsGreen+ cells (representing the

engineered Jurkat cells) were gated for analysis of CD69 expression. Non-engineered Jurkat cells co-cultured with target tumor cells were stained with the same antibody to generate the CD69+ (APC+) gate.

Isolation, culture, transduction and MACS of primary human T cells

Human peripheral blood mononuclear cells (PBMCs) were isolated from buffy coats (San Diego Blood Bank) using Lymphocyte Separation Medium (Corning, 25-072-CV) following the manufacturer's instructions. Primary human T cells were isolated from PBMCs using Pan T Cell Isolation Kit (Miltenyi, 130-096-535) and activated with Dynabeads® Human T-Expander CD3/CD28 (Gibco, 11141D). Three days later, lentivirus concentrated using PEG-it (SBI, LV825A-1) was added to the T cells at MOI = 10, followed by spinoculation in a 96-well plate coated with Retronectin (Takara, T100B). T cells were further expanded and dynabeads were removed prior to downstream procedures (e.g., magnetic-activated cell sorting (MACS), *in vitro* HS, *in vivo* injection, etc.).

For *in vitro* and *in vivo* cytotoxicity studies, T cells were transduced with a lentiviral cocktail of inducible Cre and lox-stop CAR reporter (Fig. 4.2A). MACS was performed using Anti-c-Myc-Biotin antibodies and Anti-Biotin microbeads (Miltenyi, 130-092-471 and 130-097-046) following the manufacturer's instructions to enrich c-Myc+ cells. A representative double positive efficiency after MACS is 69%, 95% for the c-Myc+ and 71.4% for the ZsGreen+ cells (fig. 4.S2B). CAR expression in the engineered inducible CAR T cells with or without HS was quantified using the CAR antibody as described above.

Luciferase-based cytotoxicity assay

A constant number of 5×10^4 Fluc+ Nalm-6 cells were mixed with engineered primary human T cells with or without HS (pre-washed and resuspended with complete RPMI without IL-2) at effector-to-target (E:T) ratios of 1:50, 1:20, 1:10, 1:5, 1:1, 5:1 or no T cells ("target cell only"). The mixtures were then cultured in round bottom 96 well plates for 24 hr, centrifuged to remove the supernatant (which was harvested for quantification of cytokine production), and assayed with the Bright-Glo^{TM} Luciferase Assay System (Promega, E2610) following the manufacturer's instructions to quantify the luminescence of each sample. The cytotoxicity (%) of Sample X was calculated as (1- Luminescence of X / Luminescence of "target cell only") x 100%.

For cytotoxicity assay using PC3 cells as the target, 1×10^4 PSMA+ Fluc+ PC3 cells were seeded onto TC-treated flat bottom 96 well plates (Corning, 3603). Except for "target cell only" wells, engineered primary human T cells with or without HS (washed and resuspended with complete RPMI without IL-2) were added 6 hr later at E:T ratios of 1:10, 1:5, 1:1, 5:1, 10:1, 20:1. The luminescence was quantified 24 hr after co-culture as described above.

Quantification of cytokine production

The supernatant of effector-target cell co-culture was harvested. The concentrations of cytokines IL-2 and IFN-γ were quantified using the corresponding ELISA kits (BD, 555190 and 555142).

T cell viability assay

Non-engineered primary human T cells were heat shocked as described above and kept under normal culture condition for 24 hr. Cell viability was then assessed using the FITC

Annexin V Apoptosis Detection Kit I (BD, 556547) following the manufacturer's instructions. The cells stained negative for both Annexin V and PI were counted as live cells.

MRI-guided FUS

The MRI-guided FUS system is composed of a 1.5 MHz 8-element annular array transducer, a 16-channel broadband RF generator, a piezo motor-based X-Y positioning stage, and a degassing and water circulation system (Image Guided Therapy, France). MR images acquired using a Bruker 7T MRI system were transferred to ThermoGuide software (Image Guided Therapy, France) to generate phase images and real-time temperature maps. Using PID controller, the software automatically regulates the output power of the generator to maintain the temperature at the focal spot at a desired value as described elsewhere (*19, 34*).

Animal experiments were performed following Protocol S15285 approved by UCSD IACUC. NSG mice (6-8 weeks old) were purchased from Jackson Laboratory (JAX) and shaved prior to FUS stimulation. Anesthesia was induced using 2% isoflurane-oxygen mixture and maintained with 1.5% isoflurane-oxygen mixture during FUS stimulation. The mouse was laid on its side on an MR bed containing a surface coil. A pressure pad was placed under the mouse to monitor its respiration rate, and a rectal thermal probe was used to provide feedback for the delivering of warm air into the bore to maintain the mouse's core temperature at approximately 37°C. The ultrasound transducer was positioned right above the targeted region on the mouse's hindlimb. Thin layers of SCAN ultrasound gel (Parker labs) were applied at the skin-transducer and skin-bed interfaces.

The ThermoGuide software regulates the temperature in a 3 x 3 pixel square (3 - 4 mm^2) centered at the ultrasound focus (Fig. 4.3E). A PID controller is used to maintain the average

temperature of the target square at 6°C above reference by controlling the output power of the FUS generator, with the reference temperature being 37°C as measured by the rectal thermal probe. As such, the MRI-guided FUS enabled temperature elevation to 43°C locally at the focal area in the hindlimb of an anesthetized mouse.

FUS stimulation in tofu phantom

For FUS stimulation on cells in the tofu phantom, Nalm-6 cells were lentivirally transduced with the dual-luciferase reporter (Fig. 4.3B, Hsp-Fluc-PGK-Rluc-mCherry) and FACS-sorted. The cells were resuspended in culture medium and mixed with matrigel (Corning, 354262) at 1:1 volume ratio on ice. Extra-firm tofu was cut into a 15-mm thick pad, and an 8-mm deep hole of 8-mm diameter was drilled from the top. A microcentrifuge tube of 7.5-mm diameter (Fisherbrand, 05-408-120) was cut to 8-mm long by removing the cap and the conical bottom, and was inserted into the hole in the tofu phantom. Cell-matrigel mixture of 150 µL was added into the hole (~3 mm thick) and allowed to gel at room temperature. The rest of the hole and the gap between the tube and the tofu phantom were filled up with matrigel. After gelation, the assembly was inverted and positioned onto the MR bed containing the surface coil. The ultrasound transducer was positioned above the tofu phantom with its center aligned with that of the tube. Thin layers of ultrasound gel were applied at the tofu-transducer and tofu-bed interfaces. A thermal probe was inserted into the distal end of the tofu phantom to provide reference temperature readings.

MR images of the assembly were acquired and transferred to ThermoGuide to calculate the theoretical ultrasound focal position. Test FUS shots were delivered to determine the actual focal position. Steering was applied to focus the ultrasound at the region immediately above the

77

cells. Three pulses of 5-min FUS stimulations at 43°C were applied. The cell-matrigel mixture was then recovered from the tube, placed in cell culture medium, and returned to a standard 37°C cell culture incubator. After 6 hr, the culture was centrifuged to remove the supernatant, and the cell-matrigel pellet was incubated in a Cell Recovery Solution (Corning, 354253) at 4°C for 1 hr to retrieve the Nalm-6 cells from matrigel. The Fluc and Rluc luminescence of the cells was quantified using the Dual-Luciferase® Reporter Assay System (Promega, E1910) following the manufacturer's instructions.

In vivo bioluminescence imaging

In vivo bioluminescence imaging (BLI) was performed using an In vivo Imaging System (IVIS) Lumina LT Series III (PerkinElmer). For Fluc imaging, 150 mg/kg D-Luciferin (GoldBio, LUCK) was administered intraperitoneally (i.p.). BLI started 10 min after substrate injection until peak signal was acquired. For Rluc imaging, 200 µL 0.295 mM ViviRen™ (Promega, P1232) (*57*) was administered i.p. BLI started 15 min after substrate injection until peak signal was acquired. BLI of Fluc and Rluc in the same mouse, when needed, was performed 4 hr apart. Images were analyzed using Living Image software (PerkinElmer), and the integrated Fluc luminescence intensities within regions of interest were quantified to represent tumor sizes.

FUS-inducible gene activation *in vivo*

NSG mice (male, 6-8 weeks old) were subcutaneously injected with 2×10^6 dual-luciferase reporter Nalm-6 cells at the hindlimb. One week later, the experimental mice received two pulses of 5-min FUS stimulation at 43°C targeted at the implanted cells, while the control

mice remained unstimulated. The *in vivo* Fluc and Rluc luminescence was quantified 4 hr before and 12 hr after FUS stimulation, as described above.

In vivo tumor cytotoxicity of FUS-inducible CAR T cells.

NSG mice (male, 6-8 weeks old) were subcutaneously injected with 2×10^5 Fluc+ Nalm-6 cells (or 2×10^5 PSMA+ Fluc+ PC3 cells, for PC3 tumors) on both hindlimbs to generate matched bilateral tumors. Four days later (or five days later, for PC3 tumors), 1×10^6 inducible primary human CAR T cells prepared as described above were injected subcutaneously and locally at tumor regions. Within 4 - 8 hr after T cell injection, three pulses of 5-min FUS stimulation targeted at 43°C were applied on the left tumor region as described above, while the tumor on the right hindlimb received no FUS stimulation to serve as the control. Tumor aggressiveness was monitored by BLI twice a week as described above until euthanasia criteria were met.

**Quantification of mRNA expression in tumor tissue.**

PC3 tumors (Fig. 4.4, D and E) were harvested 22 days after tumor implantation (17 days after T cell injection and FUS stimulation). The tumors were disrupted and homogenized, and the same amount of lysate from each tumor was used to extract total RNA with the RNeasy Mini Kit (Qiagen, 74104) followed by reverse transcription using the same amount of template RNA. Quantitative PCR (qPCR) was performed using iTaq™ Universal SYBRRTM Green Supermix (Bio-Rad, 1725121), the same amount of template cDNA, and the specific primers described below. The mRNA levels were normalized to b-actin.

The first pair of specific primers were designed on human CD3 g chain to detect the presence of human T cells. The second pair of specific primers were designed based on the lox-stop PSMACAR reporter sequence to reflect CAR expression after FUS-induced Cre recombination (fig. 4.S6, A and B). The forward primer anneals from -60 bp of the mouse PGK promoter, downstream of the transcription starting site (TSS), and the reverse primer anneals from +20 bp of the PSMACAR gene (*35*). With the presence of FUS-induced Cre recombinase, the sequence from the second half of LoxH to the first half of LoxP will be excised, resulting in a 200 bp qPCR product. Without Cre-mediated recombination, this pair of primers will theoretically generate a 984-bp fragment. We adopted a two-step qPCR protocol with combined annealing/extension at 60°C for only 15 sec to ensure the specific amplification of the 200-bp fragment, but not the 984 bp fragment, as confirmed by gel electrophoresis and Sanger sequencing of the qPCR product (fig. 4.S6, C and D; sequence alignment performed in Serial Cloner). Therefore, the second pair of specific primers can detect the successfully recombined CAR mRNA amount.

Statistics.

One-way ANOVA followed by Tukey's multiple comparisons test is used for Figs. 4.1, F and G, and fig. 4.S3, B and D to E. Student's t-test is used for Fig. 4.2D. Two-way ANOVA followed by Sidak's multiple comparisons test is used for Figs. 4.2, B, G to I, 4.3G, 4.4, B and D, fig. 4.S4B, 4.S5, B to D.
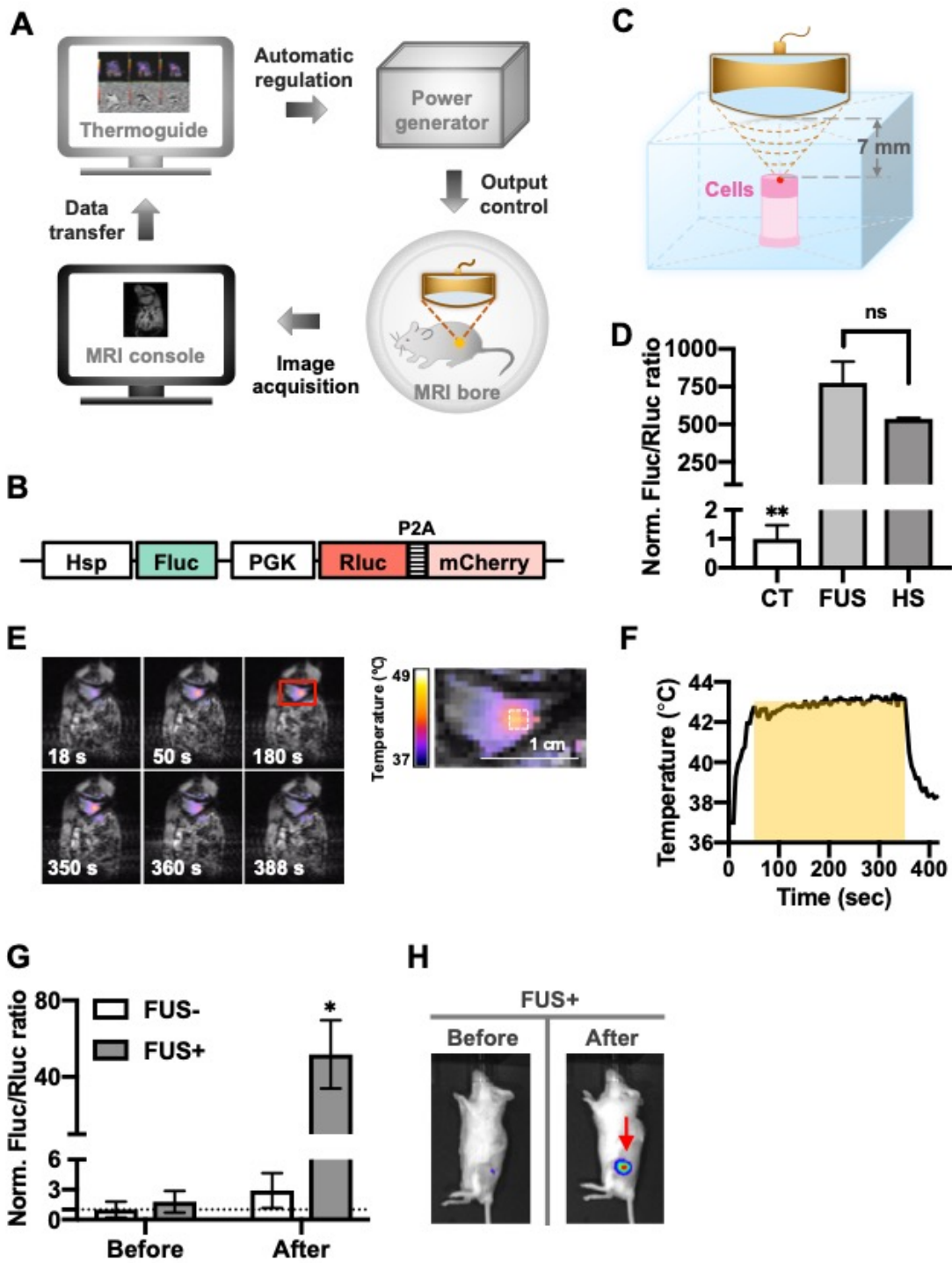
Figure. 4.1. Heat-inducible gene activation. (A) Design of the FUS-controllable CAR T therapy technology. T cells engineered with the heat-inducible CAR and localized at the tumor region are activated by MRI-guided FUS for recognizing and eradicating target tumor cells. **(B)** Schematics of the dual-promoter eGFP reporter. **(C-D)** **(C)** Fluorescent images of inducible eGFP and constitutive mCherry, and **(D)** the percentage of eGFP+ cells and their mean fluorescence intensity after a 15-min HS at 43°C in HEK 293T cells containing the dual-promoter reporter. **(E-G)** Gene induction in primary human T cells with the dual-promoter eGFP reporter. **(E)** Representative flow cytometry profiles of eGFP expression. **(F)** The percentage of eGFP+ cells and **(G)** their mean fluorescence intensity. In (E-G), CT: without HS; HS: with a continuous 15-min HS. MCherry+ cells were gated for eGFP analysis. N = 3 repeats; error bar: SEM. ****: $p < 0.0001$.
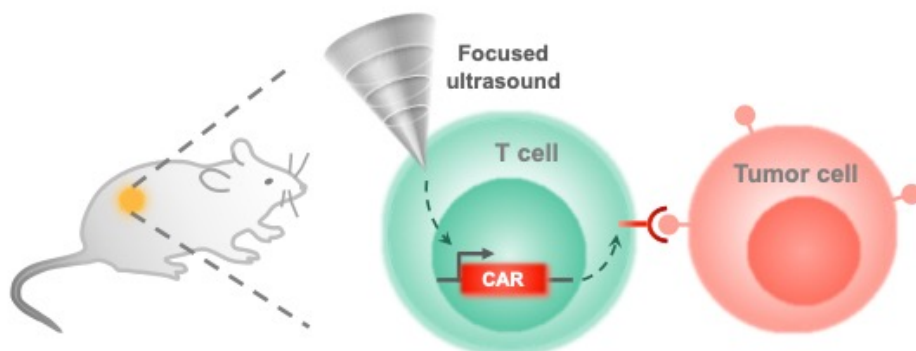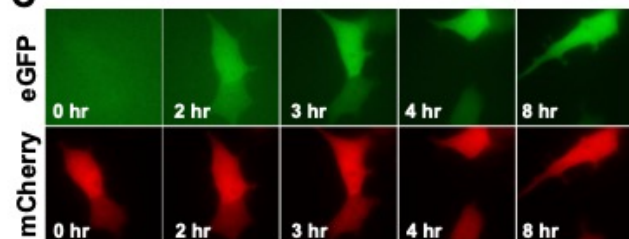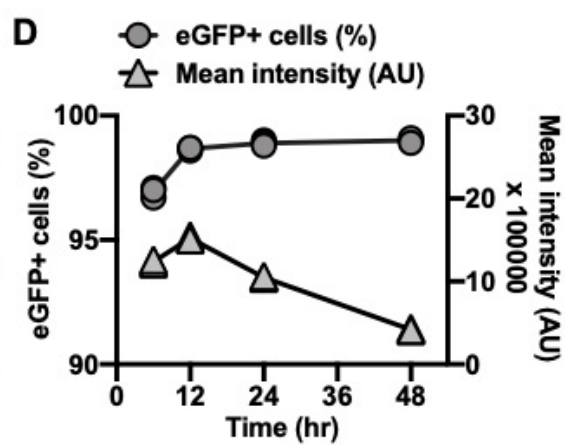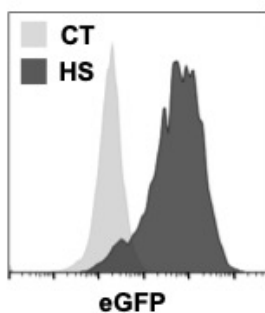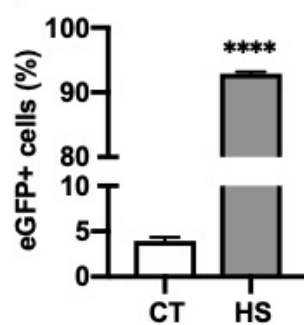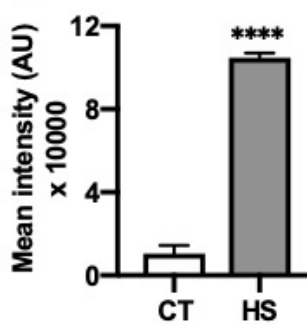
Figure. 4.2. Heat-inducible CD19CAR expression and functional outcomes in Jurkat and primary T cells. (A) Schematics of the transgenes: the inducible Cre and the lox-stop CAR reporter. **(B)** Inducible CAR expression in Jurkat cells hosting the lox-stop CAR reporter alone (lox), or both transgenes in (A) with (HS) or without HS (CT). **(C)** Schematics of assays accessing the functionality of the heat-induced CAR T cells, including CD69 expression, cytotoxicity, and cytokine release. **(D)** The percentage of CD69+ cells in Jurkat with both transgenes in (A). **(E)** Representative flow cytometry data showing the histogram of CD69 expression in (D). **(F)** Representative histograms showing the percentage of CAR+ cells in primary T cells with both transgenes in (A). **(G)** The cytotoxicity of the T cells in (F) against Nalm-6 tumor cells at various E:T ratios. **(H-I)** Quantification of **(H)** IFN-γ and **(I)** IL-2 cytokine release associated with (G). Arrow: cytokine level not detectable. In (B) and (D) to (F), CT: without HS; HS: with a continuous 15-min HS. N = 3; error bar: SEM. ***: p < 0.001; ****: p < 0.0001; ns: no significant difference.

84
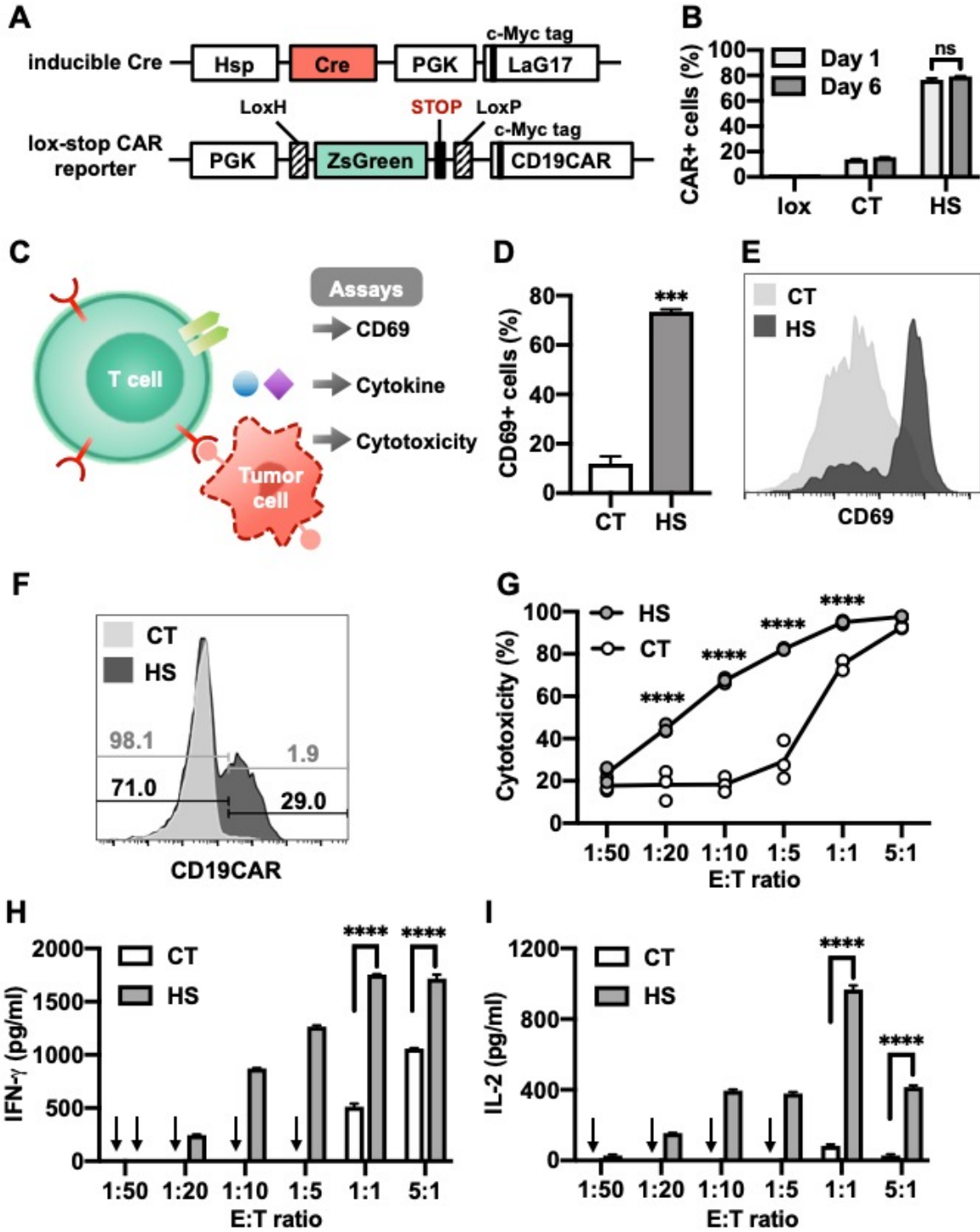
Figure. 4.3. MRI-guided FUS-inducible gene activation in phantom and *in vivo*. (A) Schematics of the MRI-guided FUS system. **(B)** The dual-luciferase reporter containing the inducible Hsp-driven Fluc and constitutive PGK-driven Rluc fused with mCherry. **(C)** The experimental setup of FUS stimulation on cells in a tofu phantom. **(D)** Gene induction level in Nalm-6 cells containing the dual-luciferase reporter with three pulses of 5-min heating by MRI-guided FUS in tofu phantom (FUS) or by thermal cycler (HS). CT: without heating. Gene induction level is quantified by the Fluc/Rluc ratio and normalized to CT. N = 3. **(E)** Left: color-coded temperature map superimposed on MRI images at different time points during a 5-min FUS stimulation at 43°C on the hindlimb of an anesthetized mouse. Right: close-up of the red rectangle region on the left. The dotted white square outlines the region of interest (ROI) for temperature regulation. **(F)** The average temperature of the ROI during FUS stimulation in (E). The yellow shadow represents the predefined target temperature (43°C) and duration (300 sec) of FUS stimulation. **(G)** Gene induction *in vivo* by MRI-guided FUS. Nalm-6 cells containing the dual-luciferase reporter were injected subcutaneously into NSG mice followed by FUS stimulation. FUS+ or FUS-: with or without two pulses of 5-min FUS stimulation at 43°C. Gene induction was quantified by the *in vivo* Fluc/Rluc ratio and normalized to the "FUS-, before" group, as indicated by the dotted line. N = 4 mice. **(H)** Representative bioluminescence images of Fluc expression before and after FUS stimulation in (G). Error bar: SEM. *: $p < 0.05$; **: $p < 0.01$; ns: no significant difference.

A Thermoguide — Automatic regulation → Power generator — Output control → MRI bore — Image acquisition → MRI console — Data transfer

B Hsp — Fluc — PGK — Rluc — P2A — mCherry

C 7 mm — Cells

D Norm. Fluc/Rluc ratio — ns — ** — CT, FUS, HS

E 18 s, 50 s, 180 s, 350 s, 360 s, 388 s — Temperature (°C) 37–49 — 1 cm

F Temperature (°C) vs Time (sec)

G Norm. Fluc/Rluc ratio — FUS−, FUS+ — Before, After — *

H FUS+ — Before, After

86

Figure. 4.4. FUS-controllable tumor suppression by the engineered CAR T cells *in vivo*. (A) Timeline of the *in vivo* experiment using NSG mouse bearing matched bilateral tumors as the animal model. The tumor on the left flank received FUS stimulation (FUS+) and the one on the right received no FUS (FUS-) following injection of engineered CAR T cells. **(B-E)** The quantified tumor growth and representative bioluminescence images of **(B-C)** Nalm-6 tumors or **(D-E)** PC3 tumors with (FUS+) or without (FUS-) FUS stimulation. Tumor size was quantified using the integrated Fluc luminescence intensity of the tumor region and normalized to that of the same tumor on the first measurement. N = 4 mice. Error bar: SEM. *: $p < 0.05$; **: $p < 0.01$; ****: $p < 0.0001$.
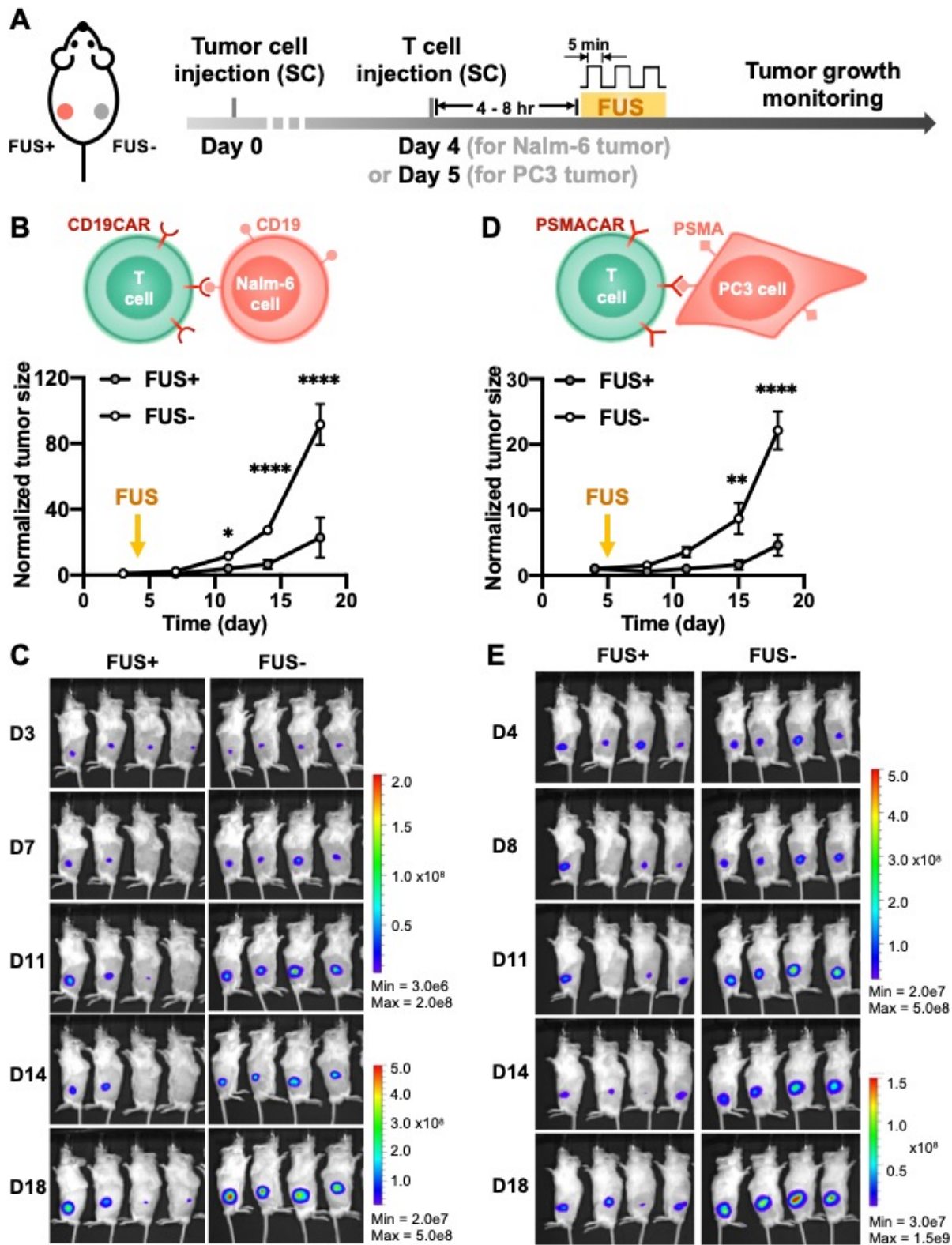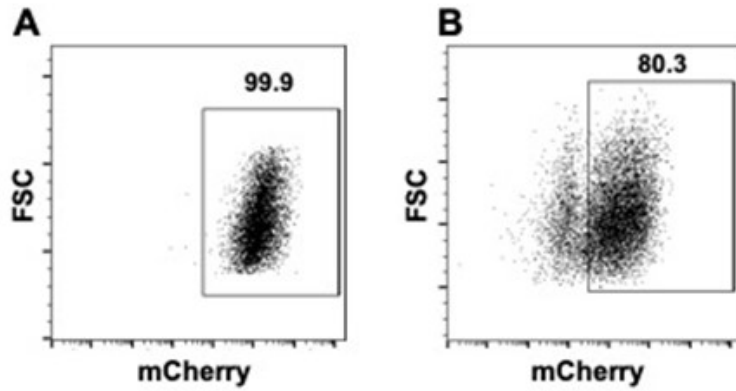
Figure. 4.S1. Transduction efficiencies of the dual-promoter eGFP reporter. Representative flow cytometry data showing the lentiviral transduction efficiencies of the dual-promoter eGFP reporter (Hsp-eGFP-PGK-mCherry) in **(A)** HEK293T cells (99.9%) and **(B)** primary human T cells (80.3%). The mCherry+ gates are based on the profiles of the corresponding non-engineered cells.
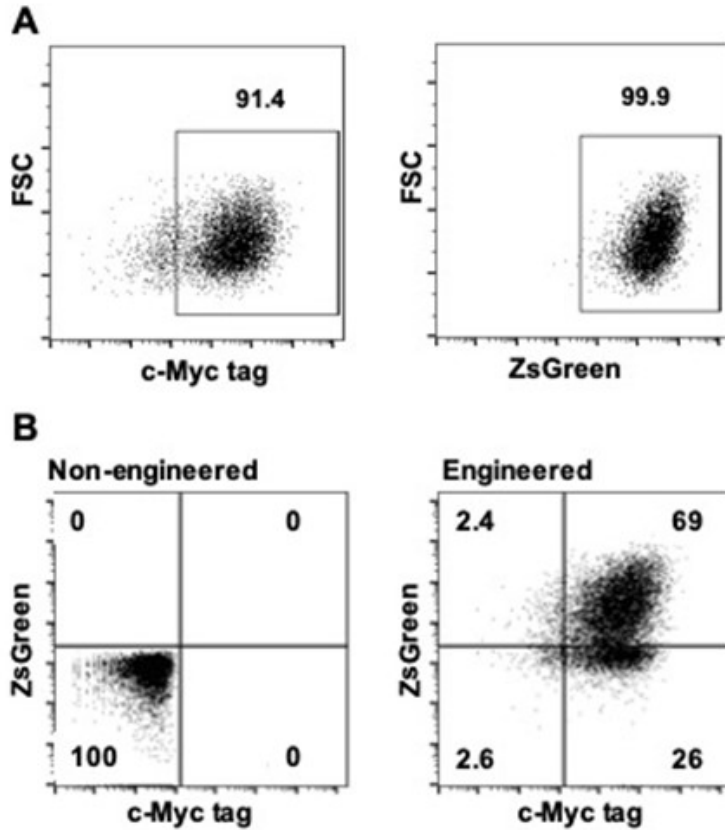
Figure. 4.S2. Transduction efficiencies of the heat-inducible Cre-lox system in Jurkat and primary human T cells. (A) Jurkat cells were lentivirally co-transduced with inducible Cre (Hsp-Cre-PGK-cMyc-LaG17) and lox-stop CAR reporter (PGK-LoxH-ZsGreen-stop-LoxP-CAR). Shown are the transduction efficiencies of cells without HS. **(B)** Primary human T cells were co-transduced with inducible Cre (Hsp-Cre-PGK-cMyc-LaG17) and lox-stop CAR reporter (PGK-LoxH-ZsGreen-stop-LoxP-CAR) lentiviruses. The cells were sorted through MACS for c-Myc+ cells. The representative transduction efficiency after MACS is 69% for the c-Myc and ZsGreen double positive, 95% for the c-Myc+ and 71.4% for the ZsGreen+ cells. Gating is based on the corresponding non-engineered cells with the same c-Myc antibody staining.

Figure. 4.S3. Thermal tolerance of primary human T cells. (A) Different patterns of HS. H: heating at 43°C; L: resting at 37°C. **(B)** The viability of non-transduced primary human T cells 24 hr after different patterns of HS in (A) assayed by Annexin V and PI staining. **(C)** Representative flow cytometry data of (B). **(D-E) (D)** The percentage of eGFP+ cells and **(E)** their mean fluorescence intensity in primary human T cells engineered with the dual-promoter eGFP reporter in Fig. 4.1B under different HS patterns in (A). N = 3 repeats; error bar: SEM. *: $p < 0.05$; ***: $p < 0.001$; ****: $p < 0.0001$; ns: no significant difference.
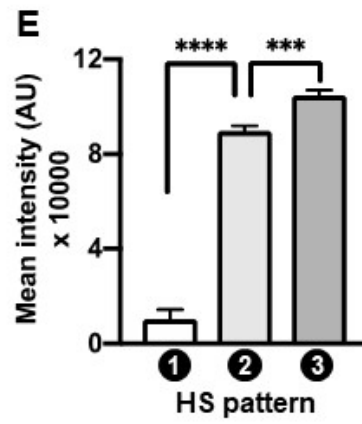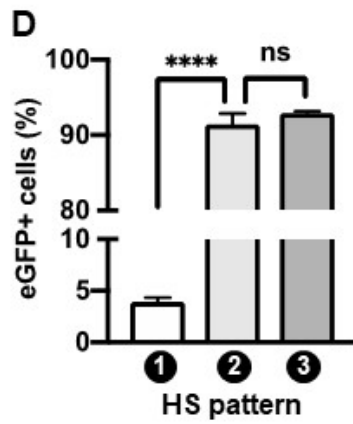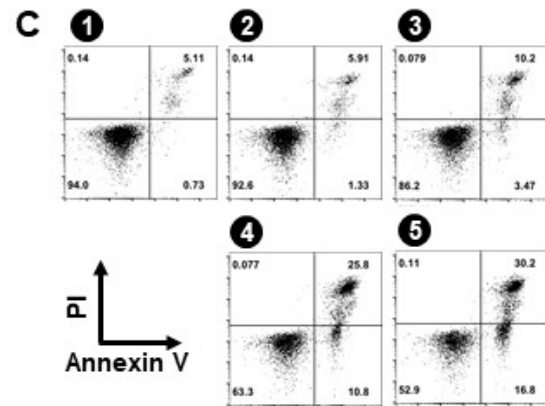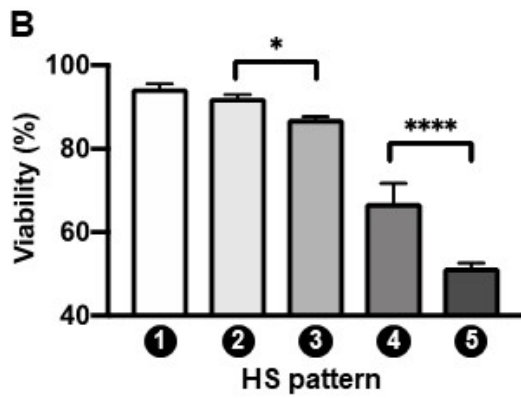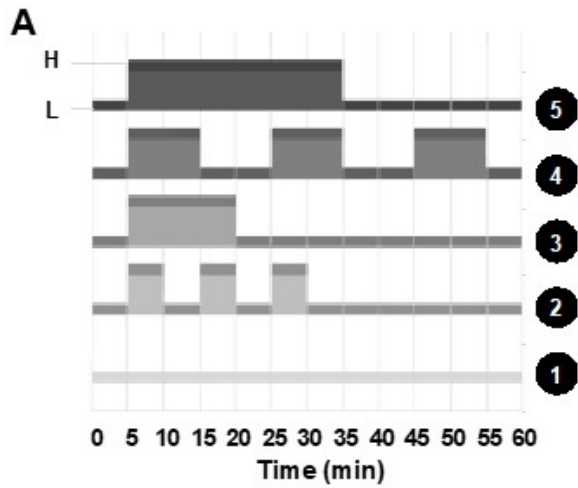
Figure. 4.S4. FUS has no detectable effect on tumor growth. (A) Timeline of *in vivo* experiment. Fluc+ Nalm-6 cells are subcutaneously injected into NSG mice to generate matched bilateral tumors. Four days later, three pulses of 5-min FUS stimulation targeted at 43°C was applied on the tumor on one side (left), while the tumor on the other side (right) received no FUS stimulation. Tumor growth after FUS stimulation was monitored by bioluminescence imaging. **(B-C)** The **(B)** quantified tumor growth and **(C)** representative bioluminescence images of the tumors with (FUS+) or without (FUS-) FUS stimulation. Tumor size is quantified using the integrated luminescence intensity and normalized to that of the same tumor on the first measurement. N = 5 mice. Error bar: SEM. No significant difference was detected.

A

Tumor cell injection (SC)

5 min

FUS

Day 0   Day 4   Tumor growth monitoring

B

C

Min = 1.0e7
Max = 1.0e9

94
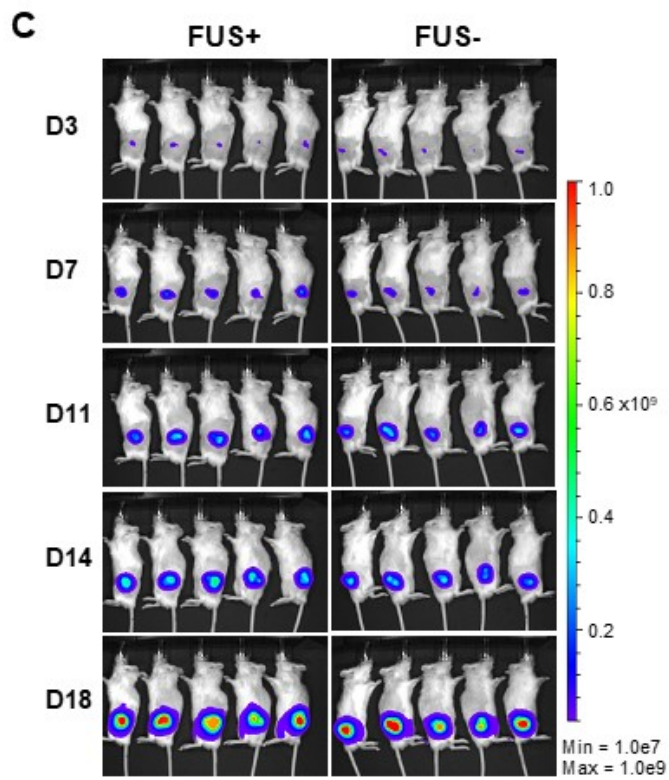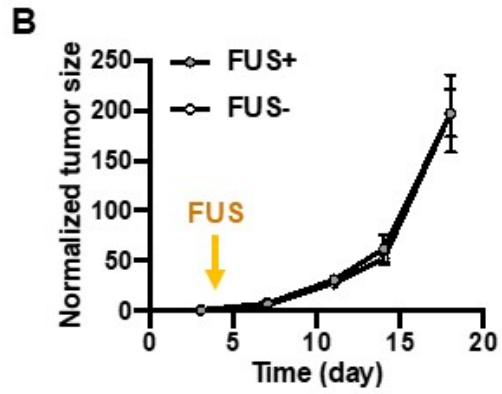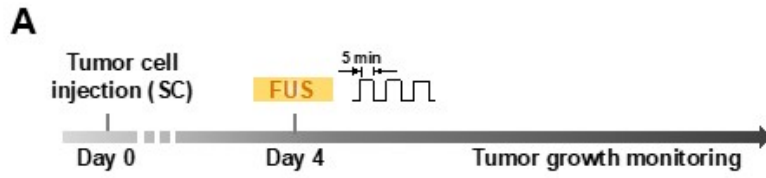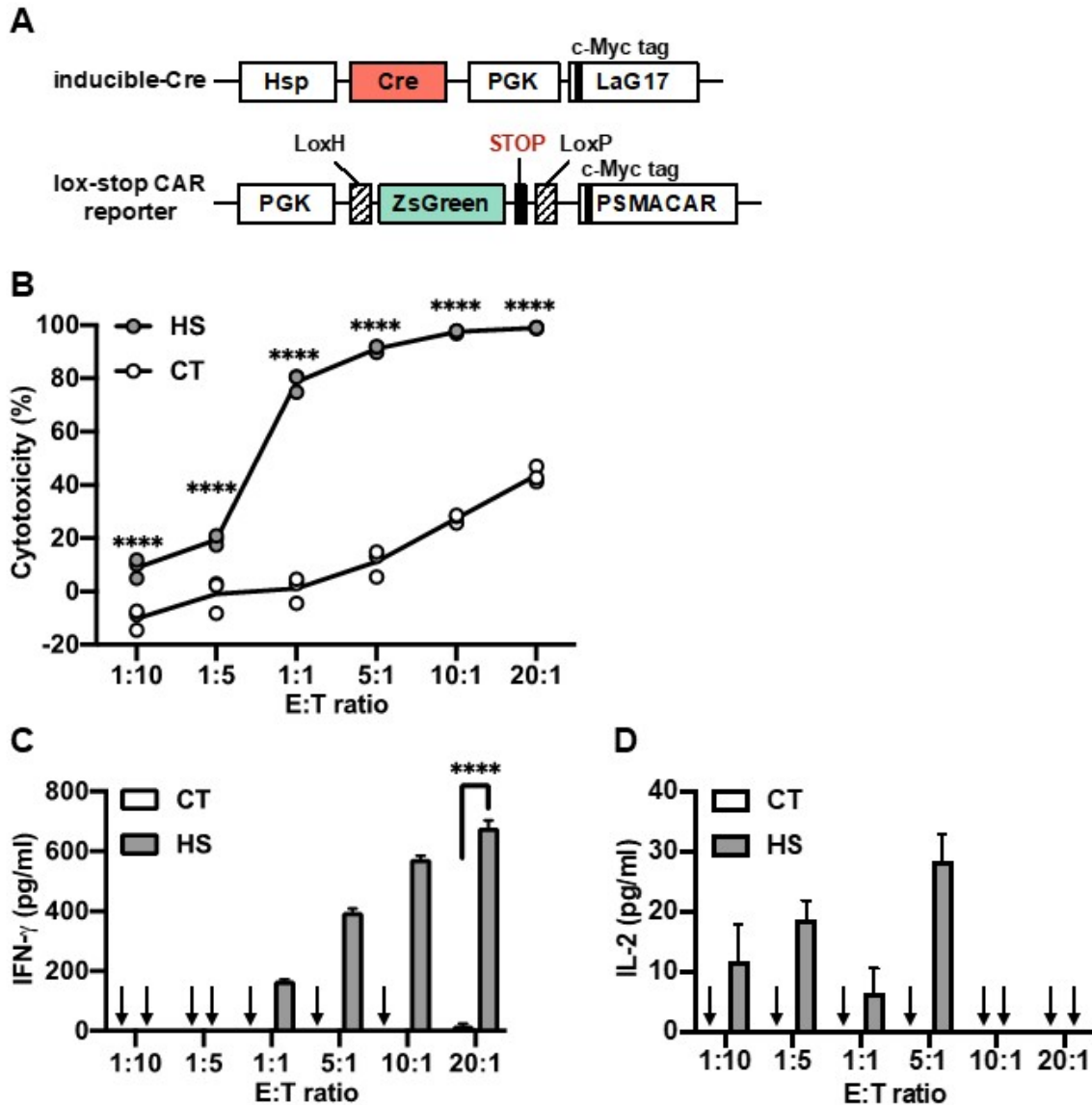
Figure. 4.S5. Functionality of the heat-inducible PSMACAR T cells *in vitro*. (A) Schematics of the transgenes used in this figure, including the heat-inducible Cre and the lox-stop PSMACAR reporter. **(B)** Cytotoxicity of the T cells engineered with the transgenes in (A) against Fluc+ PSMA+ PC3 tumor cells at various E:T ratios. **(C-D)** Quantification of **(C)** IFN-γ and **(D)** IL-2 cytokine release associated with (B). Arrow: cytokine level not detectable. CT: without HS. HS: with a continuous 15-min HS. N = 3; error bar: SEM. ****: $p < 0.0001$.

Figure. 4.S6. Quantification of relative mRNA expression levels in tumors. (A) The expression levels of CD3 and CAR mRNA in tumors with FUS stimulation (fig. 4.4E, FUS+), with their values normalized to the corresponding mRNA levels in tumors without FUS stimulation (fig. 4.4E, FUS-). Dotted line: the corresponding mRNA levels in tumors without FUS stimulation are set to 1. **(B)** Schematics of the theoretical templates without (-Cre) or with (+Cre) Cre-lox recombination, and the expected products amplified by the designed primers. **(C)** Gel electrophoresis of the qPCR products of the tumors with FUS stimulation (FUS+) or without (FUS-). **(D)** Alignment of the combined Sanger sequencing results and the theoretical template with Cre-lox recombination.

A

Normalized mRNA expressions

CD3   CAR

15
10
5

B

-Cre

Forward primer   LoxH   STOP LoxP
PGK [ ] ZsGreen ▮ [ ] PSMACAR
Transcription Starting Site (TSS)
Reverse primer
984 bp

+Cre

Forward primer
PGK [ ] PSMACAR
200 bp
Reverse primer

C

1000 bp

200 bp

FUS- FUS+ Ladder
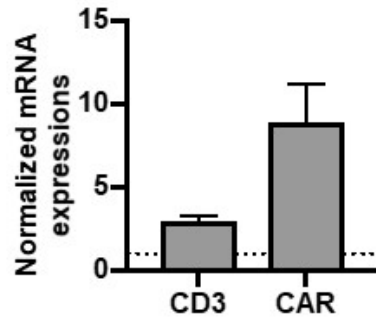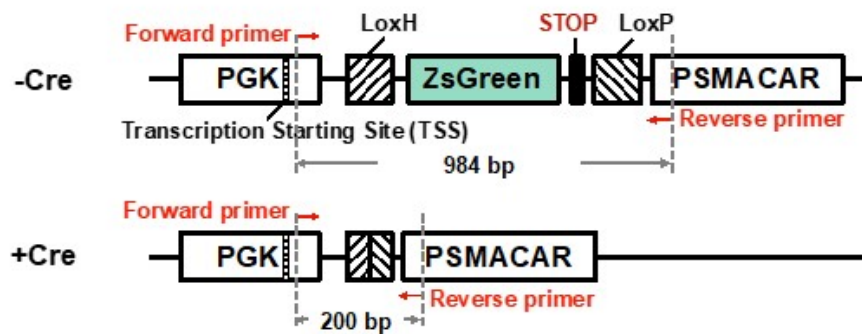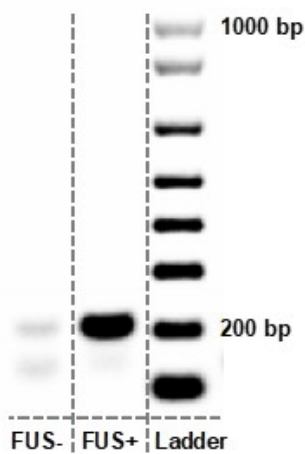
D

```
Seq_1  1    -acgcttcaaaagcgcacgtctgccccgctgttctcctcttcctcatctccgggcctttc  59
            |||||||||||||||||||||||||||||||||||||||||||||||||||||||||||
Seq 2  1    TACGCTTCAAAAGCGCACGTCTGCCGCGCTGTTCTCCTCTTCCTCATCTCCGGGCCTTTC  60

Seq 1  60   gacctgcagcccaagcttaccGAGACCCAAGCTGGCTAGAATTACCTCATATAGCATACA  119
            ||||||||||||||||||||||||||||||||||||||||||||||||||||||||||||
Seq_2  61   GACCTGCAGCCCAAGCTTACCGAGACCCAAGCTGGCTAGAATTACCTCATATAGCATACA  120

Seq_1  120  TTATACGAAGTTATGTTTcggcAATTCGCGCGCAggaattgatccttcgaactagtGGATC  179
            ||||||||||||||||||||||||||||||||||||||||||||||||||||||||||||
Seq_2  121  TTATACGAAGTTATGTTTCGGAATTCGCGCGCAGGAATTGATCCTTCGAACTAGTGGATC  180

Seq_1  180  CATGGCTCTCCCAGTGACTGC  200
            |||||||||||||||||||:::
Seq_2  181  CATGGCTCTCCCAGTGACNNN  201
```

Seq_1: theoretical sequence after Cre-lox recombination
Seq_2: combined Sanger sequencing results
Pink: PGK promoter (partial)
Green: first half of LoxH
Blue: second half of LoxP
Red: PSMACAR (partial)
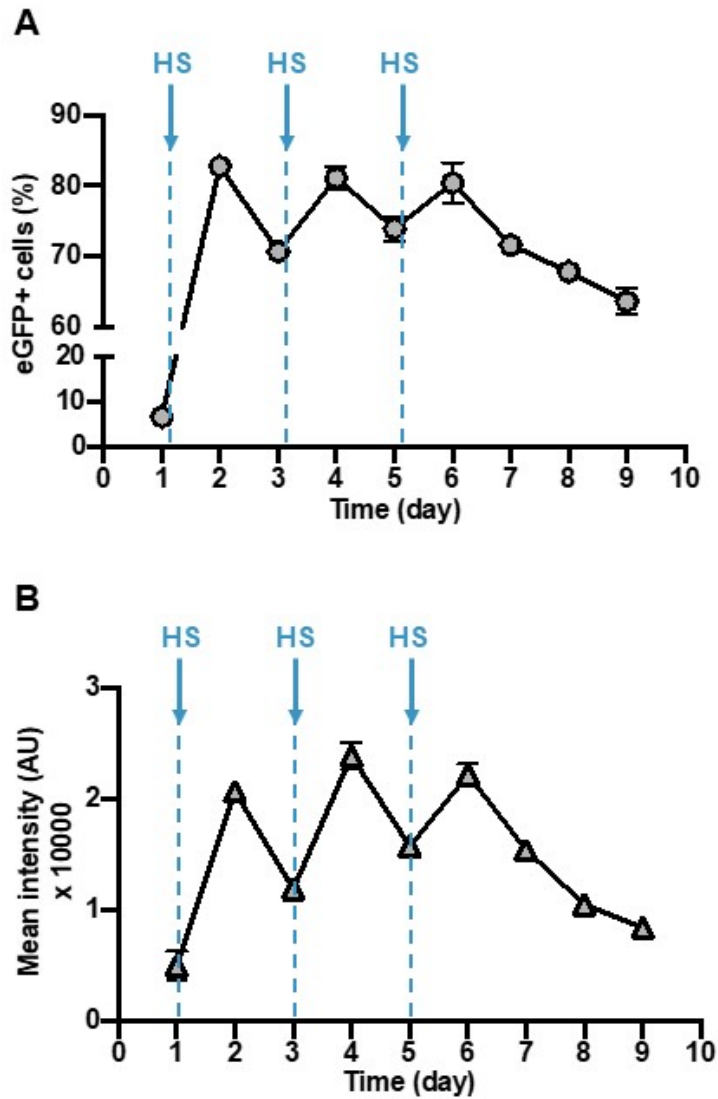
Figure. 4.S7. Gene activation with periodical HS. (A-B) The dynamics of eGFP expression in terms of **(A)** percentage of eGFP+ cells and **(B)** mean eGFP intensity in primary human T cells transduced with the dual-promoter eGFP reporter and subjected to a 10-min HS every 48 hr on Day 1, 3, and 5. N = 3; error bar: SEM.

Table 4.S1. Plasmids used in this Chapter 4. Detailed information on the plasmids used in this work, including the features of the constructs, their usage, and sources.

Plasmid	Purpose	Used in	Source
pHR-Hsp-eGFP-PGK-mCherry	inducible GFP reporter	Figs. 4.1C-G, 4.S1, 4.S7	This work
pHR-PGK-LoxH-ZsGreen-STOP-LoxP-cMyc-CD19CAR	Lox recombination CD19CAR reporter	Figs. 4.2B, 4.2D-I, 4.4B-C, 4.S2	This work
pHR-Hsp-Cre-PGK-cMyc-LaG17	inducible Cre	Figs. 4.2B, 4.2D-I, 4.4B-C, 4.S2, 4.S5, 4.S6	This work
pHR-Hsp-Fluc-PGK-Rluc-P2A-mCherry	inducible dual luciferase reporter	Fig. 4.3D, 4.3G-H	This work
pHR-PGK-LoxH-ZsGreen-STOP-LoxP-cMyc-PSMACAR	Lox recombination PSMACAR reporter	Figs. 4.4D-E, 4.S5, 4.S6	This work
pHR-PGK-PSMA	PSMA antigen	Figs. 4.4D-E, 4.S5	This work
pHIV-EF1a-Fluc-IRES-ZsGreen	firefly luciferase	Figs. 4.2G-I, 4.4B-E, 4.S4, 4.S5	Addgene #39196

99

Table 4.S2. Thermal cycler HS patterns used in Chapter 4. The patterns of different HS treatments performed in this work using a thermal cycler.

Pattern	Step	Temperature	Time
1		37°C	∞
2	Initial equilibrium	37°C	5 min
	3 Cycles	43°C	5 min
		37°C	5 min
3	Initial equilibrium	37°C	5 min
	1 Cycle	43°C	15 min
4	Initial equilibrium	37°C	5 min
	3 Cycles	43°C	10 min
		37°C	10 min
5	Initial equilibrium	37°C	5 min
	1 Cycle	43°C	30 min

Table 4.S3. Engineered cells used in Chapter 4. Detailed information on the engineered cells (excluding primary human T cells) used in this work, including the cell type, the transgene delivered and the associated delivery method and efficiency, sorting information and applications.

Cell type	Gene delivery method	Construct	Sorting	Efficiency	Application
HEK 293T	Lentivirus	Hsp-eGFP-PGK-mCherry	Not sorted	>99%	Gene activation in vitro by HS
Jurkat	Lentivirus	Hsp-eGFP-PGK-mCherry	Not sorted	>99%	Gene activation in vitro by HS
Jurkat	Lentivirus	Hsp-Cre-PGK-cMyc-LaG17	Not sorted	91.40%	Cre activation in vitro by HS, CD69 assay
	(co-transduction)	PGK-LoxH-ZsGreen-STOP-LoxP-CD19CAR	Not sorted	>99%	
Nalm-6	Lentivirus	Hsp-Fluc-PGK-Rluc-mCherry	FACS	>99%	Gene activation in vivo by FUS
Nalm-6	Gift from Michel Sadelain Lab	constitutive Fluc+	FACS	>99%	In vitro and in vivo cytotoxicity studies
PC3	Lentivirus	pHIV-EF1a-Fluc-IRES-ZsGreen (Addgene)	FACS	>99%	In vitro and in vivo cytotoxicity studies
	(co-transduction)	PGK-PSMA	FACS	>99%	

4.6. Supplemental video captions

Video 4.S1. The dynamics of HS-activated eGFP expression. Real-time fluorescence imaging of two HEK 293T cells transduced with the dual-promoter eGFP reporter (Hsp-eGFP-PGK-mCherry). A 15-min HS at 43°C was applied from 30 to 45 min after the initiation of imaging using a heating stage integrated with the microscope. Imaging lasted for 12 hours. GFP: GFP channel showing the dynamic activation of eGFP; mCherry: mCherry channel showing the constitutive mCherry expression.

Video 4.S2. MRI-guided FUS stimulation on a targeted region on the hindlimb of an anesthetized mouse. MRI images are superimposed with color-coded temperature map of the region of interest. FUS stimulation was aimed at the hindlimb of an anesthetized mouse. The FUS stimulation is composed of a temperature rising phase (Dyn 1 - 10), a steady-state phase (Dyn 11 - 75), and a cool-down phase (Dyn 76-90). Dyn: dynamic; one dynamic of MRI scanning takes 4.6 sec.

Chapter 4, in full, has been submitted for publication of the material. Wu, Y., Liu, Y., Huang, Z., Wang, X., Jin, Z., Li, J., Limsakul, P., Zhu, L., Allen, M., Pan, Y., Bussell, R., Jacobson, A., Liu, T., Chien, S., Wang, Y. Acoustogenetic control of CAR T cells via focused ultrasound. *Submitted.* The dissertation author was the primary investigator and author of this paper.

4.7. References

1. Davila, M. L., Riviere, I., Wang, X., Bartido, S., Park, J., Curran, K., . . . Brentjens, R. (2014). Efficacy and toxicity management of 19-28z CAR T cell therapy in B cell acute lymphoblastic leukemia. *Sci Transl Med, 6*(224), 224ra225. doi:10.1126/scitranslmed.3008226

2. Chakravarti, D., & Wong, W. W. (2015). Synthetic biology in cell-based cancer immunotherapy. *Trends Biotechnol, 33*(8), 449-461. doi:10.1016/j.tibtech.2015.05.001

3. Maus, M. V., Grupp, S. A., Porter, D. L., & June, C. H. (2014). Antibody-modified T cells: CARs take the front seat for hematologic malignancies. *Blood, 123*(17), 2625-2635. doi:10.1182/blood-2013-11-492231

4. Morgan, R. A., Yang, J. C., Kitano, M., Dudley, M. E., Laurencot, C. M., & Rosenberg, S. A. (2010). Case report of a serious adverse event following the administration of T cells transduced with a chimeric antigen receptor recognizing ERBB2. *Mol Ther, 18*(4), 843-851. doi:10.1038/mt.2010.24

5. Akpek, G., Lee, S. M., Anders, V., & Vogelsang, G. B. (2001). A high-dose pulse steroid regimen for controlling active chronic graft-versus-host disease. *Biol Blood Marrow Transplant, 7*(9), 495-502. doi:10.1053/bbmt.2001.v7.pm11669216

6. Di Stasi, A., Tey, S. K., Dotti, G., Fujita, Y., Kennedy-Nasser, A., Martinez, C., . . . Brenner, M. K. (2011). Inducible apoptosis as a safety switch for adoptive cell therapy. *N Engl J Med, 365*(18), 1673-1683. doi:10.1056/NEJMoa1106152

7. Themeli, M., & Sadelain, M. (2016). Combinatorial Antigen Targeting: Ideal T-Cell Sensing and Anti-Tumor Response. *Trends Mol Med, 22*(4), 271-273. doi:10.1016/j.molmed.2016.02.009

8. Cho, J. H., Collins, J. J., & Wong, W. W. (2018). Universal Chimeric Antigen Receptors for Multiplexed and Logical Control of T Cell Responses. *Cell, 173*(6), 1426-1438 e1411. doi:10.1016/j.cell.2018.03.038

9. Fedorov, V. D., Themeli, M., & Sadelain, M. (2013). PD-1- and CTLA-4-based inhibitory chimeric antigen receptors (iCARs) divert off-target immunotherapy responses. *Sci Transl Med, 5*(215), 215ra172. doi:10.1126/scitranslmed.3006597

10. Roybal, K. T., Rupp, L. J., Morsut, L., Walker, W. J., McNally, K. A., Park, J. S., & Lim, W. A. (2016). Precision Tumor Recognition by T Cells With Combinatorial Antigen-Sensing Circuits. *Cell, 164*(4), 770-779. doi:10.1016/j.cell.2016.01.011

11. Wu, C. Y., Roybal, K. T., Puchner, E. M., Onuffer, J., & Lim, W. A. (2015). Remote control of therapeutic T cells through a small molecule-gated chimeric receptor. *Science, 350*(6258), aab4077. doi:10.1126/science.aab4077

12. D'Aloia, M. M., Zizzari, I. G., Sacchetti, B., Pierelli, L., & Alimandi, M. (2018). CAR-T cells: the long and winding road to solid tumors. *Cell Death Dis, 9*(3), 282. doi:10.1038/s41419-018-0278-6

13. Ilyas, S., & Yang, J. C. (2015). Landscape of Tumor Antigens in T Cell Immunotherapy. *J Immunol, 195*(11), 5117-5122. doi:10.4049/jimmunol.1501657

14. Tsien, R. Y. (2003). Imagining imaging's future. *Nat Rev Mol Cell Biol, Suppl*, SS16-21.

15. Thanou, M., & Gedroyc, W. (2013). MRI-Guided Focused Ultrasound as a New Method of Drug Delivery. *J Drug Deliv, 2013*, 616197. doi:10.1155/2013/616197

16. Deckers, R., Quesson, B., Arsaut, J., Eimer, S., Couillaud, F., & Moonen, C. T. (2009). Image-guided, noninvasive, spatiotemporal control of gene expression. *Proc Natl Acad Sci U S A, 106*(4), 1175-1180. doi:10.1073/pnas.0806936106

17. Guilhon, E., Quesson, B., Moraud-Gaudry, F., de Verneuil, H., Canioni, P., Salomir, R., . . . Moonen, C. T. (2003). Image-guided control of transgene expression based on local hyperthermia. *Mol Imaging, 2*(1), 11-17.

18. Wang, S., Zderic, V., & Frenkel, V. (2010). Extracorporeal, low-energy focused ultrasound for noninvasive and nondestructive targeted hyperthermia. *Future Oncol, 6*(9), 1497-1511. doi:10.2217/fon.10.101

19. Piraner, D. I., Abedi, M. H., Moser, B. A., Lee-Gosselin, A., & Shapiro, M. G. (2017). Tunable thermal bioswitches for in vivo control of microbial therapeutics. *Nat Chem Biol, 13*(1), 75-80. doi:10.1038/nchembio.2233

20. Pan, Y., Yoon, S., Sun, J., Huang, Z., Lee, C., Allen, M., . . . Wang, Y. (2018). Mechanogenetics for the remote and noninvasive control of cancer immunotherapy. *Proc Natl Acad Sci U S A, 115*(5), 992-997. doi:10.1073/pnas.1714900115

21. Miller, I. C., Gamboa Castro, M., Maenza, J., Weis, J. P., & Kwong, G. A. (2018). Remote Control of Mammalian Cells with Heat-Triggered Gene Switches and Photothermal Pulse Trains. *ACS Synth Biol, 7*(4), 1167-1173. doi:10.1021/acssynbio.7b00455

22. Raimondi, M. V., Randazzo, O., La Franca, M., Barone, G., Vignoni, E., Rossi, D., & Collina, S. (2019). DHFR Inhibitors: Reading the Past for Discovering Novel Anticancer Agents. *Molecules, 24*(6). doi:10.3390/molecules24061140

23. Abravaya, K., Phillips, B., & Morimoto, R. I. (1991). Attenuation of the heat shock response in HeLa cells is mediated by the release of bound heat shock transcription factor and is modulated by changes in growth and in heat shock temperatures. *Genes Dev, 5*(11), 2117-2127. doi:10.1101/gad.5.11.2117

24. Ghosh, S. K., Missra, A., & Gilmour, D. S. (2011). Negative elongation factor accelerates the rate at which heat shock genes are shut off by facilitating dissociation of heat shock factor. *Mol Cell Biol, 31*(20), 4232-4243. doi:10.1128/MCB.05930-11

25. Martinez, M., & Moon, E. K. (2019). CAR T Cells for Solid Tumors: New Strategies for Finding, Infiltrating, and Surviving in the Tumor Microenvironment. *Front Immunol, 10*, 128. doi:10.3389/fimmu.2019.00128

26. Sridhar, P., & Petrocca, F. (2017). Regional Delivery of Chimeric Antigen Receptor (CAR) T-Cells for Cancer Therapy. *Cancers (Basel), 9*(7). doi:10.3390/cancers9070092

27. Mahmood, U., Levy, L. B., Nguyen, P. L., Lee, A. K., Kuban, D. A., & Hoffman, K. E. (2014). Current clinical presentation and treatment of localized prostate cancer in the United States. *J Urol, 192*(6), 1650-1656. doi:10.1016/j.juro.2014.06.017

28. Musunuru, H. B., Yamamoto, T., Klotz, L., Ghanem, G., Mamedov, A., Sethukavalan, P., . . . Loblaw, A. (2016). Active Surveillance for Intermediate Risk Prostate Cancer: Survival Outcomes in the Sunnybrook Experience. *J Urol, 196*(6), 1651-1658. doi:10.1016/j.juro.2016.06.102

29. Rastinehad, A. R., Anastos, H., Wajswol, E., Winoker, J. S., Sfakianos, J. P., Doppalapudi, S. K., . . . Halas, N. J. (2019). Gold nanoshell-localized photothermal ablation of prostate tumors in a clinical pilot device study. *Proc Natl Acad Sci U S A, 116*(37), 18590-18596. doi:10.1073/pnas.1906929116

30. Boice, M., Salloum, D., Mourcin, F., Sanghvi, V., Amin, R., Oricchio, E., . . . Wendel, H. G. (2016). Loss of the HVEM Tumor Suppressor in Lymphoma and Restoration by Modified CAR-T Cells. *Cell, 167*(2), 405-418 e413. doi:10.1016/j.cell.2016.08.032

31. Roybal, K. T., Williams, J. Z., Morsut, L., Rupp, L. J., Kolinko, I., Choe, J. H., . . . Lim, W. A. (2016). Engineering T Cells with Customized Therapeutic Response Programs Using Synthetic Notch Receptors. *Cell, 167*(2), 419-432 e416. doi:10.1016/j.cell.2016.09.011

32. Wang, C., Li, X., Hu, H., Zhang, L., Huang, Z., Lin, M., . . . Xu, S. (2018). Monitoring of the central blood pressure waveform via a conformal ultrasonic device. *Nature Biomedical Engineering, 2*(9), 687-695. doi:10.1038/s41551-018-0287-x

33. Boyden, E. S., Zhang, F., Bamberg, E., Nagel, G., & Deisseroth, K. (2005). Millisecond-timescale, genetically targeted optical control of neural activity. *Nat Neurosci, 8*(9), 1263-1268. doi:10.1038/nn1525

34. Fite, B. Z., Liu, Y., Kruse, D. E., Caskey, C. F., Walton, J. H., Lai, C. Y., . . . Ferrara, K. W. (2012). Magnetic resonance thermometry at 7T for real-time monitoring and correction of ultrasound induced mild hyperthermia. *PLoS ONE, 7*(4), e35509. doi:10.1371/journal.pone.0035509

35. McBurney, M. W., Sutherland, L. C., Adra, C. N., Leclair, B., Rudnicki, M. A., & Jardine, K. (1991). The mouse Pgk-1 gene promoter contains an upstream activator sequence. *Nucleic Acids Res, 19*(20), 5755-5761. doi:10.1093/nar/19.20.5755

CHAPTER 5. CONCLUSION

5.1. Research summary

My doctoral research is mainly composed of two parts: the visualization and understanding of molecular events in tumor cells via FRET biosensors and computational analysis, and the remote control of T cell functions using FUS-based acoustogenetics for therapeutic purposes, with more focus on the latter as we continue exploring the potential of this technology for other applications.

Chapter 1 provides a general introduction on the background of my research projects. The discovery of FRET and FPs and the development of FRET biosensors enabled the visualization of molecular events in live cells at unprecedented resolutions. Meanwhile, genetic engineering has empowered us to reprogram cells for desired therapeutic purposes, with CAR T therapy being one of the most recent and revolutionary examples. Despite the huge success of CAR T therapy in treating blood cancers, certain side effects and limitations need to be overcome before it can be used to treat solid tumors.

Chapter 2 summaries my research on deciphering the temporal coordination between FA assembly/disassembly and kinase (FAK and Src) activities. The targeting of FRET biosensors to FA sites, the FA tracking algorithm, and the computational cross-correlation analysis employed in this study enabled the quantification of the temporal coupling at the single FA level, as opposed to previous studies collecting averaged information from traditional biochemical assays. The study thus provided new insights into this field.

Chapters 3 and 4 focus on my second project on remote controllable CAR T therapy via MRI-guided FUS. At the beginning of my doctoral research, I witnessed the explosion of interests in CAR T therapy in immunology and biomedical engineering fields. Meanwhile, the

fields were also aware of the side effects of this treatment, especially its on-target off-tumor toxicity, and several approaches were developed to tackle this problem, such as the synNotch CAR and small molecule inducible CAR. We, as bioengineers, sought to approach this problem from a different angle. Our lab utilized different engineering tools (e.g., light, focused and unfocused ultrasound) in combination with synthetic biology to remotely control the activation of inducible CAR T cells, opening a new era of remote and noninvasive controllable immunotherapy.

Among these, I engineered heat-sensitive CAR T cells and used the MRI-guided FUS to generate heat in local tissues *in vivo* for the activation of infused T cells. I demonstrated that the heat-sensitive CAR T cells were function after heat induction *in vitro*. I also calibrated and characterized an MRI-guided FUS system and used it to induce local temperature increase deep in phantom and *in vivo* that led to heat-sensitive transgene activation in engineered cells. Lastly, using tumor-bearing mouse models, I showed that the heat-sensitive CAR T cells could inhibit tumor growth after MRI-guided FUS stimulation. With the widely available FUS systems in clinics, we envision that this technology has great translational potential and may benefit patients in the near future.

5.2. Future work

While working on the remote control of CAR T cells using MRI-guided FUS, we realized the power of this acoustogenetics technology and envision that it can be generalized as a platform for the remote regulation of genetic/epigenetic activities and the corresponding cellular functions *in vivo*.

5.2.1. Remote regulation of endogenous genes

One example is to integrate FUS-based acoustogenetics with CRISPR technology to remotely regulate endogenous genes. We place the Hsp upstream of a guide RNA (gRNA) flanked by two ribozymes that enables the expression of gRNA under an RNA polymerase II promoter (*1*). The endonuclease dead Cas9 (dCas9) fused with transcriptional activators/repressors is also introduced into the cells. Upon FUS stimulation, the induced gRNA binds to dCas9 and targets the transcriptional activators/repressors to the desired locus on the genome, causing corresponding charges in the expression of the targeted endogenous gene.

As proof-of-concept, we cloned a Hsp-driven gRNA 1 targeting a synthetic promoter P1 (Hsp-dsRed2-triplex-HHRibozyme-gRNA1-HDVRibozyme-pA, abbreviated as Hsp-gRNA1). We co-transfected HEK 293T cells with Hsp-gRNA1, constitutive dCas9 fused with transcriptional activator VP64 (CMVp-dCas9-3xNLS-VP64, abbreviated as dCas9-VP64), and the synthetic P1 promoter-driven EYFP (P1-EYFP). Our results show that a 30min HS at 43°C induced EYFP expression in 10.7% of the cells (non-sorted, including both engineered and non-engineered cells), compared to 0.81% in the cells without HS (Fig. 5.1). We further cloned a plasmid of the Hsp driving both gRNA 1 and gRNA 2, with the latter targeting a synthetic promoter P2 (Hsp-dsRed2-Triplex-HHRibozyme-gRNA1-HDVRibozyme-HHRibozyme-gRNA2-HDVRibozyme, abbreviated as Hsp-gRNA1-gRNA2). We co-transfected HEK 293T cells with Hsp-gRNA1-gRNA2, dCas9-VP64, P1-EYFP and P2-driven ECFP (P2-ECFP), and observed that both EYFP and ECFP expressions were induced after HS (Fig. 5.2). These results show that heat can activate Hsp-driven gRNAs to regulate target gene expressions using CRISPR/Cas tools.

The next step is to design Hsp-driven gRNAs targeting endogenous genes. We will perform *in vitro* HS on the engineered cells to characterize and validate the genetic circuits. The engineered cells will then be injected into mice followed by FUS stimulation *in vivo*. The corresponding gene expressions and functional outcomes will be analysed to determine the efficiency of FUS- and CRISPR-based endogenous gene regulation.

5.2.2. Remote control of epigenetics

Epigenetics describes heritable changes such as DNA methylation and histone modifications that affect the function of the genome without altering its DNA sequence (*2-4*). We propose that MRI-guided FUS can be used to remotely reprogram the epigenetics of cells *in vivo* using heat-inducible epigenetic regulators. Recently, a "hit-and-run" system was shown to achieve inheritable long-term gene silencing with transient transfection of a combination of the transcriptional repressor KRAB and the catalytic domains of DNA methyltransferases (DNMTs) 3A and 3L (*4*). By constructing a Hsp-driven hit-and-run system, we can use FUS to selectively silence genes such as methylcytosine dioxygenase TET2, the disruption of which has been shown to promote CAR T cell efficacy (*5*).

In summary, we envision that when combined with genome-editing technologies, FUS-based acoustogenetics will allow the dynamic modulation of endogenous epigenome/genome in cells at a location deep in living organisms.
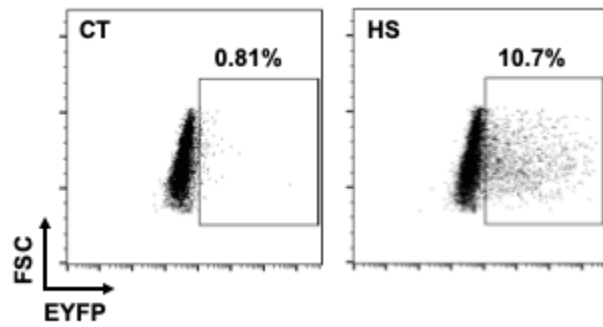
Figure. 5.1. Reporter gene expression in HEK 293T cells engineered with the heat-inducible CRISPR system with or without heat stimulation. Cells were transfected with Hsp-driven gRNA1 targeting a synthetic P1 promoter, constitutive dCas9 fused with transcriptional activator VP64, and the synthetic P1 promoter-driven EYFP. The reporter EYFP expression was quantified using flow cytometry 24 hr after HS. CT: without HS; HS: with 30min HS at 43°C.

Hsp-dsRed2-gRNA1-gRNA2	CMV-dCas-VP64	P1-EYFP	P2-ECFP	ECFP	EYFP	dsRed2
+	+	+	+			
+	+	+	-			
+	+	-	+			
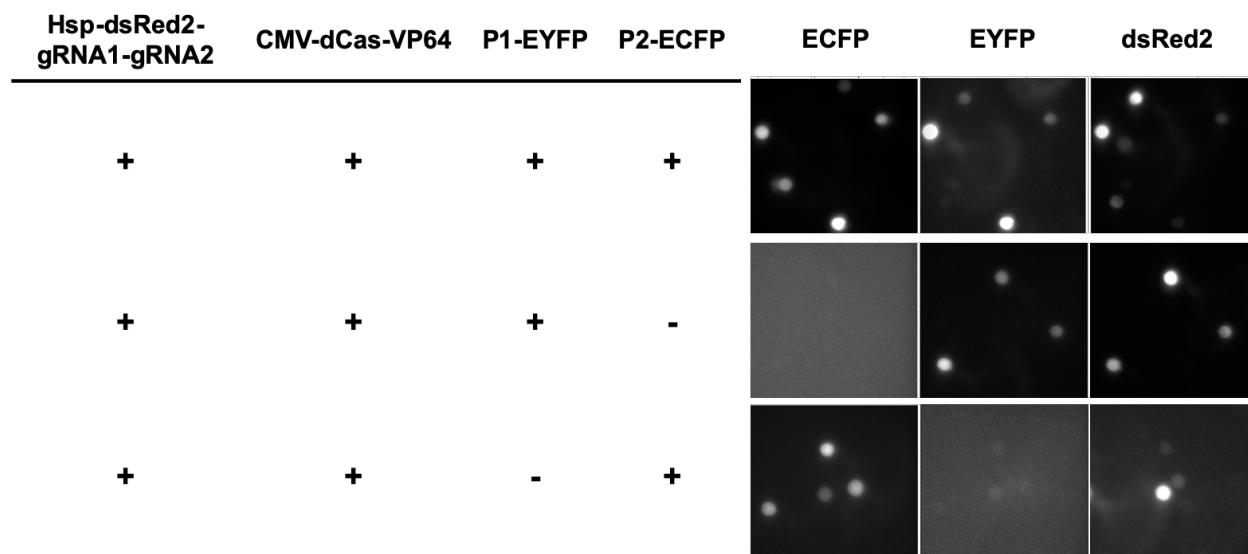
Figure 5.2. Representative images of the expression of reporter genes in HEK 293T cells transfected with different components of the heat-inducible CRISPR system. All three groups received 30min HS at 43°C. Expression of the reporter genes EYFP and ECFP were visualized with fluorescent microscopy 24 hr after HS. +: construct transfected; -: construct not transfected.

5.3. References

1. Nissim, L., Perli, S. D., Fridkin, A., Perez-Pinera, P., & Lu, T. K. (2014). Multiplexed and Programmable Regulation of Gene Networks with an Integrated RNA and CRISPR/Cas Toolkit in Human Cells. *Mol Cell, 54*(4), 698-710. doi:10.1016/j.molcel.2014.04.022

2. Dupont, C., Armant, D. R., & Brenner, C. A. (2009). Epigenetics: Definition, Mechanisms and Clinical Perspective. *Seminars in Reproductive Medicine, 27*(5), 351-357. doi:10.1055/s-0029-1237423

3. Jaenisch, R., & Bird, A. (2003). Epigenetic regulation of gene expression: how the genome integrates intrinsic and environmental signals. *Nature Genetics, 33*, 245-254. doi:10.1038/ng1089

4. Amabile, A., Migliara, A., Capasso, P., Biffi, M., Cittaro, D., Naldini, L., & Lombardo, A. (2016). Inheritable Silencing of Endogenous Genes by Hit-and-Run Targeted Epigenetic Editing. *Cell, 167*(1), 219-+. doi:10.1016/j.cell.2016.09.006

5. Fraietta, J. A., Nobles, C. L., Sammons, M. A., Lundh, S., Carty, S. A., Reich, T. J., . . . Melenhorst, J. J. (2018). Disruption of TET2 promotes the therapeutic efficacy of CD19-targeted T cells. *Nature, 558*(7709), 307-+. doi:10.1038/s41586-018-0178-z